TOPOCHEMICAL SYNTHESIS AND ELUCIDATION OF STRUCTURE-PROPERTY RELATIONSHIPS IN MAGNETIC KAGOMÉ MATERIALS AND OTHER GEOMETRICALLY FRUSTRATED LATTICES

by
ZACHARY ANDREW KELLY

A dissertation submitted to Johns Hopkins University in conformity with the requirements for the degree of Doctor of Philosophy

Baltimore, Maryland
February, 2018

© 2018 Zachary Andrew Kelly
All Rights Reserved

Abstract

Solid state chemistry is the study of extended crystalline solids containing $\sim 10^{23}$ atoms. The overarching goal of solid state chemistry is to design new materials with specifically targeted properties. This is often accomplished by leveraging structure-property relationships. The focus of chapters 1 and 2 are to introduce key concepts for understanding structure-property relationships in solid state materials: electronic band theory, the concept of symmetry, the origins of magnetism, the phase transition theory, and methods. Refinement of these highly predictive and informative theoretical frameworks continues to push our understanding of materials and provides a pathway to discover novel emergent phenomena.

Chapter 3 discusses the synthesis and properties of electron-doped synthetic Herbertsmithite, the first example of a doped canonical kagomé spin liquid. Previous pressure and doping studies have demonstrated that certain frustrated geometries display metallicity, but it has proven difficult to successfully introduce charges into definitively two dimensional spin liquids built on the kagomé or honeycomb lattice. By applying topochemical techniques, we were able to achieve it experimentally. We find that electron doping continuously suppresses the magnetism in the material without the appearance of superconductivity or related metallic phases. This is significantly different than the predictions of theory, which must be refined in light of our results.

Chapter 4 reports the realization of an ideal $S = 1$ kagomé in $Na_2Ti_3Cl_8$. This quantum magnet undergoes a discrete two-step trimerization on cooling, transforming from a cen-

trosymmetric high temperature phase to non-centrosymmetric, ferroelectric intermediate and low temperature phases via successive first order phase transitions and the formation of metal-metal bonds. We believe this is a novel mechanism to induce a proper ferroelectric phase transition at achievable temperatures driven through frustrated magnetism and metal-metal bonding. Development of new mechanisms to induce ferroelectricity remains rare. The unique kagomé to trimer ferroelectric transition with two discrete ferroelectric phases positions compounds that exhibit the same metal-metal bonding mechanism as $Na_2Ti_3Cl_8$ to be highly viable for incorporation into the next generation of multifunction devices.

Chapter 5 highlights the result of a collaboration with Prof. Kageyama at Kyoto University, Japan, supported by the NSF EAPSI fellowship. In Japan, I explored both low temperature techniques and high pressure syntheses to target new irridate compounds with a distorted honeycomb lattice. The compound $Sr_3CaIr_2O_9$ has a unique corner-sharing connectivity of the iridium sub-lattice which forms a honeycomb structure. This corner-sharing allows for a specific type of magnetic exchange which could lead to the realization a magnetically frustrated system predicted to host the Kitaev spin liquid state. The issue is $Sr_3CaIr_2O_9$ is non-magnetic since Ir is in the $5d^4$ electronic state. This collaboration reviews the progress of reducing $Sr_3CaIr_2O_9$ from the $5d^4$ to $5d^5$ in an attempt to realize the Kitaev spin liquid model.

Dissertation Committee

Tyrel M. McQueen (Primary Advisor)
Professor
Department of Chemistry
The Johns Hopkins Krieger School of Arts and Sciences

John D. Tovar
Professor
Department of Chemistry
The Johns Hopkins Krieger School of Arts and Sciences

Howard D. Fairbrother
Professor
Department of Chemistry
The Johns Hopkins Krieger School of Arts and Sciences

To my Mother and Father

who instilled in me a passion for science

and to Danielle
for being my guiding light

Acknowledgments

It is difficult to put into words how incredibly grateful I am for those whom I have formed relationships throughout this endeavor. It has been an absolute pleasure and an honor to work under the guidance of Professor Tyrel M. McQueen. He is truly one of the most intelligent, innovative, and (most importantly) genuinely kind and generous people I have ever had as a colleague. I thank you for all that you have taught me and for allowing me to pursue whatever interested me.

I would also like to thank my committee, Professor Tovar and Professor Fairbrother, for their guidance and advice.

Graduate school would be a death sentence if it wasn't for my fellow graduate students and postdocs. A special thanks to John Sheckelton, Patrick Cottingham, W. Adam Phelan, Allyson Fry-Petit, Benjamin Trump, Kate Arpino and David Wallace for taking me under your wings during the start of my graduate career. I would also like to thank Jessica Panella, Juan Chamorro, Mike Quintero, Jennifer Morey, Jake Tutmaher, Mike Winiarski, Cheng Wan, Thao Tranh, Hongcheng Lu, Veronica Stewart, Mekhola Sinha, Hector Vivanco, and Tanya Berry for all of the support, friendships, and laughs.

This department would be in shambles if it wasn't for our chemistry office, Jean Goodwin, Rosalie Elder, John Kidwell, Lauren McGhee, Meghan Carter, Joe Russell, and our two incredible building managers Boris Steinburg and Brian Schriver who are always willing to lend a hand.

I would like to especially acknowledge the Physics department community which I

worked in. Professors Collin Broholm, N. Peter Armitage, and Oleg Tchernyshyov have been accessible resources to me, and have each enriched the department and IQM with their distinctive personalities. My neighboring physics students and post-docs have made me feel welcome, taught me, and have helped me grow as a scientist. Among those, I would like to specifically acknowledge Wes Fuhrmann, Thomas O'Connor, Guy Marcus, Shan Wu, Allen Scheie, and Joel Clemmer.

I am deepy thankful for the guidance of my Japanese EAPSI Advisor, Professor Kageyama. He is an incredible scientist and a blast to talk with over beer and ramen.

I'd also like to recognize the close friendships I made during my time here. Reid, Julie, Ken, Justin, Ron, Kristen, Digs, Snooze, and the entire softball team. May house Dellwood live forever in our hearts.

Finally, I would like to thank my childhood friends and my family. Their love and support has been unwavering, and I couldn't have done it without them. My friends Anthony, Andrew, Arthur, Brendan, Matt, and Phong have been like brothers to me. I am especially thankful to my parents who have instilled in me a love for science and a passion for life. I'd also like to thank them for all the time they spent and sacrifices they made that allowed me to pursue chemistry. My sister, Amy, and brother, Matt, are an inspiration to me. They posses incredible capacities for strength, love, and kindness, and they taught me what it means to lead a good life. The newest additions to our family, my brother-in-law, John and my nephew, Thomas, have been amazing, and I am so happy I can call them family. Lastly, I'd like to thank my partner in life, Danielle. She makes my life more fulfilling than I ever thought possible, and I am so excited for our next chapter together.

Table of Contents

List of Figures

List of Tables

List of Tables

1 Introduction

The primary focus of this dissertation is geometrically frustrated magnetic systems, namely crystalline materials with magnetic kagomé and honeycomb lattices. This chapter introduces key concepts and principles that lay the ground work to understand the behavior of these materials and motivation of the research performed.

One of the most rewarding aspects of my thesis research was the ability to engage with all phases of the material discovery throughout the material life cycle. The process begins by examining the current theories and predicting a model material that may host the desired property. Once identified, a variety of synthetic methods are used to try to synthesize the target material and characterize its properties (Figure 1.0.1). Frequently it takes multiple rounds of synthesis and characterization to reach the target compound using the off target synthesis attempts as a guide to determine the tolerances of the system. There are times where the perfect target material cannot be made with current techniques, however the information is utilized to expand the theory and methods of material synthesis and to push our current understand of concepts in the field. Serendipity has led to the most important discoveries in history from fire, superconductors, and more recently CRISPR/Cas9.[4**?**] As the scientific fields of chemistry become more specialized, it is important to remember to always keep an open mind and think of the potential impact of our discoveries across multiple scientific disciplines. This philosophy embodies the mindset of the McQueen group, where we explore materials with heavily competing internal interactions in the hopes of discovering new emergent phenomena.

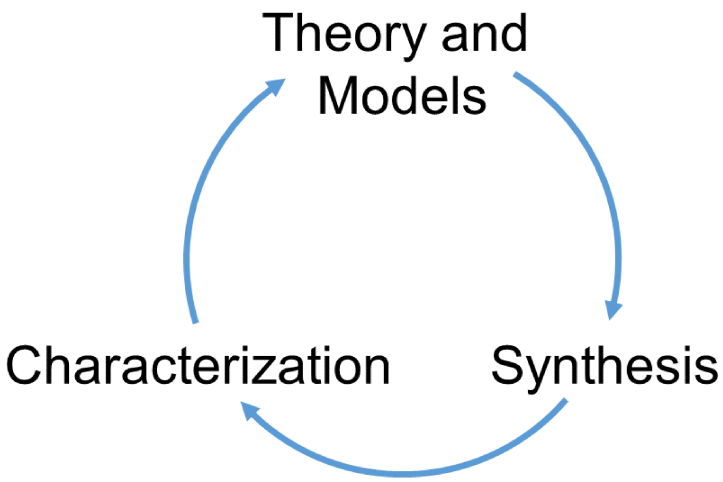

Figure 1.0.1: The material life cycle which has three main phases: theory and model development, synthesis of target compounds, characterization of the structural and physical properties which leads to the updating of the theory and model repeating the cycle.

1.1 Emergence

Emergent properties are a puzzling and fascinating phenomena ubiquitous in the chemistry of solids. In the physical sciences, there has always been a drive to understand nature at its most fundamental level. In the constructionist view point, only the most fundamental laws of the universe are needed to predict the behavior of all things: from atoms, molecules, and proteins to the occurrence of life, galaxies, and the entire universe. However, it is abundantly obvious to researchers in higher level many-body fields that behavior of all systems can not be described by a simple extrapolation of the properties of a few elementary particles. As a system grows in complexity and scale, new emergent behavior appears. Theses emergent properties appear to be themselves as fundamental as the particles that compose them.[5] While the epistemological question of whether emergent properties are *truly* fundamental remains unclear (and is a debate which will be left to philosophers),

scientifically approaching them as such has been highly fruitful for gaining understanding of many emergent properties.

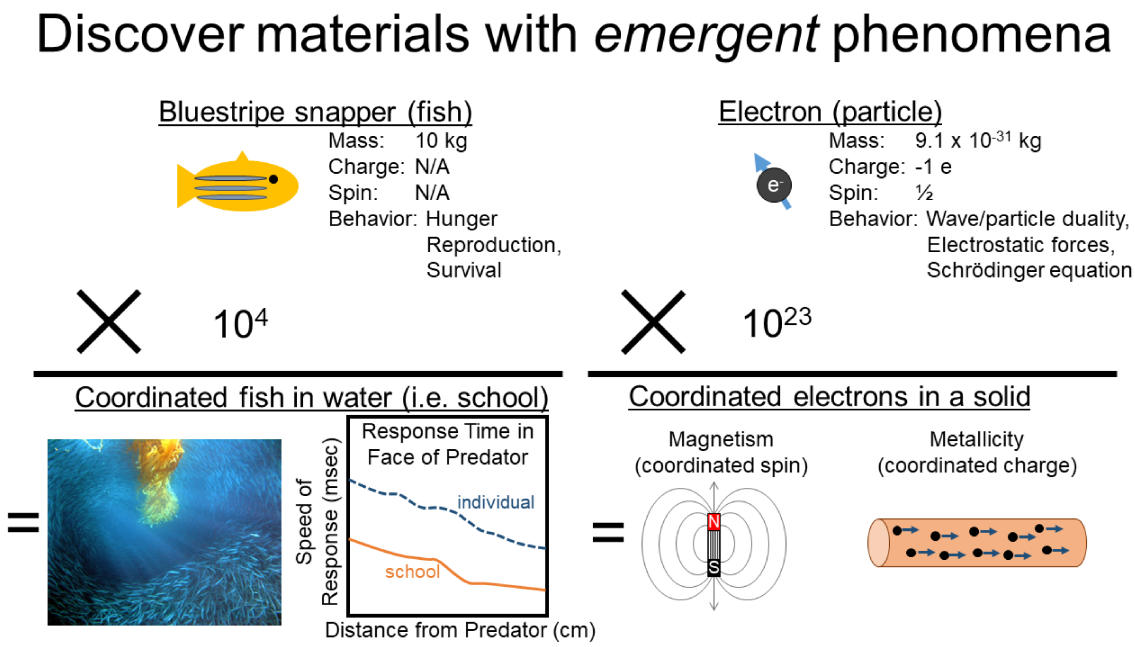

Figure 1.1.1: Illustrations of two emergent phenomena in the real world: Schooling of fish and magnetic and metallic behavior of solids.

1.2 From Electrons to Extended Solids

1.2.1 Electrons

Quantum mechanics lays the ground work for our understanding of atoms and subatomic particles, in particular the electron. An electron has a charge of negative one and a spin, intrinsic angular momentum, of $\frac{1}{2}$. When an electron is in a state (i.e. confined to specific set of conditions), it can be described in terms of a wave function. The electron wave function, Ψ, describes state of the system where $|\Psi|^2$ is the electron probability-density. The energy of the system, E, can be solved using the Schrödinger equation where $H\Psi = E\Psi$.[6, 7] In the single electron case of the hydrogen atom, Schrödinger equation can be solved exactly. Once systems get any more complex, the Hamiltonian is constructed by accounting for

all of the nuclear and electron interactions (e^- kinetic energy, $e^- - e^-$ repulsion, nucleus kinetic energy, nucleus-nucleus repulsion, and coulombic attraction), resulting in:[8]

$$H = -\sum_i \frac{p_i^2}{2m_e} + \sum_{i,j} \frac{e^2}{|r_i - r_j|} - \sum_n \frac{p_n^2}{2m_n} + \sum_{m,n} \frac{z_m z_n e^2}{|R_m - R_n|} - \sum_{m,i} \frac{z_m e^2}{|R_m - r_i|} \tag{1.1}$$

where p is momentum, m_e and m_n are the mass of an electron and nucleus respectively, R and r are radial distances, an Z is the atomic number. Although an equation can be written explicitly to describe all of the possible contributions, the complex interactions of many body effects make exact solutions practically unattainable and therefore must be approximated numerically. There are a number of different models and techniques to calculate the electronic wavefunctions of real materials with density functional (DFT) theory being by far the most common. A chemically intuitive version of DFT uses local orbitals (which can be estimated by atomic orbitals) in what is referred to as the tight binding model.[9]

1.2.2 Band Structures- Tight Binding Model

In small molecules, one method to construct molecular orbitals is through the linear combining of valence atomic orbitals (LCAO) also known as the tight binding model. Figure 1.2.1 shows the construction molecular orbits of increasing ring sizes using *s* orbital. On the far left, where N = 2, the atomic orbitals mix to form two molecular orbitals below and above their original individual atomic orbital energies. As the chain length increases, more discrete molecular orbitals are created, splitting in energy ranging from the lowest energy bonding orbital to the highest energy antibonding orbital.[10, 11] As the length approaches infinity, the energy gap between neighboring orbitals becomes so small that the discrete molecular orbitals can be approximated as a continuous band. By integrating the number of states across the band, the density of states (DOS) shows the relative concentration of states at different energies. The Fermi level (E_f) is the chemical potential separating the highest occupied molecular orbital (HOMO) and lowest unoccupied molecular orbital

(LUMO) at absolute zero.

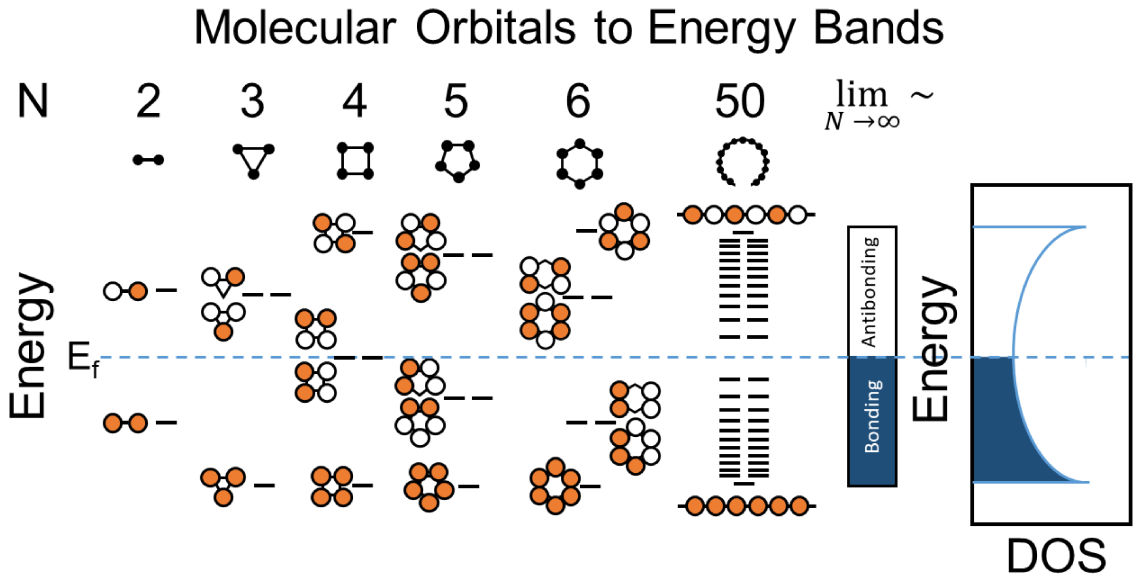

Figure 1.2.1: An illustration of the construction of molecular orbitals approximated from the linear combination of *s* atomic orbitals on rings of atoms. The simple case of a dimer is shown on the far left, where two molecular orbitals, bonding and antibonding, are formed. As the ring size (N) increases, more molecular orbitals are formed spanning different energies depending on their degree of bonding. As N becomes large, the quantized energy differences between neighboring energy levels becomes small and the energy levels can be approximated as continuous band of energies. Integrating over this band gives the density of states (DOS) at a given energy.

The periodicity of a crystalline structure impacts the overall wave function of the electrons and therefore the properties of the material. This is described by a Bloch function (equation 1.2) which returns the wave function, Ψ, multiplied by a periodic function, e^{ika} as follows:

$$\Psi(x+a) = e^{ika}\Psi(x) \tag{1.2}$$

where k is the crystal wave vector, i is the imaginary number, a is the length of the repeating unit (unit cell). This equation sets boundary conditions. When k =0 the Bloch function returns $\Psi(x+a) = \Psi(x)$ resulting in full bonding while at the other extreme if $k = \frac{\pi}{a}$ the function returns $\Psi(x+a) = -\Psi(x)$ resulting in full antibonding between each repeating

unit. A visualization of the meaning of different k values in shown in Figure 1.2.2.[12]

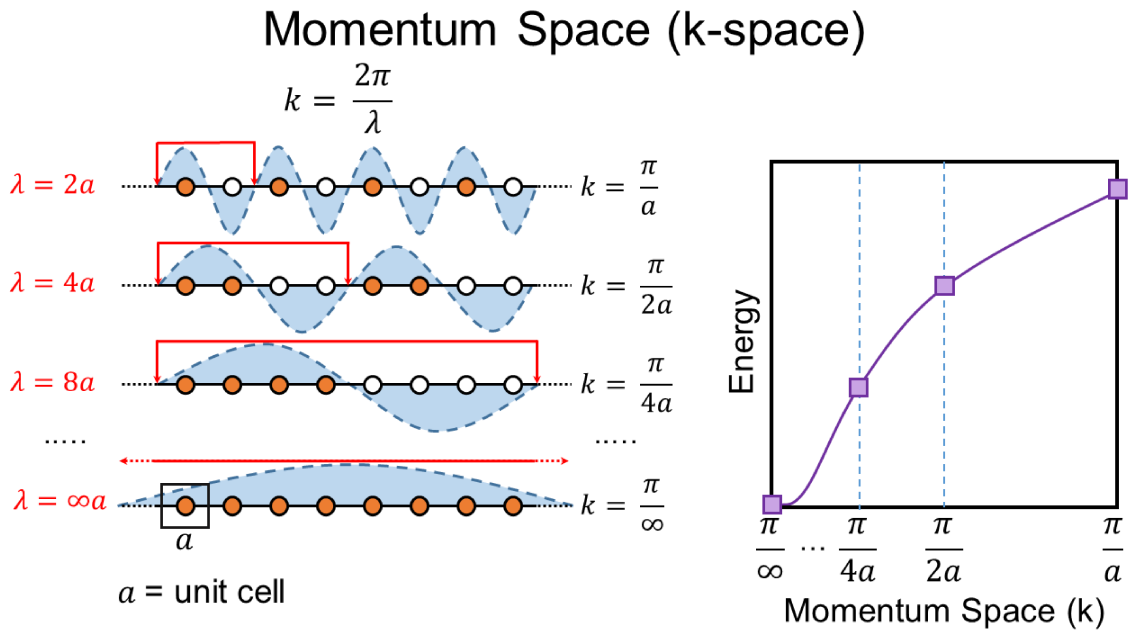

Figure 1.2.2: An illustration of the relationship between the k vector and electronic states in a 1D chain of s orbitals. The parity of a orbital is represented by its color (white and orange) which, in the case of s orbitals, also directly corresponding with the sign of the wave function. The blue wave form is a visualization of λ which is related to the k vector by $k = \frac{2\pi}{\lambda}$. The resulting electronic band structure is plotted as a function of k-space (momentum space).

The energy of a band can be plotted as a function of k vector which is called k-space or momentum space. Bands can either increase or decrease in energy from one point in momentum space to another depending on their orientation and atomic character. This is nicely demonstrated in the case of p orbitals on a 1-D chain as shown in Figure 1.2.3 **a**. The p_z orbital is oriented perpendicular to the 1-D chain. At $k = 0$, all p orbitals have the same sign and parity on every atom, so the upper lobe and lower lobe match in parity and allow for bonding. When $k = \frac{\pi}{a}$, the parity between every atom alternates leading to the full antibonding case, similar to the case seen in s orbitals in a 1-D chain. Aligned with the 1-D chain, the p_x orbital has the opposite k-dependence where $k = 0$ results in full antibonding and $k = \frac{\pi}{a}$ is the lowest energy full bonding state. Therefore their respective bands run in opposite directions in k-space.

Understanding the k dependence of energy bands is critical for explaining behaviors of certain materials such as indirect band gap photovoltaics and semi-metals which can not be understood without mapping the k dependence. Photovoltaics are semiconductors which have a band gap which spans the approximate energy of visible light (1-2 eV). Their band gap can either be direct, where a photon can excite an electron directly into the conduction band, or indirect, where a photon must pair with a lattice vibration to excite the electron and translate the electron's momentum to match the momentum of the conduction band, demonstrated in Figure 1.2.3 **b**. These direct vs. indirect mechanism greatly effect the overall performance of the photovoltic and must be considered in the design of the solar cell to optimize its efficiency. The simple energy only band picture is indistinguishable for both the direct and indirect case as shown. This is also observed in the metal vs. semi-metal case, which have identical energy only band structures but distinct k-dependent band structures which explains the difference in properties.

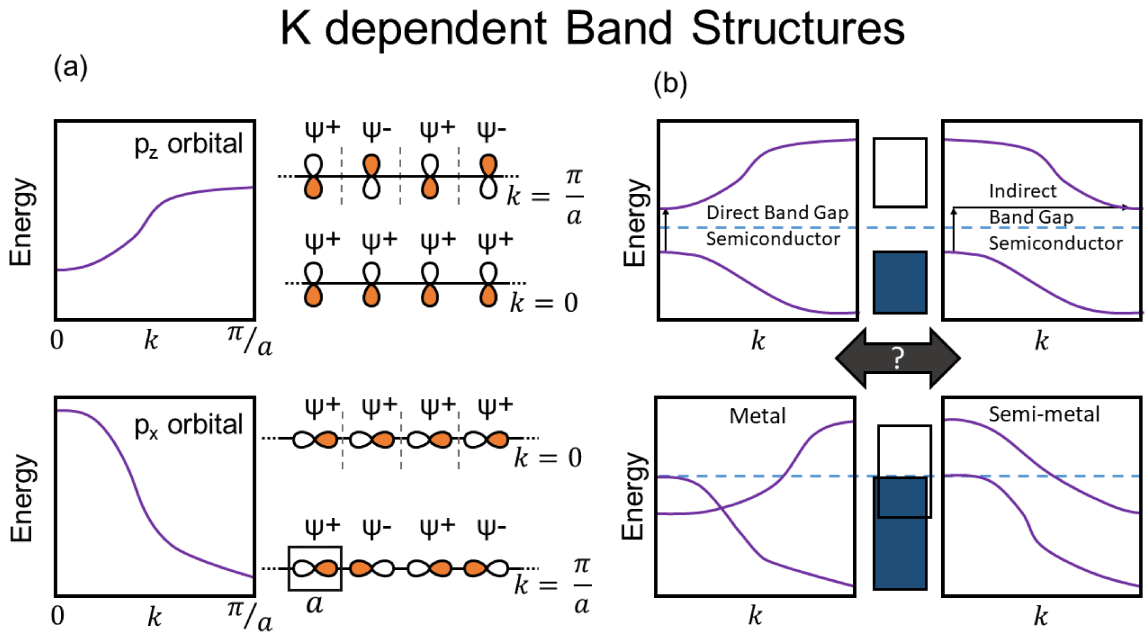

Figure 1.2.3: a) An illustration of the k-dependent band structures for typical p_x and p_z atomic orbitals in a 1D chain. Due to their orientation, the bands have different band widths and opposite energy trends. **b)** Schematics of band diagrams for a direct band gap semiconductors, indirect band gap semiconductors, metal, and semimetal respectively. The energy only band diagram is shown (white and blue blocks) between the schematics to demonstrate the inability of the energy only band diagrams to distinguish between these related materials.

1.2.3 Electron-Electron Interactions in Solids

Although tight bonding model has a lot of explanatory power, it predicts certain materials, such as synthetic Herbertsmithite, to be a metallic. However, Herbertsmithite is an insulator with a band gap of ∼1.7 eV.[65] Why does the tight binding model fail to predict the behavior of this material?

Synthetic Herbersmithite has a the chemical formula of $ZnCu_3(OH)_6Cl_2$ and contains copper with an oxidation state of 2+ (d^9). The copper is in a Jahn-Teller distorted octahedral crystal field which causing the d orbitals to split.[7] The $d_{x^2-y^2}$ orbital becomes the highest occupied molecular orbital (HOMO) with an single unpaired electron (Figure 1.2.4 **a**). Metals are materials with partially filled bands, where electrons require minimal thermal energy to easily move past one another and conduct electricity. Insulators have a fully

occupied band where the electrons must be excited to an unoccupied band in order to be mobile and conduct electricity. The distance between these bands is called a band gap (analogous to a HOMO-LUMO gap). In Herbersmithite, the $d_{x^2-y^2}$ band is exactly half filled so the tight-binding model would predict Herbertsmithite to be a metal. However, the model fails to take into account the energy cost associated with moving an electron into a partially occupied orbital due to electron-electron interactions.[14] An example of this is shown in Figure 1.2.4 **b** where a 1D chain of $d_{x^2-y^2}$ orbitals are each filled with one electron. When an electron hops to a neighboring orbital, the electrons interact giving rise to the Hubbard U.[15, 16] The Hubbard U is defined as:

$$U = I - A \tag{1.3}$$

where U is the Hubbard U, I is the ionization potential, and A is the electron affinity. The Hubbard U effectively splits the $d_{x^2-y^2}$ band into two forming a gap between the occupied and unoccupied states (Figure 1.2.4 **c**). This type of insulator is called a Mott insulator. The strength of U and the band widths of the energy bands determine the size of the band gap.

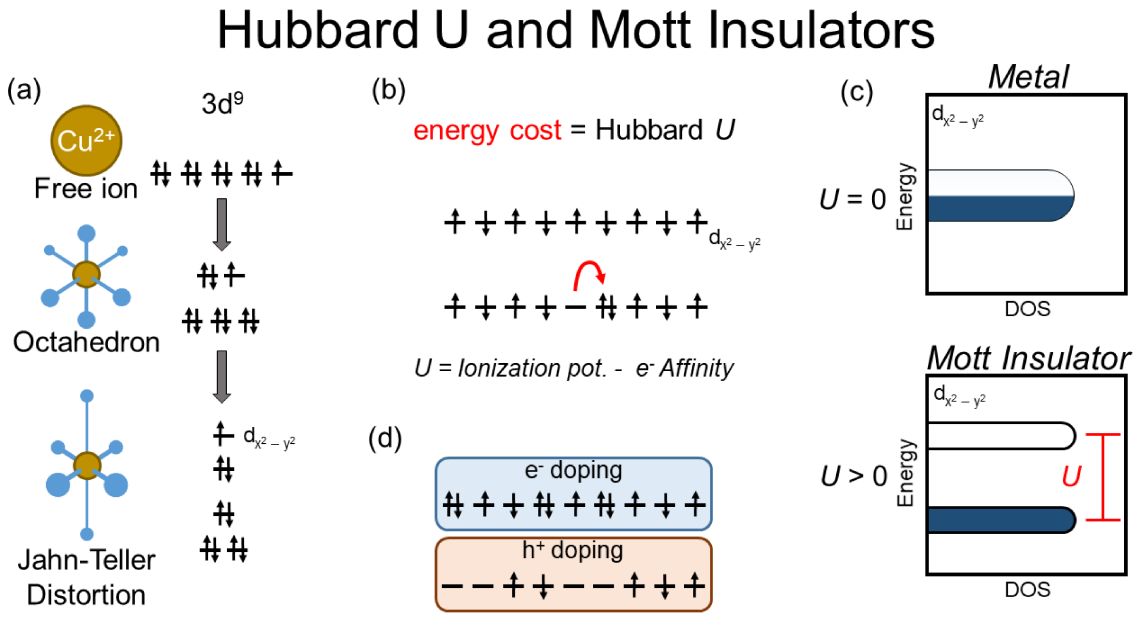

Figure 1.2.4: **a)** A schematic of the octahedra crystal field spliting and Jahn-Teller distortion of a Cu^{2+} ion. **b)** An illustration of the half filled $d_{x^2-y^2}$ in real space in 1D. The movement of one electron to a neighboring orbital that is already half occupied requires energy, the Hubbard U. **c)** A schematic of the predicted density of states of the $d_{x^2-y^2}$ band given a $U = 0$ and $U > 0$. The material is predicted to be a metal if $U = 0$ and an insulator if $U > 0$. **d)** An illustration of electron and hole doped electron states to avoid the half filled state.

Another factor that can influence effective band gap of materials with a Hubbard U is electronic orbital contributions from the neighboring anions present in many solids (e.g. O, S, Se, and Te). The anion p band tends to have a large band width which can overlap with the lower Hubbard band of the transition metal. As the transition metals d band moves down in energy with increasing nuclear charge (left to right on the periodic table), the lower Hubbard band approaches the anion p band in energy until the top of anion p band is above the lower Hubbard band. The p band is now the highest energy occupied band allowing an electron from the p band to be excited to the unoccupied upper Hubbard band with a band gap of Δ (Figure 1.2.5).[1, 6] A material with this p to d band gap is a charge transfer insulator where the charge from the anion is moved to the transition metal.

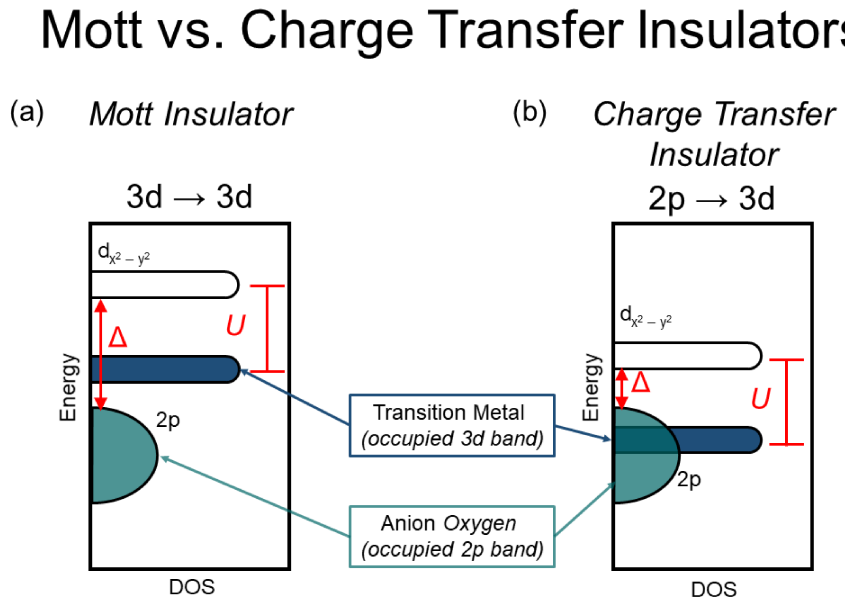

Figure 1.2.5: **a)** A schematic of a density of states of a Mott insulator where the smallest band gap is between the top of the metal's lower Hubbard band and the bottom of the upper Hubbard band. **b)** A schematic of the density of states of a charge transfer insulator, where the smallest band gap is the charge transfer band gap, Δ, between the anion p band and the transition metal d band.[1]

Mott insulators occur when a d band is half full. Removing electrons from a Mott insulator results in vacant orbitals in the material's electronic state. The movement of an electron from its original orbital to a vacant orbit avoids any electron-electron interactions greatly reducing the energy cost and allowing the electron to be more mobile. The same principle applies by adding electrons to the system to form a set of paired electrons which can also move more easily from orbital to orbital.[17] The addition and removal of electrons is referred to as "doping" (Figure 1.2.4 **d**). Doping Mott insulators can induce an insulator to metal transition and is theorized to be an approach to design high temperature superconductors as suggested by the high T_c cuprates. Herbertsmithite is a Mott insulator with strong magnetic interactions and is considered one of the leading candidates to obtain a high temperature superconducting state if the material can be sufficiently doped to obtain a metallic state. This will be discussed in more detail in later chapters.

1.3 Crystal Structures

Crystals consist of long-range ordered periodic units and are classified by their symmetry.[18] Though widely appreciated by the layperson in terms of aesthetic beauty, symmetry is a recurring and highly predictive paradigm throughout the natural sciences. In chemistry, symmetry is used to determine and predict many physical parameters such as the degree of orbital mixing, allowed electronic excitations, and vibrational modes to name a few. Similarly, the symmetry of an extended crystal largely determines the materials properties.

1.3.1 Unit cell and space group symmetries

Point group symmetry is familiar concept in general chemistry, but translational and space symmetries are the purview of solid state chemistry. The unit cell is defined as smallest group of atoms that displays the overall symmetry of the crystal and, when combined with translational symmetry, contains all the information needed to completely reconstruct the entire crystal.[6] The unit cell must tile all 3-D space without gaps, so there is a finite number of possible geometries for a valid unit cell. Unit cells fall into 7 crystal systems which are, from low to high symmetry: triclinic, monoclinic, orthorhombic, tetragonal, trigonal, hexagonal, and cubic. These crystal systems are defined by their lattice parameters: a, b, and c are the lengths of the sides of the cell and α, β, and γ are the corresponding angles between the faces of the cell. When taking into consideration translational symmetry, these seven crystal systems can be categorized by 14 possible Bravais lattices. A lattice is defined as a set of points where the environment of any one point is the same as the environment of any other point. These points can be located at the corners of the unit cell, in the center of the body (body-centered), or in the center of the faces (base-centered or face-centered). A space group is a symmetry group (set of symmetry elements) of a configuration in 3-D space which are used to exhaustively and exclusively classify crystalline materials. Once

atoms decorate the unit cell, applying the possible internal symmetries of pure rotations, inversion, reflections, screw rotation axes, and glide reflection planes leads to 230 possible space groups.

Materials with the same space group may have markedly different elemental compositions and coordinations, but typically they are highly related in structural motif and physical properties. For example, the trigonal space group, $R\bar{3}m$ (166), is the space group for both Herbertsmithite, $ZnCu_3(OH)_6Cl_2$, and $Na_2Ti_3Cl_8$.[19] These materials have different elements, valence electrons, and lattice parameters, but they both host the same underlying structural motif, the kagomé lattice, as well as similar magnetic responses. Furthermore, understanding the space group gives great insight into the structure, the first half of establishing a structure-property relationship.

1.4 The Structure-Property Relationship

Understanding structure-property relationships is at the heart of solid state chemistry. Some of the most interesting properties evolve from the coupling between mechanical, thermal, electrical, and magnetic responses. This phenomenon is known as reciprocity.[20] These coupled materials are extremely useful for a wide range of devices such as actuators, sensors, and memory storage. The coupling behavior of these materials is predicted and described by the laws of thermodynamics. By understanding each materials' thermodynamic state, we can draw relationships about its inherent properties.

The thermodynamic ground state (lowest energy most stable state under a given set of conditions) can be expressed in terms free energy (G) as a function of temperature (T), electric field (E_i), stress (σ_{ij}), and magnetic field (H_m).[21] Taking the first derivative of the system, equation 1.4, shows how the system will respond when exposed to certain perturbations.

$$dG = -SdT - \varepsilon_{ij}Vd\sigma_{ij} - P_i dE_i - B_\mu dH_m \tag{1.4}$$

By applying different controlled conditions (e.g. constant temperature or constant pressure) to the system, it is possible to rearrange the equations to solve for each parameter individually under those particular conditions. These first derivate responses are typical in all solid materials which vary in strength of coupling such as stress and strain ($\sigma_{ij} = C_{ijkl}\varepsilon_{ij}$) and polarization and electric field ($P_i = \eta_{ij}E_j$).

$$S = -\left(\frac{\partial G}{\partial T}\right)_{\sigma_{ij},E_i,dH_m} \tag{1.5}$$

$$\varepsilon_{ij}V = -\left(\frac{\partial G}{\partial \sigma_{ij}}\right)_{T,E_i,dH_m} \tag{1.6}$$

$$P_i = -\left(\frac{\partial G}{\partial E_i}\right)_{T,\sigma_{ij},dH_m} \tag{1.7}$$

$$B_\mu = -\left(\frac{\partial G}{\partial H_m}\right)_{T,\sigma_{ij},E_i} \tag{1.8}$$

By using Maxwell relations, it is possible to derive coupling relationships between these different responses by relating them through the second derivate of energy. For example:

$$\left(\frac{\partial S}{\partial E_i}\right)_{T,\varepsilon_{ij}} = -\left(\frac{\partial}{\partial E_i}\frac{\partial G}{\partial T}\right) = -\left(\frac{\partial^2 G}{\partial T \partial E_i}\right) = -\left(\frac{\partial}{\partial T}\frac{\partial G}{\partial E_i}\right) = \left(\frac{\partial P_i}{\partial T}\right)_{\varepsilon_{ij},E_i} \tag{1.9}$$

and since $\delta Q = TdS$ where Q is heat

$$\frac{1}{T}\left(\frac{\delta Q}{\partial E_i}\right)_{T,\varepsilon_{ij}} = \left(\frac{\partial P_i}{\partial T}\right)_{\varepsilon_{ij},E_i} = \rho_i \tag{1.10}$$

where ρ_i is the pyroelectric coefficient. This equation highlights the the pyroelectric effect, the coupling of a change in temperature of the bulk material to a bulk electric polariza-

tion. Similar relations can be found coupling other properties such as piezoelectricity and thermoelectricity as shown in Figure 1.4.1.[22**?**]

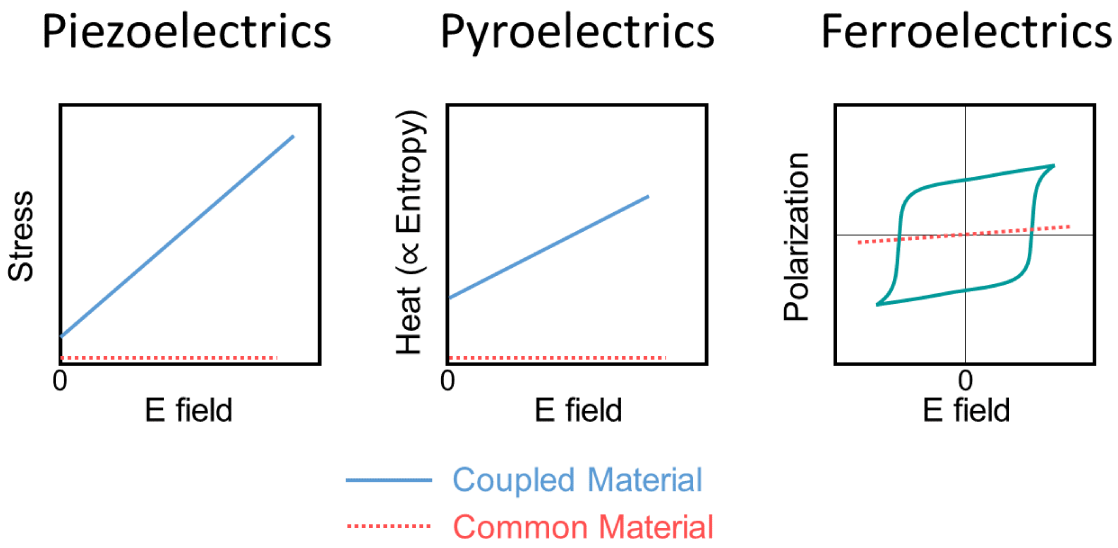

Figure 1.4.1: An illustration of typical physical response of a few materials with unique coupling relationships: piezoelectrics, pyroelectrics, and ferroelectrics.

Many of the possible degrees of freedom that alter the free energy of the material can be coupled through the Maxwell relations. It is important to realize that coupling coefficients can be derived for all materials however, in common materials these tensors are equal to zero. Maxwell's equations prove that these reciporical properties must coexist, but can not predict the magnitude of the cross coupling term. In order to predict and design these materials with strong coupling terms, we must develop additional theory to build a predictive model of property-structure relationships.

1.5 Magnetism and Correlated Electron Phenomena

1.5.1 Origins of Magnetism

The written record of the phenomenon of magnetism go as far back as the Greeks in the 6th century describing the behavior naturally found in lodestone (magnetite). Insight into the origins of magnetism remained limited until 1820 when Hans Christian Ørsted discovered that electric current induces magnetic fields (a useful feature that is utilized in magnetization measurements). Further advancements by André-Marie Ampére, Carl Friedrich Gauss, Jean-Baptiste Biot, Félix Savart, and Michael Faraday laid the ground work for James Clerk Maxwell who developed a theory that related electricity, magnetism and light known as Maxwell's equations.[10]

So what is the origin of magnetism in materials? The bulk magnetic properties arise from magnetic moments in electrons which originate from two sources: 1) the intrinsic spin of the electron and 2) negatively charged electrons orbiting the nucleus.[23, 24] Both of these effects are quantified into a single quantity, the magnetic moment, μ, which is defined as:

$$\vec{\mu} = \gamma^* \hbar \vec{J} = -g^* \mu_B \vec{J} \tag{1.11}$$

where γ is the gyromagnetic ratio, * designates a tensor, $\hbar$ is Planck's constant, μ_B is the Bohr magneton, and $\vec{J}$ is the total angular momentum. For free ions, the total angular momentum is simply $J = S + L$ and the values of S and L are predicted by using Hund's rules. However, the magnetic moment is not necessarily parallel to J so a vector model is used to describe the expectation value of the magnetic moment. More commonly, the magnetic moment is thought of in terms of Landé g factor, g, which is:

$$g = 1 + \frac{J(J+1) + S(S+1) - L(L+1)}{2J(J+1)} \tag{1.12}$$

And related to the effective magnetic moment by:

$$\mu_{eff} = p_{eff}\mu_B = g\mu_B\sqrt{J(J+1)} \tag{1.13}$$

Both the spin angular momentum, S, and the orbital momentum, L, contribute to the magnetic moment. If spin angular momentum is the sole contributor to the magnetic moment then $g = 2$, conversely if orbital angular momentum is the lone contributer then $g = 1$. The value of g is typically between 1 and 2 for magnetic ions. The experimentally observed magnetic moments for lanthanide ions are in good agreement with the above formula using total angular momentum. However, the situation changes for ions with incomplete d shells such as first row transition metals where the magnetic moments are much smaller than the value predicted by equations 1.12 and 1.13. For transition metals, the experimentally determined effective magnetic moment is more accurately described by only considering spin angular momentum where:

$$\mu_{eff} = p_{eff}\mu_B = 2\mu_B\sqrt{S(S+1)} \tag{1.14}$$

This is referred to as the quenching of the orbital angular momentum. Consider a simple picture where orbital angular momentum arises from degenerate symmetry related orbitals which are only partially filled by electrons, as the case would be in a d^1 ion in free space. In real solids, these magnetic metal ions experience a crystalline electric field from the coordinated lattice. To reach a lower energy state, the orbitals will under go crystal field splitting (and in some cases more substantial distortions such as Jahn-Teller distortions) relieving degeneracy. Since degeneracy is broken, electrons can no longer sample other d orbitals without paying an energy cost. So the crystal field splitting effectively quenches the orbital contribution to the momentum. In the lanthanide compounds, the atoms are large and the valence orbitals are in close proximity to the nucleus effectively shielding it from the crystal field effects to conserve orbital momentum.[1]

1.5.2 Effective Models with Magnetism

During the introduction, theory was discussed as a pillar of the material life cycle. To relate the ”real physical world” to theory, science uses models: constructs that represent a simplified version of real world phenomena/objects. The goal of theory is to develop a first principle framework (i.e. model) to predict desirable properties and provide experimentalist a road map to discover new phenomena. The best models are descriptive, explanatory, and predictive.

Models can either be built from the top-down or from the bottom-up. The top-down approach is done for weather models, where scientists examine historical data, extract common laws and trends, and scale specific contributions from different weather principles to predict weather patterns. These models are continually adjusted and refined using real world data to improve the model's accuracy. Machine learning is also an example of a top-down approach.

The bottom-up method is achieved through constructing a model based on first principles, a set of fundamental principles which are assumed to always be true. These types of models are common in fundamental physics. The tight binding model (described earlier) is a bottom-up model using atomic orbitals as a first principle. Crystalline materials are particularly well suited to test theoretical models built from first principles. Their geometric lattice and periodicity bode well for the construction of highly descriptive models with relatively straight forward mathematics. In order for models to be predictive and useful, condensed matter theory must construct a model which can be ”solved” either exactly or numerically. The summation of a model's components is written down as a Hamiltonian, and the Hamiltonian is used to calculate predicted physical properties and exotic behaviors that ought to manifest in the ”real world.” [6]

For solid state materials, models take into account fundamental quantum considerations, such as charge, spin and energy, as well as spatial arrangements and orientations. For magnetic materials in particular, models are derived by combining magnetic moments on a

lattice. The typical geometric lattices are 1D, 2D, and 3D structures composed of dimers, triangles, squares, and hexagons.[25] The challenge for experimentalist is not only to realize the model's structural motif in a real material, but also to consider specific elements and oxidation states to obtain the proper magnetic interactions.[26]

1.5.3 Exchange Interactions

In free magnetic ions, distance prevents spins from interacting so the spins behave independently (paramagnetically) down to low temperatures. Once you begin to move the atoms closer together, the orbital overlap increases and the magnetic moments begin to interact with one another. This is called exchange interaction denoted by J_{ij}. If $J < 0$ then anitferromagnetic (opposing spins) exchange dominates while $J > 0$ results in ferromagnetic exchange (spins align).[24]

Classical Spin Models

Classical spin models consist of a lattice with "spin" degrees of freedom at the vertices. Three common models for magnetic materials are the Ising, *XY*, and Heisenberg model.[25, 27, 28] Consider the Ising model where magnet moments are periodically arranged on an extended lattice. The energy of the system depends on the interaction, J_{ij}, between the neighboring spins, σ_i and σ_j. In this model, the spin only has one degree of freedom: spin up, $S = 1/2$, or spin down, $S = -1/2$, along a z-axis. Considering one exchange strength and only nearest neighbors, the energy of the system would simply be the sum of all of the interaction across the system as shown in Figure 1.5.1. Allowing additional spin degrees of freedom generates the *XY*-model and the Heisenberg model with two and three degrees respectively. Models can also be made more complex by considering different lattice geometries, exchanges between next nearest neighbors (NNN), next next nearest neighbors (NNNN), and so on, and multiple interactions with different J_{ij} values.

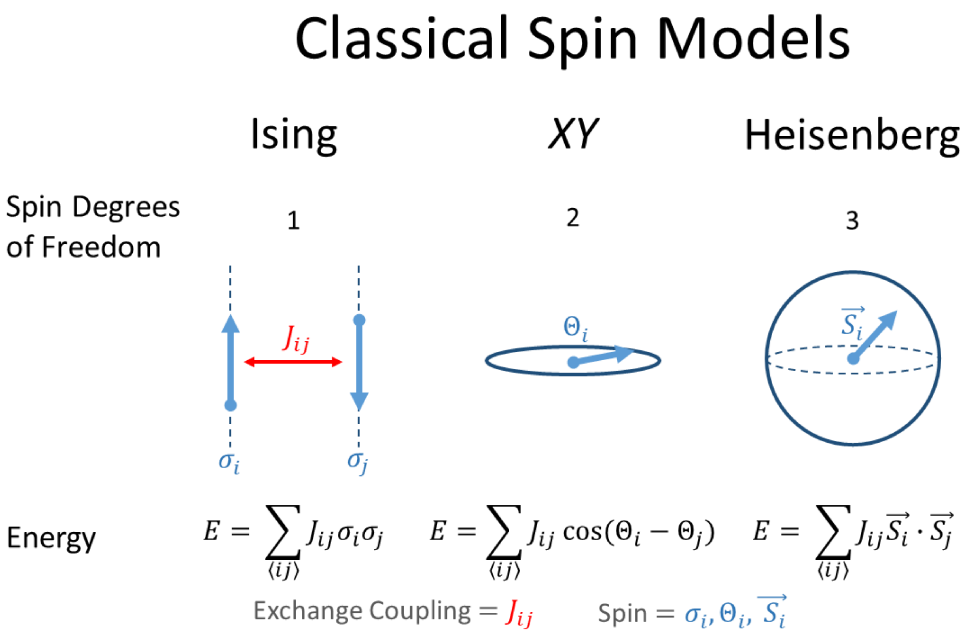

Figure 1.5.1: Schematic depictions and total energy equations of three simple models of interacting spins on a crystalline lattice by increasing spin degrees of freedom: Ising, *XY*, and Heisenberg models respectively

The summation of all the exact local geometries becomes extremely complicated very quickly as site number increases. Therefore one approach to make these models useful is through a mean-field approximation. Instead of feeling individual spin-interactions, every spin-site feels a net isotropic spin field. In this approximation, it is assumed that the neighbors of a given spin are ”typical” and they all reflect the same mean spin-interaction field. Since every spin is feeling the same surroundings, the energy of the system only depends on the ratio of spin ”ups” to spin ”downs.” Using statistical mechanics, a partition function can be generated for a given model and can be used to predict of magnetic behavior and features in other physical properties, such as heat capacity. Some of the most interesting and potentially realizable models, such as the $S = 1/2$ kagomé , are quite complex and have not been solved exactly. In these cases powerful computational techniques must be used to approximate properties numerically.

Determining J: Direct Exchange, Superexchange, and Indirect Exchange

Exchange interactions are the driving force for magnetic order in solids. But what determines the size and magnitude of a given exchange interaction, J_{ij}? Strong magnetic exchanges can be understood through local interactions of bound electrons, and delocalized interactions of conduction electrons. Driven by the competition between Pauli exclusion and Hund's rule, the local interactions are dependent on the degree of orbital overlap and orbital orientations.[29] Two possible mechanisms to mediate local interactions of bound electrons are through direct exchange and superexchange.[30, 31] In direct exchange, the d orbitals of two transition metals overlap and the electrons align antiparallel (antiferromagnetically) to satisfy Pauli exclusion (Figure 1.5.2**a**). If direct orbital overlap is weak, exchange can occur through bridging ligands, via the process of superexchange. An excellent example of indirect exchange is displayed in the magnetic transition metal-oxides (Figure 1.5.2**b**) which are well described by the Goodenough-Kanamori-Anderson (GKA) rules. These materials are insulators so the magnetic properties are due to localized electrons which states can be approximated by atomic orbitals. As the geometry of the metal-oxygen-metal changes from 90° to 180°, the overall magnetic moments go from aligned (ferromagnetic) to antialigned (antiferromagnetic).

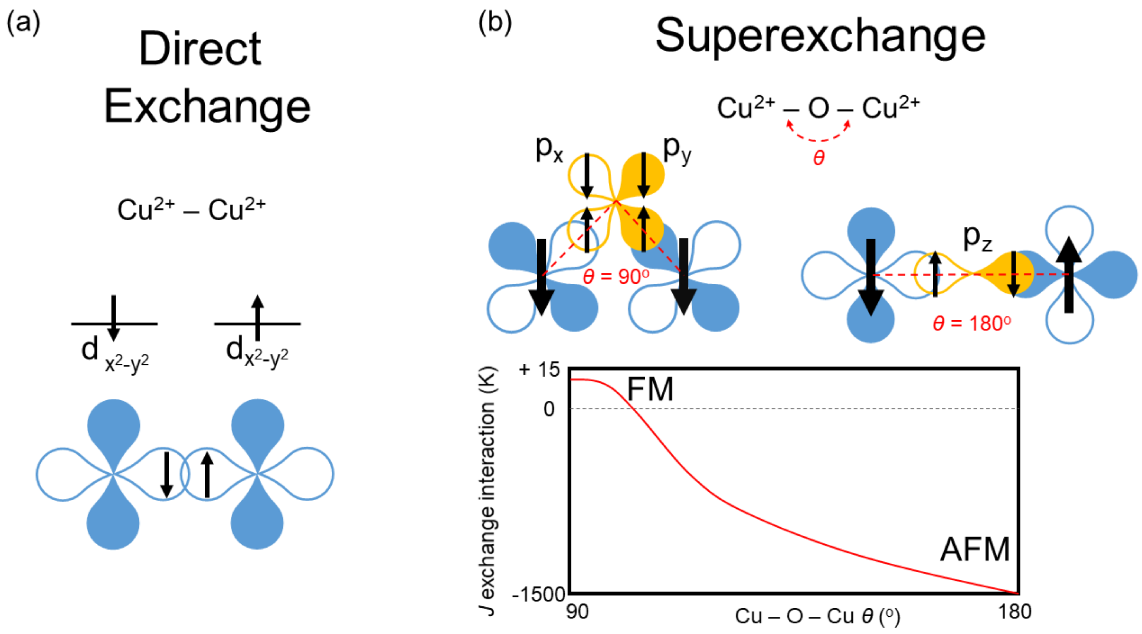

Figure 1.5.2: **a** Illustration of direct exchange between the $d_{x^2-y^2}$ orbitals of two copper ion. **b** Schematic depicting superexchange between coppers through oxygen p orbits. As the angle of the Cu-O-Cu bond changes from 90°to 180°, the exchange changes for a ferromagnetic interaction to an antiferromagnetic interaction as shown in the illustration below.

Indirect exchange interactions, called Ruderman-Kittel-Kasuya-Yosida (RKKY) interactions, is a system with an exchange between localized and delocalized electrons.[32] The localized magnetic electrons interact with the spin of surrounding conduction electrons which in turn interact with adjacent localized magnetic electrons. This leads to long range correlations which give rise to certain magnetic properties such as the Kondo effect. Purely delocalized electrons can also couple to spontaneously polarizing one spin over the other leading to a band ferromagnetism as seen in iron metal.

Types of Magnetism

All of these interactions lead to five major types of long range magnetic ordering: diamagnetism (DM), paramagnetism (PM), antiferromagnetism (AFM), ferromagnetism (FM), and ferrimagnetism (Ferri M). Diamagnetism occurs in materials with completely filled shells where all the electrons are paired up resulting in essentially no net moment. Para-

magnetism is present in materials which have magnetic moments, however the interaction between the moments is $J \sim 0$. Therefore the moments behave independently similar to a moment on a free ion. As discussed in the previous section, antiferromagnetism is an antialignment of magnetic moments where $J < 0$. Although the magnetic exchange is some cases is very strong, the net moment of the material is zero. Ferromagnetism, where $J > 0$, leads to an alignment of moments giving an overall moment to the material. Ferrimagnetism is a case where the interaction between sites is antiferromagnetic, but the magnitude of the moments on adjacent sites are unequal. Therefore the moments will not completely cancel out and there will be a net magnetic moment.

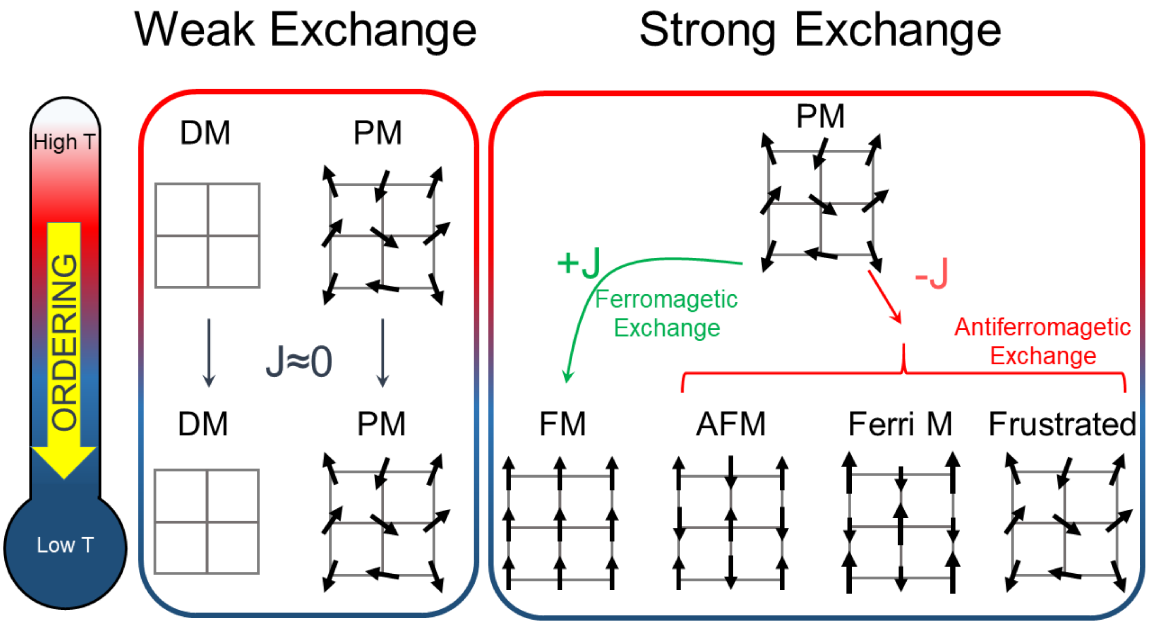

Figure 1.5.3: An illustration of the effect of temperature on magnetic ordering. In systems with weak exchange interactions, such as diamagnets or paramagnets with $J \sim 0$, there is no magnetic phase transition upon cooling. Typically when a system with strong exchange cools to a temperature where $k_B T \sim |J|$, it under goes a magnetic phase transition to order in a magnetic ground state such as a ferromagnetic, antiferromagnetic, or ferrimagnetic state. However, systems which have strong exchange interactions but do not order until temperatures where $k_B T \leq |J|/10$ are considered magnetically frustrated.

In the late 19th century, Pierre Curie (husband of the eminent scientist Marie Curie), whom the Curie-Weiss law is partly named after, pioneered the relationship between tem-

perature and magnetic phases. Typically, magnetic materials (with a strong exchange) order when cooled to low temperatures (Figure 1.5.3). When the material is at high temperatures where $k_BT > |J|$, thermal fluctuations completely overtake the exchange interactions, and the magnetic state looks like a non-interacting paramagnet. A magnetic phase transition, transformation from one magnetic state to another (such as paramagnetic to ferromagnetic state), can occur when the exchange interactions become non-negligible around $k_BT \sim |J|$ in magnetic materials. Upon cooling below that temperature, the system magnetically orders. At $T = 0$, the material will assume its ground state, lowest possible energy conformation. Examples of magnetic ground states are systems with perfect antiferromagnetic, ferromagnetic, or ferrimagnetic ordering.

However, there are magnetic systems with a strong exchange interactions that do not magnetically order even when cooled orders of magnitude below the expected transition temperature. This emergent phenomena is known as magnetic frustration.

1.5.4 Geometric magnetic frustration

Frustration occurs when a system can **not** fully satisfy all the magnetic interactions when cooled to its ground state.[33] Systems with a low degree of frustration, such as simple ferromagnets, readily assume a unique ground state by aligning all of its spins. Common ferromagnets, antiferromagnets, and ferrimagnets on a square lattices are examples of materials with minimal frustration as they reach a highly ordered and unique magnetic ground state on cooling (Figure 1.5.3). Highly frustrated systems contain strongly competing interactions which prevents all magnetic interactions from being simultaneously satisfied resulting in a large degeneracy of ground states. This large degeneracy is the underlaying mechanism of frustration. Since ferromagnetic interactions can be satisfied without frustration on any lattice, antiferromagnetic interaction must be present in order to develop frustration.[34] The two primary pathways to frustration are through disorder (spin-glass) or geometric frustration. This dissertation primarily focuses on the later.

To understand the nature geometric magnetic frustration, lets revisit the Ising model.[35] Consider the following 2-D lattices: a square lattice and a triangular lattice decorated Ising spins at the vertices with strong antiferromagnetic interactions(Figure 1.5.4). In the square model, all the pairwise interactions are simultaneous satisfied, resulting in two fully satisfied degenerate ground states. On the other hand, the two neighboring spins on the triangular lattice are unable to be simultaneously satisfied, leading to six degenerate states on a single triangle. If you expand the square lattice in two dimensions, it will still have only two degenerate ground states. While extending the triangle into a 2D lattice will lead to a rapidly increasing number of degenerate ground states as more triangles are added to the lattice. This highlights the nature of geometric frustration, where geometric constraints physically inhibit complete ordering and lead to large ground state degeneracy.

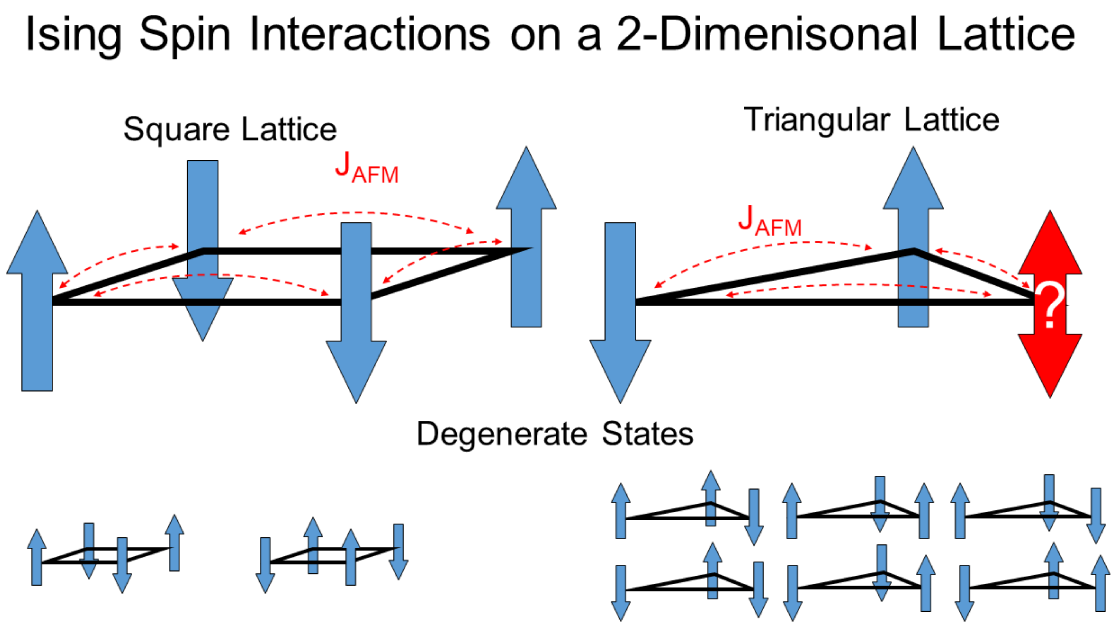

Figure 1.5.4: Square and Triangular lattices decorated with Ising spins. The red double arrow highlights the frustration in the triangular lattice.

Expanding the spin degrees of freedom to allow for either *XY* or Heisenberg exchange (see section 1.5.3), the ground state can adopt a classical 120°state where all the spins are pointed 120°away from their nearest neighbors and partially satisfy the antiferromagnetic

interactions. Frustrated systems can also break degeneracy and limit frustration through a distortion, elongating its triangles similar to a Peierls or Jahn-Teller distortion, to reach a unique ground state. This is one of the reasons it is difficult to find geometrically frustrated materials with a perfect undistorted lattice.

Types of Geometrically Frustrated Lattices

There are several geometrically frustrated systems which differ in connectivity and dimensionality as shown in Figure 1.5.5. Triangles are the primary building block of geometrically frustrated lattices.[34] The highest connectivity lattices, the triangular lattice and pyrochlore lattice each having 6 nearest neighbors, contain edge-sharing equilateral triangles. In 2D, the connectivity can be reduced to 4 by removing $\frac{1}{4}$ of the sites from the triangular lattice to produce the corner-sharing kagomé lattice. The 3D analog of the kagomé is called a hyper-kagomé lattice.

The lowest connectivity lattice, the honeycomb lattice, is pseudo-triangular and can be derivied from the triangular lattice by removing $\frac{1}{3}$ of the magnetic sites. Although not intrinsically frustrated by geometry alone, honeycomb which have a specific configuration of exchange interactions have been shown theoretically and experimentally to display magnetically frustrated behavior. One frustrated honeycomb model is the Kitaev model. Here, each vertice on the honeycomb has mutually independent exchange interactions along the x, y, and z directional bonds resulting in overall frustration (the x, y, and z directions in the honeycomb are represented by different colors in Figure 1.5.5).

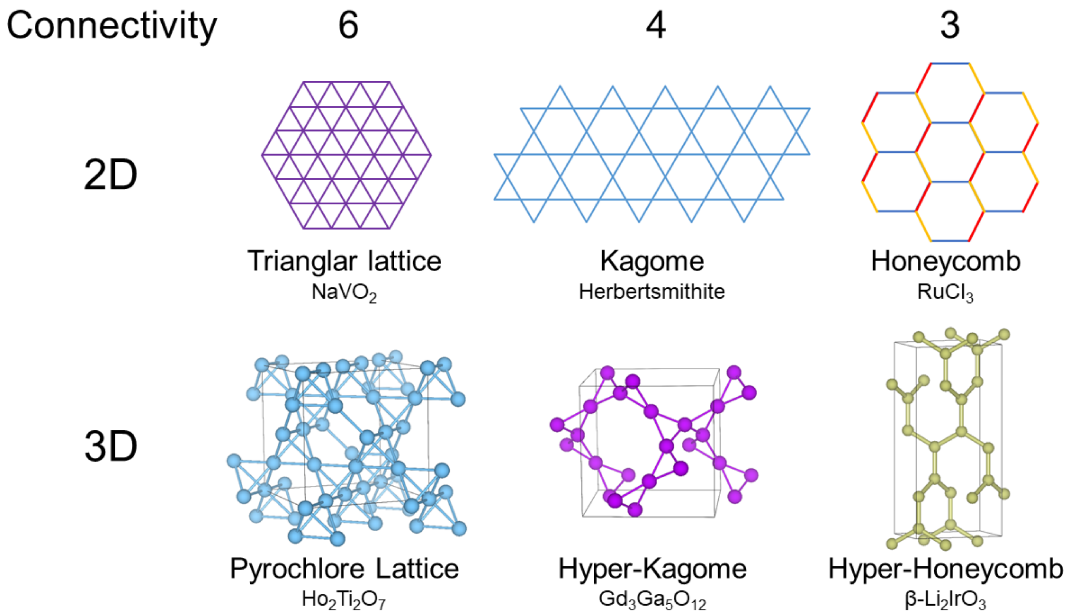

Figure 1.5.5: Magnetically frustrated lattices with strong nearest neighbor antiferromagnetic exchange ($J < 0$) displayed as nearest neighbor connectivity vs. dimensionality. The spins are located on the vertices. Examples of real versions of these lattices are presented below each representation.

Two magnetic kagomé compounds, Herbertsmithite and $Na_2Ti_3Cl_8$, and derivatives of the honeycomb compound $Sr_3CaIr_2O_9$ are investigated in this manuscript. Although the systems have notably different behavior (which will be described in detail in the following chapters), they all hold promise as candidates to host exotic quantum states and exotic properties.

1.5.5 Exotic Quantum Ground States

The major driving force for discovering new geometrically frustrated systems is due to their highly degenerate ground state. These ”quantum” ground states have the potential to host exotic quantum properties that are delocalized over the entire material giving rise to interesting and useful emergent phenomena.[36–40] Holding promise for quantum computing and high temperature superconductivity, the quantum ground states which motivated the work in this manuscript are the quantum spin liquid (QSL) state and the 2D valence bond

solid.

The Quantum Spin Liquid (QSL) State

The quantum spin liquid (QSL) state is predicted to be found in magnetically frustrated materials where quantum fluctuations drive the highly correlated magnetic moments to fluctuate avoiding order even at absolute zero. The QSL state may be an underlaying parent state for high temperature superconductivity.[17]

The two most promising theoretical models to host a true QSL state are the S = 1/2 kagomé and the S = 1/2 Kitaev model.[41, 42] In a purely classical kagomé system, the system would assume a 120°ground state at $T = 0$ K. However, strong quantum effects on the S = 1/2 kagomé lattice prevent this order due to strong quantum fluctuations from resonating valence bonds. These resonating valence bonds are pairs of electrons forming singlets that are able to hop throughout lattice between different resonance states without an energy barrier. It is theorized that these bonds are not limited to nearest neighbors, but also expand across the entire lattice.[43] The result is a superposition where every spin is forming a singlet with every other spin, leading to constant fluctuations at absolute zero, the quantum spin liquid state. This QSL state has been proven mathematically in the Kitaev model also. The Kitaev model consist of a honeycomb lattice that has spin exchange parameter dependent on direction leading to the emergence of a QSL state. One of the most appealing and exciting aspect of the Kitaev model is that it can be solved exactly, unlike the vast majority of other frustrated models.

In terms of real world material which meet the requirements of the theoretical models, Herbertsmithite is the best candidate. Synthetic Herbertsmithite contains a perfect kagomé lattice of S = 1/2 Cu^{2+} (d^9) ions and displays experimental signatures of the QSL state.[44, 45] More recently, other real material candidates have been discovered which have structures that closely resemble the Kitaev model. Currently, no material discovered fits *all* the requirements to host Kitaev QSL state. The closest candidates to date are $RuCl_3$

and honeycomb iridates with strong spin-orbit coupling, although they fall short of the perfect type of exchange needed to fully test Kitaev's theory.[46–48]

Another appealing aspect of the QSL state is its theorized connection with high temperature superconductivity. QSL materials are Mott insulators. Anderson proposed that by doping a QSL material, Figure 1.2.4 **d**, it will reach an electronic state where the electron pair in the valence bond will be physically mobile to conduct, analogous to copper pairs in the superconducting state . Ever since, there has been interest in synthesizing QSL materials and their doped counterparts to explore possible superconducting states.

2D Valence Bond Solid

Although frustrated systems with half integer spins (i.e. $S = 1/2$) have dominated the frustrated magnetism literature, there is growing interest in integer spin frustrated systems as well.[49] Consider a 1D chain of high spin $S = 1$ titanium ions (d^2) with antiferromagnetic Heisenberg exchange between atomic sites as shown in Figure 1.5.6 **a**. Each Ti atom host two valence electrons. The two electrons form a triplet which gives rise to the overall $S = 1$ on each atom. Between the atoms, there are bonds where electron 2 on atom one forms a singlets with electron 1 on atom two and electron 2 of atom two forms a singlet with electron 1 on atom three and so on down the chain. This system can be represented through electron interactions where the two electrons on the ion form a high spin triplet state (pink ovals) and the bonds between the ions form a singlet (dark blue lines in Figure 1.5.6 **b**), similar to the direct exchange discussed earlier in section 1.5.3. For chains that form a ring, the system can reach a unique ground state. But in the chain terminates, it produces unpaired $S = 1/2$ edge states and behaves as a $S = 1/2$ free spin even though the system is composed on only $S = 1$.

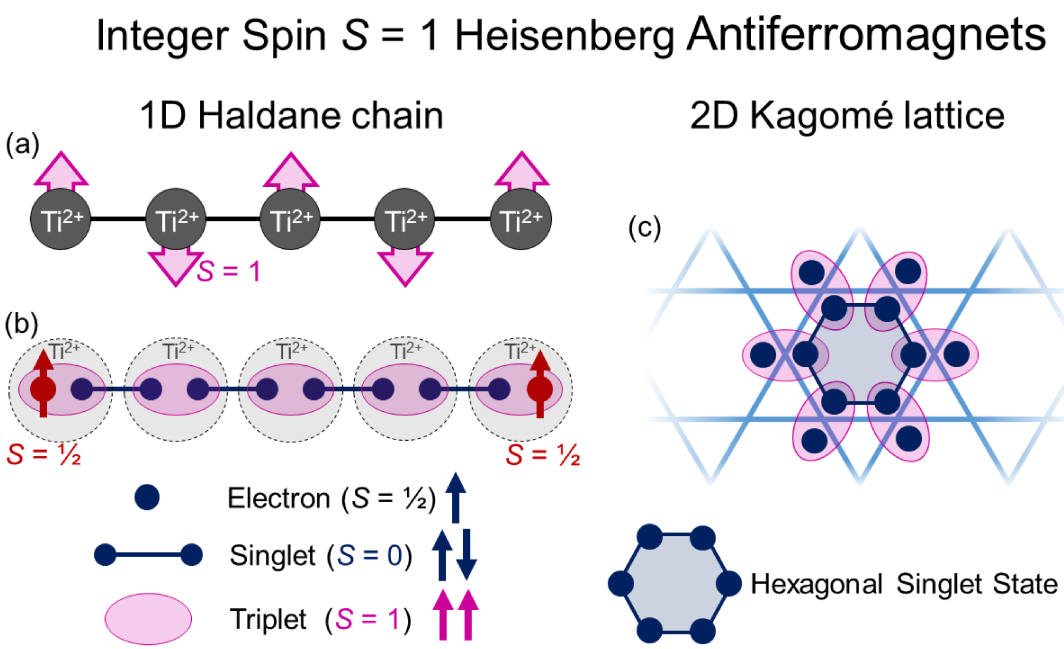

Figure 1.5.6: **a)** A simple representation of a 1D chain of high spin $S = 1$ Ti ions with two valence electrons (d^2). **b)** An electron interaction representation of the same Ti 1D chain. The two electrons localized on each ion (displayed as dark blue dots) form a triplet state (depicted as a pink oval). Bonds also form between the Ti ions where electron 2 on the first Ti atom forms a singlet bond with electron 1 on the second Ti atom and electron 2 on the second Ti atom forms a bond with electron 1 on the thrid Ti atom, and so on down the chain. At the edge of the 1D chain, it terminates with $S = 1/2$ spins (red) forming $S = 1/2$ edge states. **c)** a 2D kagomé representations of the valence bond solid state. In the 2D kagomé , the lattice separates the $S = 1$ triplet states by 120° leading to hexagonal singlets throughout the kagomé lattice. It will also produce $S = 1/2$ edge states at the terminus of the layer (not shown).

Figure 1.5.6 **c** shows the 2D valence bond solid construction on a $S = 1$ kagomé lattice. The 120° orientation of the of the bonds produces cyclical singlets tiled over the lattice. This is known as the hexagonal singlet state. The $S = 1/2$ edge states have been experimentally observed in *m*-MPYNN - BF_4 and CaV_2O_4, but the hexagonal singlet state has yet to be detected experimentally in a known material.[50–52]

1.6 Phase Transitions

1.6.1 Ehrenfest Classification

The different physical forms of water are observed everyday in the world: flowing water in rivers, the steam coming off a cup of tea, or the ice on a sideway on a cold winter's day. The different states of water (e.g. steam-gas, water-liquid, and ice-solid) are known as phases. Every phase has its own defining set of properties and spontaneously exist under specific conditions.[21] The spontaneous transformation from one phase to another is a phase transition. Phase transitions are by no means limited to transformations between solids, gases, and liquids. In solid state chemistry, examples of phase transitions include structural distortions like the tetragonal to cubic transformation in pervoskites, magnetic transitions such as the ferromagnetic to paramagnetic transition on warming, and electronic transitions in Mott insulators as they transform from a metallic to insulating state. One useful method to understand the different phases of a material is to map its state as a function of a variable (i.e. temperature, pressure, magnetic field) to construct a phase diagram. Phase diagrams are graphical representations of thermodynamically stable domains under given conditions for a system in equilibrium. These diagrams give insight into the free energy surfaces of the phases and can be used to determine the occurrence and nature of phase transitions.

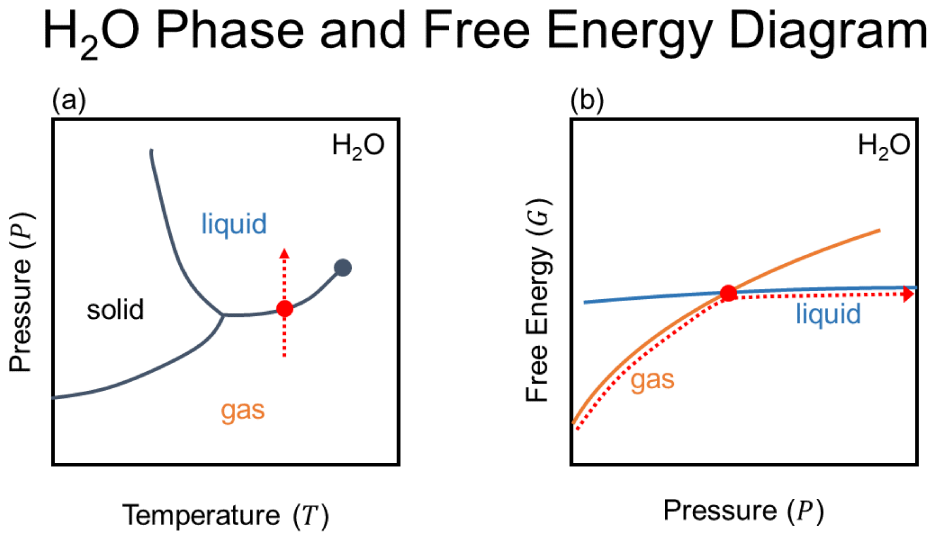

Figure 1.6.1: a) an illustration of the pressure (P) vs. temperature (T) phase diagram of water. **b)** The free energy (G) of the gas phase and the liquid phase as a function of pressure.

Consider the phase diagram for water as a function of pressure and temperature shown in Figure 1.6.1**a**. Under isothermal conditions, H_2O can be transformed from gas to liquid by increasing the pressure as denoted by the red dotted arrow transversing the coexistance line. At the coexistance line, the free energy of gas and liquid phase are equal. Below this pressure the gas phase is at a lower free energy than the liquid phase so it will spontaneously transform to the gas phase where the opposite is true above this pressure. This type of transition with a clear demarcation between phases is known as a first order phase transition under Ehrenfest's classification.[53] One important characteristic of first order phase transitions is that they have latent heat. This is due to the coexistence of multiple phases with different entropies during the transition, so the system must absorb or release heat. Examples of first order phase transitions include melting, freezing, vaporization, condensation, sublimation, and deposition. The order of the transition refers to the order of the free energy derivate where discontinuity is first observed. A second order phase transition occurs when the first derivative of the free energy is continuous but becomes discontinuous

for higher order derivatives (Figure 1.6.2). Second order transitions occur continuously throughout the transformation without the coexistence of two distinct phase and therefore do not have a latent heat. Examples of second order phase transitions are certain superconducting transitions and the β-brass order to disorder transition.

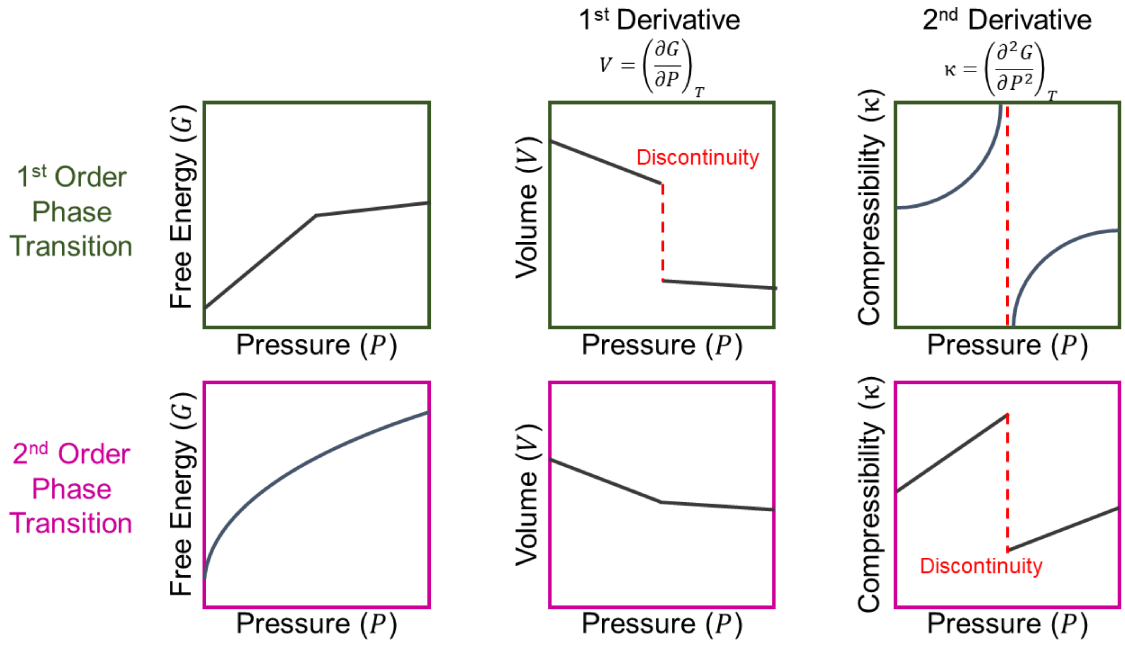

Figure 1.6.2: Graphical representations of a first order and second order phase transition in terms of free energy. The first and second derivatives are shown to demonstrate the difference in the occurrence of the discontinuity.[**?**]

1.6.2 Landau Theory of Phase Transitions

Another way to understand the nature of phase transitions is through Landau theory which considers the change in symmetry through the transition. As discussed in section 1.3, crystalline materials can be described by space groups, which are a specific set of symmetry operations. In the majority of phase transitions, the system undergoes a change in symmetry.[54] Similar to Ehrenfest classification, a first order phase transition is accompanied by latent heat and its thermodynamic quantities are discontinuous whereas continuous transitions without latent heat are considered second order. Imagine a system that is being cooled through a phase transitions. The high temperature (i.e. parent) phase has a lot of

thermal energy so it is more disordered resulting in a higher symmetry. On cooling, the thermal energy is removed from the system so that the atoms can order lowering its symmetry. Landau proposes that this transition can be characterized by the symmetry elements that we lost during this symmetry lowering process through a linear combination of symmetry modes. Symmetry modes represent a collective movement of atoms that is forbidden in the parent phase but allowed in the lower symmetry phase. These symmetry modes are represented by irreducible representations (irreps).

1.6.3 Intro to Mode Decomposition Analysis

Mode decomposition analysis is used to identify the activated symmetry modes during a symmetry lowering phase transition. ISODISTORT is a program that calculates these symmetry modes using the symmetries of the parent and distorted phases.[55] Symmetry modes are broken down by specific elements and are quantified in a scalar quantity. These modes help determine the mechanism of the phase transition as well as newly allowed physical characteristic given the change in space group. This analysis is extensively used for $Na_2Ti_3Cl_8$ in later chapters.

2 Methods

2.1 Synthesis Techniques

2.1.1 The Thermodynamics of Solid State Reactions and Inherent Limitations

Thermodynamics enables the comparison of the stability of different equilibrium states in materials. Not only is it an excellent framework to understand the phase of a material as discussed earlier, but it also gives insight into the effect of temperature on the concentration of defects and whether a certain reaction will proceed. The overall phase stability is quantified by the difference in Gibbs free energy (ΔG) as:

$$\Delta G = \Delta H - T\Delta S \tag{2.1}$$

Where ΔH is the change in enthalpy, ΔS is the change in entropy, and T is temperature.[21] For any system, the equilibrium state that gives the largest negative ΔG is the thermodynamic product and will be the most stable under thermodynamic conditions.

Thermodynamics is limited to systems in equilibrium, so it does not directly provide information of the relative energy barrier that must be overcome for a reaction to reach its thermodynamic ground state. Unlike vapor and solvated reactions, diffusion results in a major energy barrier for reactivity in solid state materials. To overcome the diffusion barrier, samples are ground into fine powders, pressed into pellets, and heated to very high

temperatures, affectionately known as the ”shake and bake” method. By applying a large amount of heat (1200-3000 K), the system can overcome the large energy barriers and settle into the most thermodynamically stable product. This is called thermodynamic control.

Thermodynamic control is an excellent method to target the most stable phase of a material. But many reactions also have possible meta-stable states which hold desirable structures and potentially exciting properties. Meta-stable states are phases at relatively higher energies then the thermodynamic minimum phase and must be kinetically trapped to isolate the phase. Over the years, solid state chemistry has developed strategies to access these other phases through low temperature crystal growths and quenching of high temperature phases. However these methods are quite limited in the degree of phase space they make available.

2.1.2 Chimie Douce Topochemical Reactions

Kinetically controlled reactions

A more innovative approach to synthesizing new solid state materials is using a low-temperature topotactic reaction. These so-called soft chemistry reactions are kinetically controlled, and therefore open up new pathways to attain metastable products that are inaccessible under high-temperature thermodynamically-controlled syntheses.[56, 57] Advances in this field have yielded multiple soft chemistry strategies to selectively create materials with unique atomic structures and precise compositions while circumventing less desirable phases.[56, 58] The soft chemistry portfolio of low temperature techniques has emerged as an ideal tactic to synthesize metastable magnetically frustrated materials.[59]

Intercalation/Deintercalation

Redox reagents, although commonly used in organic chemistry, are utilized to a much lesser extent in solid state chemistry. Those who research battery materials often use controlled

potential electrolysis to drive ions in and out of layered solid state compounds. The process of inserting mobile ions into a solid from an electrolyte is called intercalation (where deintercalation is the removal of mobile ions). Redox reagents can also be used to drive this ion exchange.[60] For example, by applying correct formal potential, $E^{o\prime}$, in solution, one can reduce the parent phase with subsequent ion intercalation to achieve a new meta-stable material.

$$A + Ox \leftrightharpoons A^+ + Red^- \tag{2.2}$$

$$K_{eq} = [A^+][Red^-]/[A][Ox] \tag{2.3}$$

The reduction solution of the benzophenone anion radical and alkaline metal is an particularly useful for this aim.

$$Ph_2CO + Li^0 \leftrightharpoons [Ph_2CO]^- + Li^+ \quad Ph_2CO/[Ph_2CO]^- \; E^{o\prime} = 2.2\ V \tag{2.4}$$

$$[Ph_2CO]^- + Li^0 \leftrightharpoons [Ph_2CO]^{2-} + Li^+ \quad [Ph_2CO]^-/[Ph_2CO]^{2-} \; E^{o\prime} = 2.9\ V \tag{2.5}$$

The benzophenone anion radical (BPA) is prepared in situ in THF in the presence of an alkaline metal, such as Li. The metal readily gives up an electron to form BPA and dissolves to produce a dark blue solution indicative of the anion radical. Adding 25-100% excess Li results in a purple solution due to the presence of the dianion radical. The ability to create both the anion and dianion allows for some flexibility in tuning the overall potential. The adjustment of concentration, anion:dianion ratio, duration, and temperature provide additional tuning parameters for the precise control over the reaction conditions and allow for the exploration new phase space.

Oxidizing agents also tend to be underutilized in solid state material synthesis. Halogens such as I_2 and Br_2 are weak oxidants that are highly soluble and colored in a variety of solvents. Unlike the benzophenone anion radical reactions, which are often run in excess, it is

relatively straight forward to control the precise [I_2] concentration to partially deintercalate on a mole to mole basis.

Metal Hydride Reduction

Exploiting different solid state diffusion rates is another strategy to exert kinetic control. Cations such as H^+, Li^+, Na^+, and Ca^{2+} along with anion species like O^{2-} and F^- are typically very mobile in solids relative to the metal lattice framework. This allows for the removal and replacement of these anions and cations while maintaining the metal framework.[59, 61] This can be achieved through reduction with metal hydrides. Metal hydrides have been used extensively in 3d transition metal pervoskite oxides to produce new materials with unique metal coordinations and valency while maintaining the underlaying structure. Hydride reactions with 5d transition metals have been a greater challenge as demonstrated by $Sr_3CaIr_2O_9$ discussed in the last chapter.

2.1.3 High Pressure Synthesis

Hydrothermal Reactions

Hydrothermal acid digestion vessels (i.e. bombs) shift the reaction into a new dimension of reaction coordinate space by significantly modifying pressure. This allows for the stabilization of phases that are not achievable at ambient pressures. A hydrothermal bomb consists of a Teflon cup (typically 23 mL) with a lid which is sealed inside a steel casing, where the top is tightened to seal the Teflon liner. Reactions consists of various soluble and insoluble solid starting materials and a solvent (both aqueous or nonaqueous). The cup is filled only up to approximately $\frac{1}{3}$ to $\frac{1}{2}$ full order to leave head space and avoid over pressuring the vessel. The reactions are carried out from 80-250 °C for a few days for polycrystalline powders to multiple weeks for single crystal growths.

Cubic Anvil Cell

Similar to hydrothermal reactions, the cubic anvil high-pressure apparatus is a technique which grants access to very high pressure phases. It is capable of reaching pressures of 1-7 GPa which is on the order of the pressure felt deep in the earths crust (deepest point in the ocean is 0.1 GPa). The sample preparation for the cubic anvil cell is shown in Figure 2.1.1 **a**.[62] The sample is wrapped in platinum (Pt) foil to prevent any reactions with the boronitride (BN) sleeve which act as a chemically inert and highly electrically resistive reaction vessel. The sample and BN sleeve are then placed inside a graphite cylinder. The graphite (being more conductive than BN) acts as a resistive heater around the sample and can achieve temperatures ranging from 800-1500 °C. The graphite is then sandwiched between graphite disks, molybdenum (Mo) disk, and pyrophylite caps with steel rings and placed into a cubic pressure transfer medium, pyrophylite. The steel ring - Mo disk - graphite - Mo disk - steel ring stack creates an electrical circuit passing through the graphite so resistive heating can easily be applied.

The prepared sample is then placed in between 6 anvils, one for each side of the cube. The bottom anvil is stationary while the top anvil is pressed downwards. This downward motion also presses down the sloped outer bodies the horizonal anvils, pressing them into the sample (shown in Figure 2.1.1 **b** covered in a protective white plastic coating). This geometry allows for isotropic pressure to be applied on every side of the cube. Once the instrument reaches the desired pressure, the vertical anvil is electrically charged to pass current through the graphite to heat the sample. High pressure reactions times are much shorter than ambient pressure reactions and range from 0.5-6 hours. The pressure forces the reactants to be in excellent close contact increasing the overall rate of diffusion.

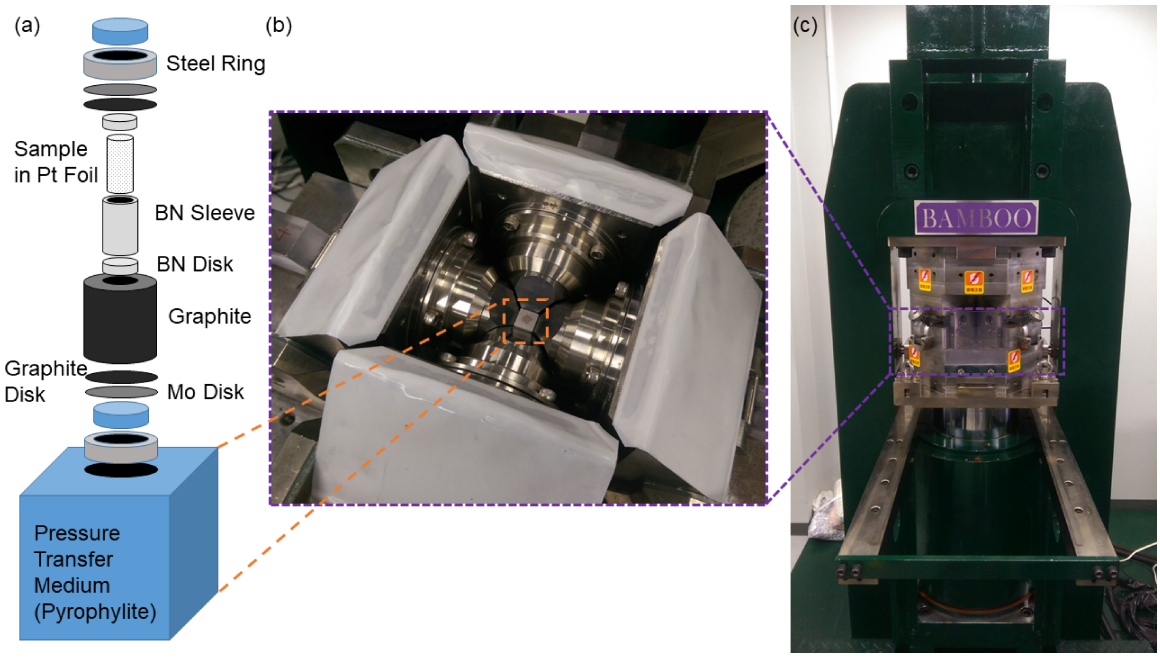

Figure 2.1.1: The cubic anvil high-pressure apparatus at the Kyoto University. **a)** An illustration of the sample preparation for high pressure synthesis. **b)** A photograph of the cubic anvil geometry and sample placement and **c)** the top anvil applying isotropic pressure against all 6 faces of the cubic pressure transfer medium.

2.2 Structural characterization

2.2.1 Diffraction

Bragg's Law

Diffraction is a powerful crystallographic technique used to determine the structure of solid state materials. Diffraction in solids works by the same principles as the famous double slit experiment, where wave-particles pass through slits with a width on the order of the particle's wavelength. The slits act as a wave point source to constructively and destructively interfere to produce a unique diffraction pattern (Figure 2.2.1). In extended solids, individual atoms act at point scatters for wave particles. The arrangement of atoms in specific planes generate a distinct diffraction peak at a specific angle. Measuring over a range of angles, the overall structure produces a unique diffraction pattern. The angle and occurrence

of a diffraction peak is described by Bragg's law:

$$2d\sin\theta = n\lambda \tag{2.6}$$

where d is the distance between atomic planes, θ is the incident angle of the radiation, n is an integer, and λ is the wavelength.

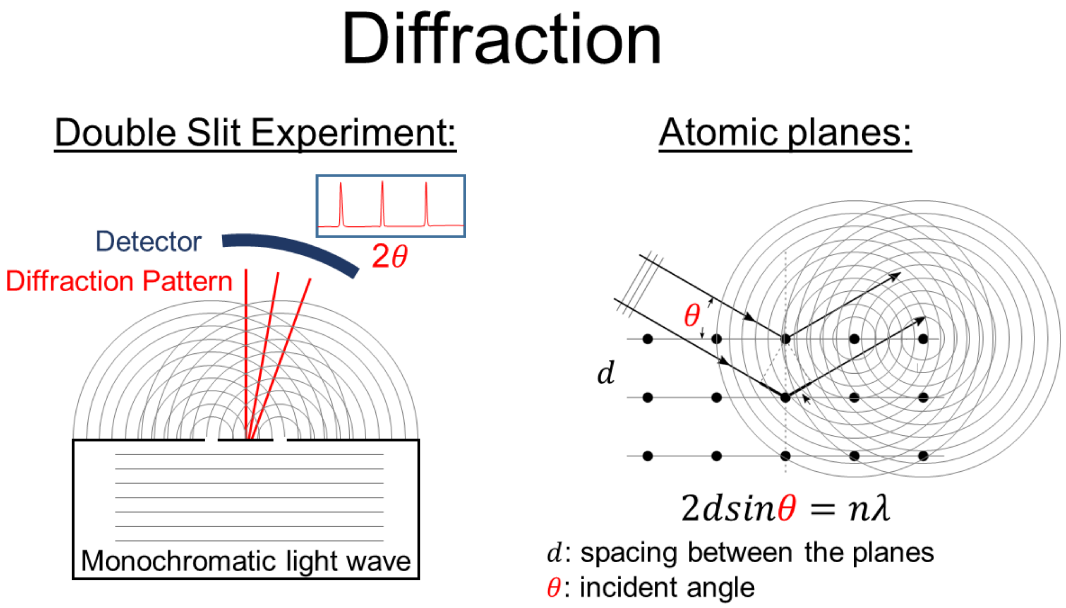

Figure 2.2.1: Schematics of diffraction in the double slit experiment and in a plane of atoms. The slits and atoms behave like point sources which interfere to produce a diffraction pattern. The expected pattern can be calculated for solid state materials with Bragg's Law.

A diffraction pattern can be thought of as having two informational components: reflection position and reflection intensity. For a given the space group and specific dimensions of the unit cell, Bragg's law will determine the position of the allowed peaks in the diffraction pattern. A unit cell (described earlier in section 1.3) is the smallest repeatable unit of a crystalline structure. Reflection intensity is determined by position of the atoms within the unit cell and is sensitive to other factors such as the type incident radiation, instrumental parameters, and temperature.

Table 2.2.1: Wave-particles commonly used in diffraction experiments: photons, electrons, and neutrons

	Photons	Electrons	Neutrons
Mass (kg)	N/A	9.11 x 10^{-31}	1.667 x 10^{-27}
λ (nm)	1.54	1.0	0.2
E (eV)	806	1.5	0.0205
E (Kelvin)	9.35 x 10^{6}	1.75 x 10^{4}	237
p momentum (J s/m)	4.30 x 10^{-43}	6.63 x 10^{-25}	3.31 x 10^{-24}
p momentum (eV s/m)	2.69 x 10^{-24}	4.14 x 10^{-6}	2.07 x 10^{-5}

Peak Intensity and Types of radiation

There are three main wave-particles used in diffraction experiments: X-ray, electron, and neutron (Table 2.2.1). This dissertation uses primarily x-ray and neutron diffraction for sample characterization. Each probe has different advantages and disadvantages, but when used together, the techniques are often complementary. X-rays and electrons scatter off of the electron clouds surrounding the atoms where neutrons scatter off of the nuclei.

Atomic planes are defined by Miller indicies, *hkl*, where *h, k,* and *l* are the inverse of the unit cell coordinates.[18] For example if an atomic plane intersected a unit cell at the coordinates $a = \frac{1}{4}$, $b = \frac{1}{2}$, and $c = \frac{1}{3}$, it would have an *hkl* of (423). The intensity of a *hkl* reflection, I_{hkl}, is proportional to the structure factor F_{hkl} by:

$$I_{hkl} \propto (F_{hkl})^2 \tag{2.7}$$

where the structure factor is defined as:

$$F_{hkl} = \sum_j f_j e^{i\alpha_{hkl}} = \sum_j f_j e^{2\pi i(hx_j + ky_j + lz_j)} \tag{2.8}$$

The structure factor is a model for the amplitude and phase of a reflection with the Miller indices h,k,l where $\sum_j$ is the sum of all the atoms in the unit cell, (x_j, y_j, z_j) are the coordinates of atom j, f_j is the scattering factor of atom j, and α_{hkl} is the phase of the diffracted beam. Recall the intensity is the square of the structure factor so phase

information is lost upon detection.

In X-ray diffraction, the scattering factor, f_j, of an atom is directly proportional to the atomic number, Z, where heavy atoms like U ($Z = 92$) scatter much more strongly than light atoms like Li ($Z = 3$) On the other hand, the scattering factors for neutrons does not trend with respect to atomic number and have values all within an order of magnitude of one another. This gives neutrons a number of advantages and makes it extremely complementary to X-ray diffraction for solving structures.

First, the seemingly random scattering strength of specific atoms in neutron diffraction can lead to different atomic contrast compared to X-ray diffraction which together help to tease out difficult to distinguish elements. Also, since neutrons reflect off of the nuclei, neutron diffraction is extremely sensitive to different isotopes which could have vastly different, such as positive vs. negative, scattering factors. This means you can mix negative scattering isotopes and positive scattering isotopes in a specific ratio to effectively cancel out all contributions from that atom, making other features of the structure more apparent. Another important distinction is the difference in the form factor (Figure 2.2.2). The form factor describes the intensity of the scattered waves as a function of the incident angle. For radiation that interacts with the electron cloud such as X-rays, the intensity is strongest at low angles and decreases as 2θ approaches 180°. This is due to the electron cloud being spread out in real space. For simplicity, if you assume a Gaussian distribution of an electron around an atom in real space, the Fourier transform will result in a Gaussian distribution in k-space resulting in a drop in intensity out further in momentum space (often denoted as Q in neutron experiments). Neutrons interact with nuclei, which are approximately δ-functions in real space compared to electrons clouds. This leads to a nearly flat dependence of amplitude as a function of momentum space. Therefore neutron diffraction is better suited to probe higher angles (larger Q) without losing intensity.

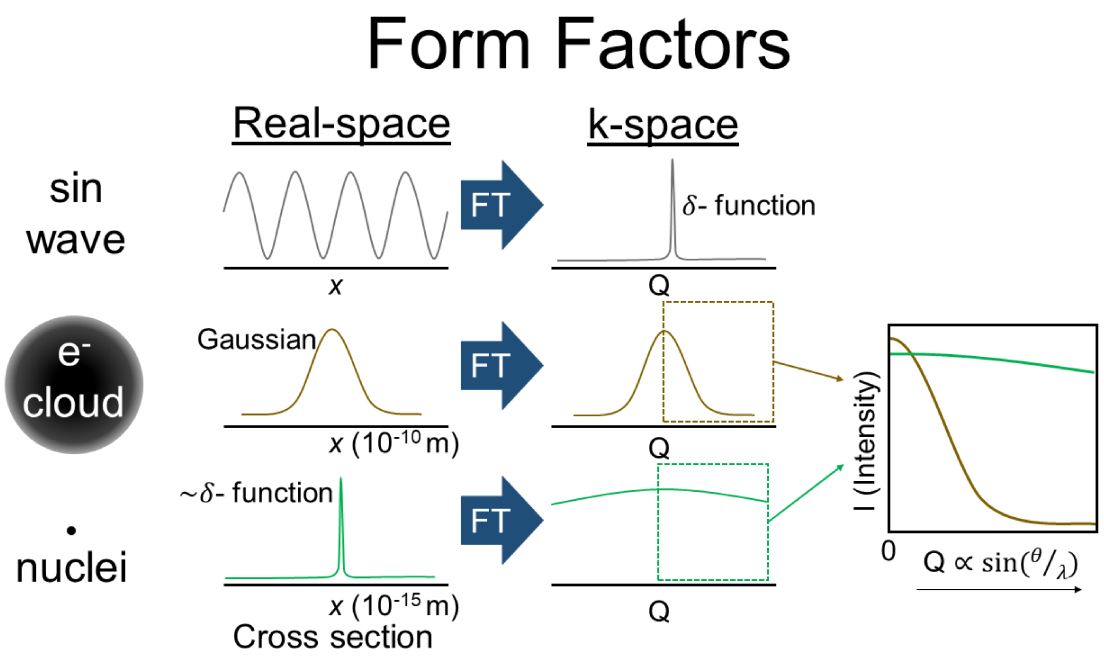

Figure 2.2.2: A schematic of the form factors for electrons vs. nuclei. The first column illustrates the real space cross section of the scattering object. The sin wave serves as a reference for the operation of a Fourier transform (FT). After the transformation, the resulting k-space dependent intensity is displayed in the second column. The third figure compares the form factors for electrons and neutron scatterers as a function of momentum space.[1]

Powder diffraction and Rietveld Refinements

Diffraction can be measured on either single crystal or powder samples. Single crystal diffraction generates a three dimensional pattern which can be collected over many crystal orientations relative to the incident beam. However for many materials, it is extremely difficult to grow single crystals, so measurements are often done on their polycrystalline powder form. When measuring a polycrystalline powder, the particles consist of a vast number of randomly oriented crystallites. These effectively represent all single crystal orientations at the same time, averaging the 3D oriented peaks into a series of cones defined by a specific 2θ angle. The powder experiment detects the Bragg cone reflection to measure a diffraction pattern of peak intensity vs. diffraction angle. Refinement techniques can be used to back out rich structural information.

Rietveld refinement is a powerful method for solving crystal structures from powder neutron (NPD) and X-ray diffraction (PXRD) patterns. It allows for the identification of materials, determination of purity, and refinement of atomic structure. Essentially in a Rietveld analysis, a calculated model is refined using a least squares approach to fit it to the observed data. A model can either be built from scratch using various techniques such as simulated annealing, or can be derived and modified from a known related structure. The model includes instrumental parameters and the phase's structural parameters: space group, lattice parameters, domain sizes, stress/strain, preferred orientation, atomic positions, occupancy, and thermal parameters.

There is no single metric that can use to determine the best fit.[63] One must consider the statistical discrepancy values (such as goodness-of-fit (GOF), χ^2, number of refined parameters, and the R-factors) and the "overall chemical sense" of the structure taking into consideration bond lengths, coordination, and oxidation states. Listed below are some of the most common statistical discrepancy values used throughout the text.

$$R_{wp} = \sqrt{\frac{\sum w_m (Y_{o,m} - Y_{c,m})^2}{\sum w_m Y_{o,m}^2}} \tag{2.9}$$

$$\chi^2 = \frac{\sum w_m (Y_{o,m} - Y_{c-m})^2}{M - P} \tag{2.10}$$

$$GOF^2 = \chi^2 \tag{2.11}$$

where w_m is the weight, $Y_{o,m}$ is the observed intensity values, $Y_{c,m}$ is the calculated intensity value, M is the number of data points, and P is the number of parameters

The ideal value for $\chi^2 = 1$, where the model perfectly matches the observed data but due to noise and error χ^2 should be slightly greater than 1. Values less than one means you are overfitting the observed data while values much greater than 1 suggest that there may be an issue with the proposed structural model.

2.2.2 X-ray Photoelectron Spectroscopy (XPS)

X-ray Photoelectron Spectroscopy (XPS) is a surface technique that is sensitive to the chemical composition and the local chemical and electronic environments of the elements within a sample material. XPS uses soft x-rays (∼1253 eV) excite the atoms in the material and photoeject electrons that reside in the lowest core energy levels. Every element has a unique spectra based on atoms underlying physics which dictates the specific probability and energy of ejecting specific core electrons, making it desirable for identifying composition and relative concentrations. The energy of the photoelectrons is measured by an analyzer to determine the electrons kinetic energy (KE). The bonding energy (BE) can be determined by subtracting the KE from the incident X-ray energy ($h\nu$):

$$BE = h\nu - KE \tag{2.12}$$

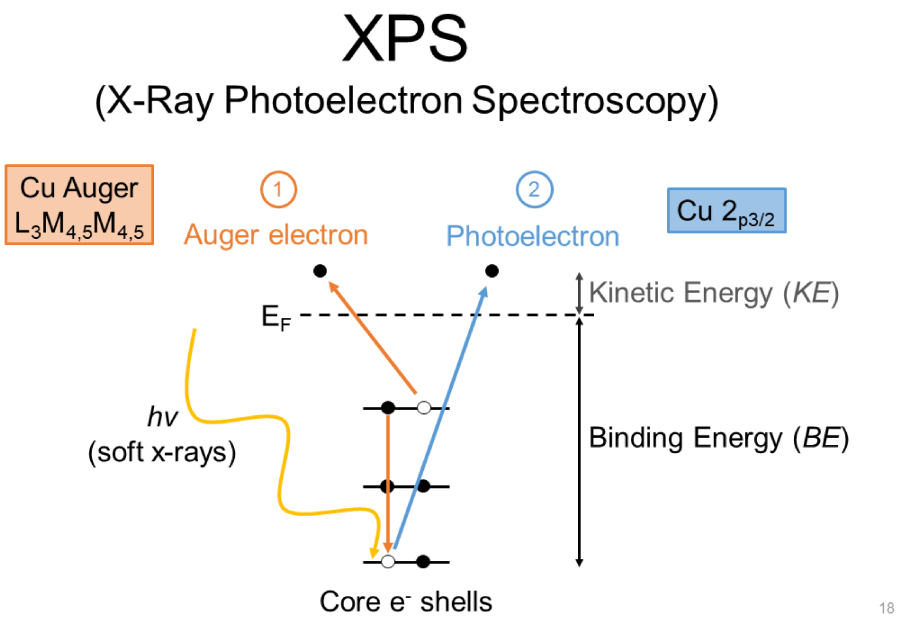

Figure 2.2.3: A schematic of the two possible electron processes in an x-ray photoelectron spectroscopy (XPS) measurement in copper: the generation of an Auger electron (orange) and Photoelectron (blue).

The process can be complicated by the simultaneously occurring Auger process. How-

ever, Auger peaks can be easily identified by adjusting the incident x-ray energy since their total measured energy is independent from the incident x-ray, unlike XPS photoelectrons. XPS can resolve chemical information beyond overall oxidation state and chemical composition. It is also highly responsive to chemical environment. Both the shape and the location of peaks are sensitive to differences in local chemical environment.

2.3 Measurement of physical properties

The aptly named Phyiscal Properties Measurement System (PPMS) is a multifunctional instrument that can be modified to measure many physical properties of materials such as magnetization, heat capacity, resistivity, photoconductivity, magnetoresistance, and others. This dissertation focuses on primarily on magnetization and heat capacity measurements which are further explained below.

2.3.1 Magnetization measurements

Magnetism is a fundamental property which drives many of the applications in materials. However, measuring magnetic response can be difficult. One way to determine magnetic properties is through magnetization measurements on the PPMS. The measurement is possible through induction, the coupling of magnetic field and electrical current in a coil. Using this principle, we can pass the sample through a detection coil while applying a magnetic field to measure a change in current and back out the magnetic response.

Applying magnetic field, $\vec{H}$, to a material induces a internal magnetic field, $\vec{B}$, which can be thought of as a flux density. The response is determined by an intrinsic material property called magnetic permeability, μ, and is related to the $\vec{B}$ by the following equation.

$$\vec{B} = \mu\vec{H} \tag{2.13}$$

The equation can be rewritten to separate out the contribution of magnetic flux through

vacuum, $\mu_0\vec{H}$, from the material by introducing a term called of magnetization, $\vec{M}$. $\vec{M}$ describes the volume density of magnetic dipole moments associated with the electronic structure of the solid. The magnetization is the response that is directly measured by the PPMS in many of the data sets presented throughout this document. By assuming a linear response, which is a good assumption in the case of many paramagnets since their response is isotropic, the magnetic susceptibility, χ, is determined. The magnetic susceptibility is a ratio and is therefore unitless, however it is given the units of emu to follow convention and for bookkeeping.

$$\vec{B} = \mu_0(\vec{H} + \vec{M}) \tag{2.14}$$

$$\mu\vec{H} = \mu_0(\vec{H} + \vec{M}) \tag{2.15}$$

$$(\frac{\mu}{\mu_0} - 1) = \frac{\vec{M}}{\vec{H}} = \chi \tag{2.16}$$

The Curie-Weiss law describes the χ for materials in the paramagnetic state in terms of interactions of magnetic moments. The Curie-Weiss law is:

$$\chi = \frac{C}{T - \theta} + \chi_0 \tag{2.17}$$

where C is the Curie constant, a measure of the effective magnetic moment of the magnetic ions; θ is the Weiss temperature, a measure of the strength and type of magnetic exchange interactions; and χ_0 a temperature-independent contribution to the response. This relationship may be linearized and fit to data:

$$\frac{1}{\chi - \chi_0} = \frac{1}{C}T - \frac{\theta}{C}. \tag{2.18}$$

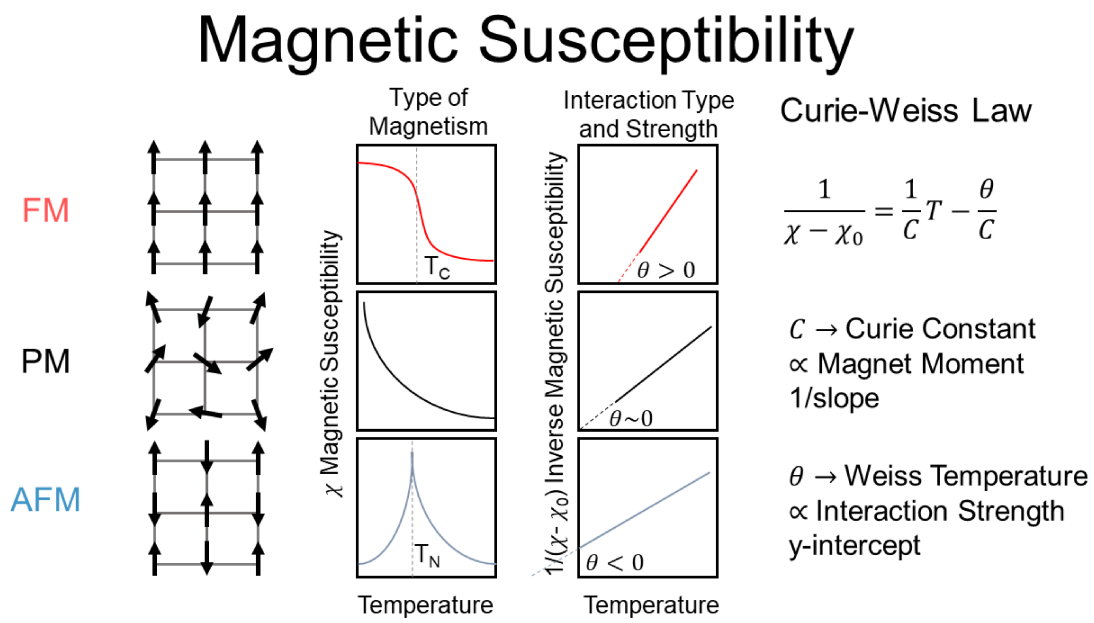

Figure 2.3.1: Curie Weiss analysis on the magnetic susceptibility of 3 types of magenetic behavior: ferromagnetism (FM - red), paramagnetism (PM - black), and antiferromagnetism (AFM - blue).

Performing this analysis in the paramagnetic region allows for the determination of the dominant magnetic interaction through the Weiss temperatue θ and the determination of the effective magnetic moment, μ_{eff}, from the Curie constant which is related to the effective moment by equation 2.19. The strength and sign of the Weiss temperature is direction proportional to the exchange interaction, J, as discussed in section 1.5.3. So it follows that $\theta < 0$ has net antiferromagnetic interaction, $\theta \approx 0$ indicates paramagnetism with weak interactions, and $\theta > 0$ host ferromagnetic interactions.

$$p_{eff} \approx \sqrt{8C} \tag{2.19}$$

Understanding these magnetic interactions is especially important for understanding frustrated magnetism. The hallmark of a highly frustrated system is one that exhibits strong antiferromagnetic interactions (large and negative θ) while suppressing magnetic order at all observable temperatures. This is the case for Herbertsmithite which has a Weiss tem-

perature of $\theta \approx$ -200 K without magnetic ordering down to $T <$ 0.05 K.

2.3.2 Heat capacity

Heat capacity is one of the most informative measurements that can be performed on a material. The specific heat is defined as the amount of heat, δQ, required to raise the temperature of a material, $C \equiv \delta Q/dT$.[**?**] The power of this measurement resides in thermodynamic relationship between specific heat entropy where:

$$S = \int_{0\,\mathrm{K}}^{T} \frac{C_v}{T} dT. \tag{2.20}$$

This allows heat capacity measures to capture all of the entropy associated with the materials which include magnetic, electronic, lattice (phononic), and structural contributions. Heat capacity can be defined under two conditions: constant volume, C_v, or constant pressure, C_p. Unlike gases, it is extremely difficult to measure solids under isochoric conditions, so measurements are carried out at constant pressure. However, the thermodynamic relationship between entropy and C_p is not as convenient as the straight forward relationship with C_v. C_p and C_v are related by:

$$C_p - C_v = \frac{V\beta^2}{\kappa_T} T = \frac{\left(\frac{\partial V}{\partial T}\right)_P}{\left(\frac{-\partial V}{\partial P}\right)_T} T \tag{2.21}$$

where β is the volume expansion coefficient and κ_T is the isothermal compressibility [**?**]. The isothermal compressibility is a positive quantity so C_p will always be greater than C_v. However, as the temperature approach zero, the difference between the heat capacities go to zero. It is estimated for materials below $\sim$30 K there is a negligible difference between C_p and C_v. In a typical material, the $\frac{C_p - Cv}{C_p} \leq 0.1\%$ for temperatures up to $\theta_D/6$, 1% for temperatures up to $\theta_D/3$, and 10% at the melting point [**?**]. Therefore at low temperatures, it is safe to assume that $C_p \approx C_v$ and $S \approx \int \frac{C_p}{T} dT$.

At low temperatures, the heat capacity can be approximated by the following model:

$$C_v = \gamma T + \beta_3 T^3 + \beta_5 T^5 + \beta_7 T^7 + ...$$
$$C_v \approx \gamma T + \beta_3 T^3 + \beta_5 T^5 \tag{2.22}$$

where γT describes the linear contribution and $\beta_3 T^3 + \beta_5 T^5 + ...$ describes the phononic contribution of the lattice [**?**]. In many models, γT is the Sommerfeld coefficient which describes the electronic contribution from the free conduction electrons. However, there are other phenomena which can also contribute a T-linear dependence in the heat capacity such as certain models for spin liquid behavior.

There are several different ways to plot Heat Capacity to extract different values and highlight specific components. Plotting $C/T vs. T$ is advantageous to highlight entropy as entropy is the area under the curve. Plotting $C/T vs. T^2$ allows you to linearize $C/T = \gamma + \beta_3 T^2$ so that β_3 is the slope and γ is the y-intercept. $(C-\gamma)/T^3 vs. T$ highlights the phononic contributions and any Schottky anomalies as $(C-\gamma)/T^3 = \beta_3 + C_{Sch}/T^3$.

Schottky Anomaly

The heat capacity of a discrete two level system gives rise to a broad peak known as a Schottky anomaly. Two level systems are prevalent in the low temperature specific heat of materials which could result from crystal field splitting, optical phonon modes, and field induced spin anisotropy (Zeeman splitting).

The heat capacity for a Schottky anomaly is expressed as:

$$C_{Sch} = R\left(\frac{\Delta}{T}\right)^2 \frac{e^{\Delta/T}}{(1+e^{\Delta/T})^2} \tag{2.23}$$

where R is the gas constant and $k_B\Delta$ is the energy of the gap between the two states. The peak of the anomaly occurs at the intermediate temperature, T_m, and is directly proportional to the splitting between the energy levels where $T_M \approx 0.42\Delta$. In the following chapters,

Schottky anomalies are used to model low temperature heat capacity behavior.

Heat capacity Long Pulse method

The PPMS heat capacity insert is shown in Figure 2.3.2 **a**. It is comprised of a sample platform, suspended in air by a thin set of wires to help with thermal isolation. Underneath the platform, there is a thermometer and a heater used to control the heat applied to the sample. In order for the measurements to be accurate, the sample must be in excellent thermal contact with the platform to reach thermal equilibrium. The heat flow can be understood as a heat circuit which is shown in the lower half of Figure 2.3.2 **a**. Typical heat capacity measurements use the semi-adiabatic pulse technique analyzed by the dual slope method. This approach heats the sample to produce a temperature rise of $\sim$2% at temperatures ranging from T = 2-300 K. The heating and cooling curves are fit to 2τ heat flow model to extract a C_p for the material at that temperature. This technique is very accurate when the heat capacity is continuous. However issues arise when a material undergoes a large 1st order phase transition with significant latent heat. The latent heat distorts the heating and cooling curves, as shown in Figure 2.3.2 **b**, preventing them from being described by the 2τ heat flow model (left panel).

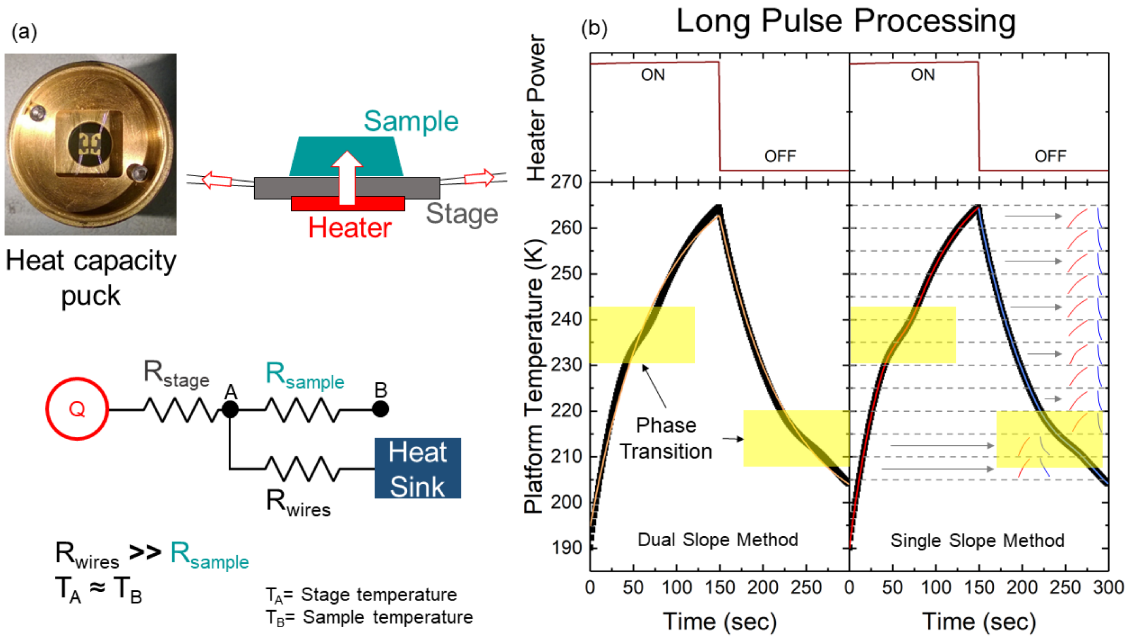

Figure 2.3.2: a) A picture and illustration of a Quantum Design Heat capacity puck with a schematic for its *heat circuit*. Power pulse is applied to the heater which flows heat into the sample stage. Since the thermal resistance of the wires (R_{wires}) is much greater than the sample (R_{sample}), the heat flows into the the sample, reaching equilibrium with the stage. After the pulse, the heat is removed through the wires into the heat sink of the system. **b)** Data from a long pulse heating and cooling sequence of $Na_2Ti_3Cl_8$. The top panels are the power pulse applied to the heater vs. time. The left panel is fit with a single 2τ heat flow model using the dual slope method (orange). The right panel is a representation of how the long pulse data is analyzed using by fitting sections (dashed gray lines are the sections) of the corresponding heating (red) and cooling (blue) curves to extract more accurate heat capacity values around a phase transition.

The long pulse method can be used to get an accurate measure of the heat capacity of a first order phase transition. In the long pulse method, a large power pulse is applied to the sample to raise the temperature 10-100% capturing the entire transition in one pulse (Figure 2.3.2 **b**). Fitting with the 2τ heat flow model using the dual slope method over the whole range does not accurately capture the changes in HC around the phase transition. Treating and fitting the heating curve separately from the cooling curve and by slicing the data into temperature sections (right panel), the data can be analyzed by single slope method to calculate the heat capacity of the transition on warming and on cooling. An

example of this shown in Figure 2.3.3, where $Na_2Ti_3Cl_8$ goes through one phase transition on warming and two phase transitions on cooling. The heat capacity can then be integrated to give the entropy of the transition. This is discussed in further detail in chapter 4.

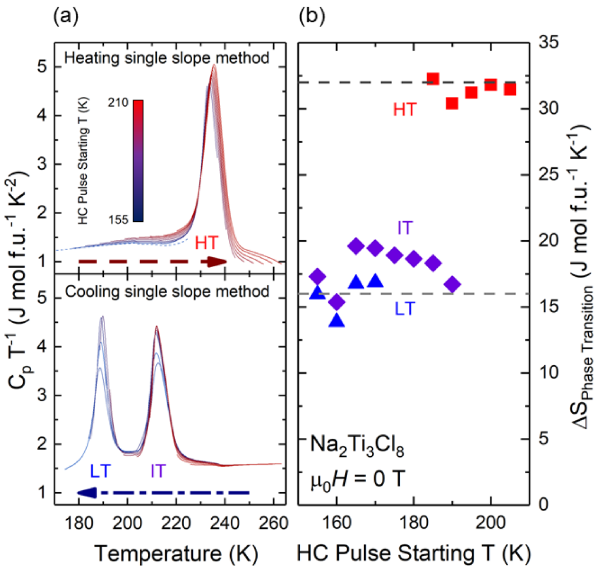

Figure 2.3.3: An example of long pulse heat capacity analysis on $Na_2Ti_3Cl_8$ **a** The individual LongHCPulse fits for both the heating (top) and cooling (bottom) curves at different starting pulse temperatures. **b** The change in entropy for each phase transition extracted by integration of the long pulse heat capacity measurements. The dashed lines (dark gray = 32 J mol f.u.$^{-1}$ K^{-1} and light gray = 16 J mol f.u.$^{-1}$ K^{-1}) are guides to the eye to illustrate that entropy associated with the HT $\rightarrow$ IT and IT $\rightarrow$ LT cooling transitions are approximately half the LT $\rightarrow$ HT heating transition. Scans on the edges of the range were partially patched with neighboring scans to complete the shape of the peak into the base line to ensure that background subtraction and integration was consistent across all scans. The patched sections were slight translated in temperatures to maintain a continuous curve.

3 Electron Doping a Kagomé Spin Liquid

The following chapter discusses the structure and properties of Li doped Herbertsmithite. This work was co-written with the following authors and is published under the following citation:

Physical Review X **6**, 4 (2016)

http://dx.doi.org/10.1103/PhysRevX.6.041007

Z. A. Kelly[1,2], M. J. Gallagher[1], T. M. McQueen[1,2,*]

[1]Department of Chemistry, The Johns Hopkins University, Baltimore, MD 21218, USA

[2]Institute for Quantum Matter, Department of Physics and Astronomy,

The Johns Hopkins University, Baltimore, MD 21218, USA

[3]Department of Materials Science and Engineering, The Johns Hopkins University, Baltimore, MD 21218, USA

[*]Corresponding Author

3.1 Abstract

Herbertsmithite, $ZnCu_3(OH)_6Cl_2$, is a two dimensional kagomé lattice realization of a spin liquid, with evidence for fractionalized excitations and a gapped ground state. Such a quantum spin liquid has been proposed to underlie high temperature superconductivity and is predicted to produce a wealth of new states, including a Dirac metal at $1/3$rd electron doping. Here we report the topochemical synthesis of electron-doped $ZnLi_xCu_3(OH)_6Cl_2$ from $x = 0$ to $x = 1.8$ ($3/5$th per Cu^{2+}). Contrary to expectations, no metallicity or superconductivity is induced. Instead, we find a systematic suppression of magnetic behavior across the phase diagram. Our results demonstrate that significant theoretical work is needed to understand and predict the role of doping in magnetically frustrated narrow band insulators, particularly the interplay between local structural disorder and tendency toward electron localization, and pave the way for future studies of doped spin liquids.

3.2 Introduction

For decades, the resonance valence bond (RVB), or quantum spin-liquid, state has been theorized to be an intricate part of the mechanism for high temperature superconductivity[17, 43]. One geometrically frustrated system, Herbertsmithite (Fig.3.3.1(a)), is considered an ideal spin two dimensional liquid candidate due to its perfectly ordered kagomé lattice of $S = 1/2$ copper ions, antiferromagnetic interactions with $J \approx -200$ K, strong evidence for fractional spin excitations by neutron scattering, and, most recently, convincing indications of a gapped spin-liquid ground state by oxygen-17 NMR[36, 44, 45, 66**?** , 67]. All of these factors suggest Herbertsmithite is the realization of a quantum spin liquid. Recent predictions expanded upon Anderson's theory in DFT calculations of electron doped Herbertsmithite, $M_xZn_{1-x}Cu_3(OH)_6Cl_2$, where Ga^{3+} or other aliovalent metals replace zinc[68, 69]. A trivalent substitution introduces electrons into the material, raising the Fermi level to the Dirac points at $x = 1$, and giving rise to a rich phase diagram span-

ning from a frustrated RVB spin liquid ($x = 0$) to a strongly correlated Dirac metal ($x = 1$) with possible Mott-Hubbard metal-insulator transitions, charge ordering, ferromagnetism, or superconducting states.

It is challenging to synthesize electron doped Herbertsmithite directly as Cu^{1+} will not assume the same distorted octahedral site on the kagomé lattice as Cu^{2+} under thermodynamic conditions, and copper(I) hydroxide is thermodynamically unstable towards disproportionation and evolution of hydrogen gas. By using low temperature topochemical techniques, this problem is circumvented by producing a kinetically meta-stable phase[70–73]. Here we use intercalation of lithium to produce electron doped Herbertsmithite, $ZnLi_xCu_3(OH)_6Cl_2$ with $0 \leq x \leq 1.8$.

3.3 Results and Discussion

3.3.1 Powder X-ray and Neutron Diffraction

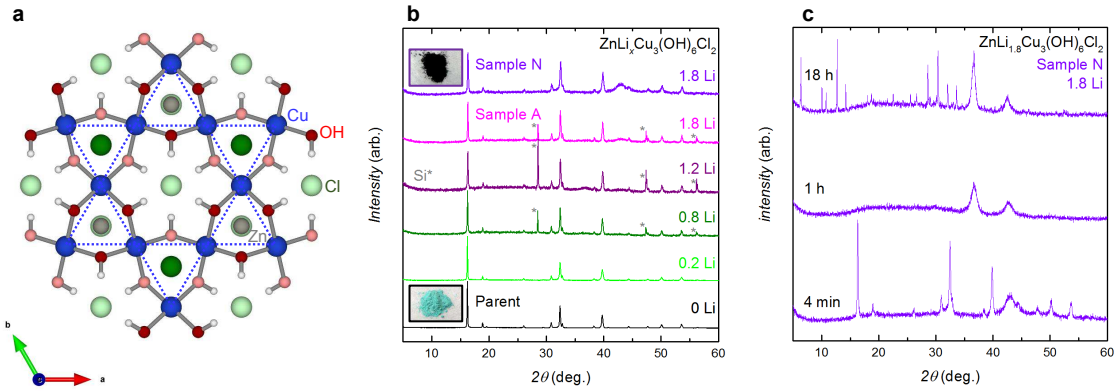

Figure 3.3.1: Doped Herbertsmithite structure. **a)** a top-down (along c-axis) representation of the parent Herbertsmithite copper kagomé layer (blue dotted line) with Cu (blue) and O (red), H (white), Zn (gray) and Cl (green) between the kagomé layers. The dark and light atoms are located above and below the kagomé plane respectively. **b)** The X-ray powder diffraction (XRPD) patterns of the complete series. The gray asterisks represent the presence of Si (internal standard). An image of the blue-green parent material is shown in the lower left corner while a picture of the black doped sample N is shown in the upper left. All doped samples are also black. **c)** XRPD data demonstrates the instability of one of the maximally doped samples, sample N, in air ($x = 1.8$) as it decomposes in hours into several other phases.

Laboratory X-ray powder diffraction (XRPD), Fig.3.3.1(b), shows the underlying structure is maintained throughout the doped series. Lithium is not directly detected due to its small X-ray scattering intensity relative to copper and zinc. Any changes in the lattice parameters as a function of doping are small and are within the resolution of the Laboratory X-ray diffractometer (Table 3.3.1). During Rietveld analysis, CuO and Cu_2O were tested and are absent from the air-free samples by both XRPD and neutron diffraction. Unlike

the air stable parent, the doped samples decomposed readily in air, Fig.3.3.1(c), with the most heavily doped samples completely decomposing within hours. This rapid and total decomposition is in agreement with the formation of a reduced copper (Cu^{1+}) hydroxide in the bulk that is prone to decomposition in moisture. The color change from blue to black is also in agreement. As soon as there are any Cu^{1+} ions present, there is another possible optical absorption mode: intervalence charge transfer (i.e. $Cu^{2+} + Cu^{1+} \rightarrow Cu^{1+} + Cu^{2+}$), or, put another way, a transition from an impurity band in the gap to the conduction band. Such absorption modes are common in mixed valent systems, such as the Cu^{1+} - Cu^{2+} mixed valence $(N_2H_5)_2Cu_3Cl_6$[74].

Table 3.3.1: Bond angles, bond lengths, and crystallographic parameters for the series, $ZnCu_3Li_x(OH)_6Cl_2$, obtained from Rietveld refinement of Laboratory X-ray powder diffraction patterns at room temperature. The trigonal space group, $R\bar{3}m$ (166), was used for all refinements. Li cannot be directly detected by Laboratory XRPD due to its small scattering factor relative to Zn, Cu, O, and Cl, therefore it was not included in refinements to simplify the analysis. Atomic displacement parameters (U_{iso}) for Zn, Cu1, O, Cl, and Cu2 were constrained with each other and occupancies of Zn, Cu, O, Cl, and H were fixed at nominal values. The position and atomic displacement parameters for H were held constant across all samples. Errors reported are statistical uncertainties.

Atoms	Parameters	Parent	0.2 Li	0.8 Li	1.2 Li	1.8 Li
	O-Cu-Cl (°)	83.03(12)	83.94(15)	84.36(19)	85.1(3)	86.69(17)
	O-Cu (*Å*)	2.003(4)	2.018(6)	2.025(10)	2.034(13)	2.075(9)
	Cl-Cu (*Å*)	2.764(3)	2.777(5)	2.793(9)	2.826(13)	2.817(8)
	O-O (*Å*)	2.663(3)	2.684(5)	2.748(9)	2.806(11)	2.898(8)
	$a = b$ (*Å*)	6.8414(2)	6.8416(4)	6.8450(3)	6.8460(3)	6.8447(3)
	c (*Å*)	14.1035(4)	14.0942(9)	14.096(2)	14.095(2)	14.099(1)
	R_{wp}	5.798	8.547	7.07	7.824	6.553
	U_{iso}	0.040(1)	0.031(2)	0.023(3)	0.008(4)	0.007(3)
Zn	*x,y,z*	$0,0,\frac{1}{2}$	→		→	
	occ.	0.85	→		→	
Cu1	*x,y,z*	$\frac{1}{2},0,0$	→		→	
O	*x*	0.20359(46)	0.20258(79)	0.1995(14)	0.1967(17)	0.1922(13)
	y	-0.20359(46)	-0.20258(79)	-0.1995(14)	-0.1967(17)	-0.1922(13)
	z	0.06275(35)	0.06465(63)	0.0640(10)	0.0638(15)	0.06762(85)
Cl	*x, y*	0,0	→		→	
	z	0.19626(29)	0.19479(50)	0.19331(85)	0.1900(12)	0.19093(76)
H	*x, y, z*	0.138, -0.138, 0.0862	→		→	
	U_{iso}	0.0507	→		→	
Cu2	*x,y,z*	$0,0,\frac{1}{2}$	→		→	
	occ.	0.15	→		→	

$$R_{wp} = \sqrt{\frac{\sum w_m (Y_{o,m} - Y_{c,m})^2}{\sum w_m Y_{o,m}^2}}$$

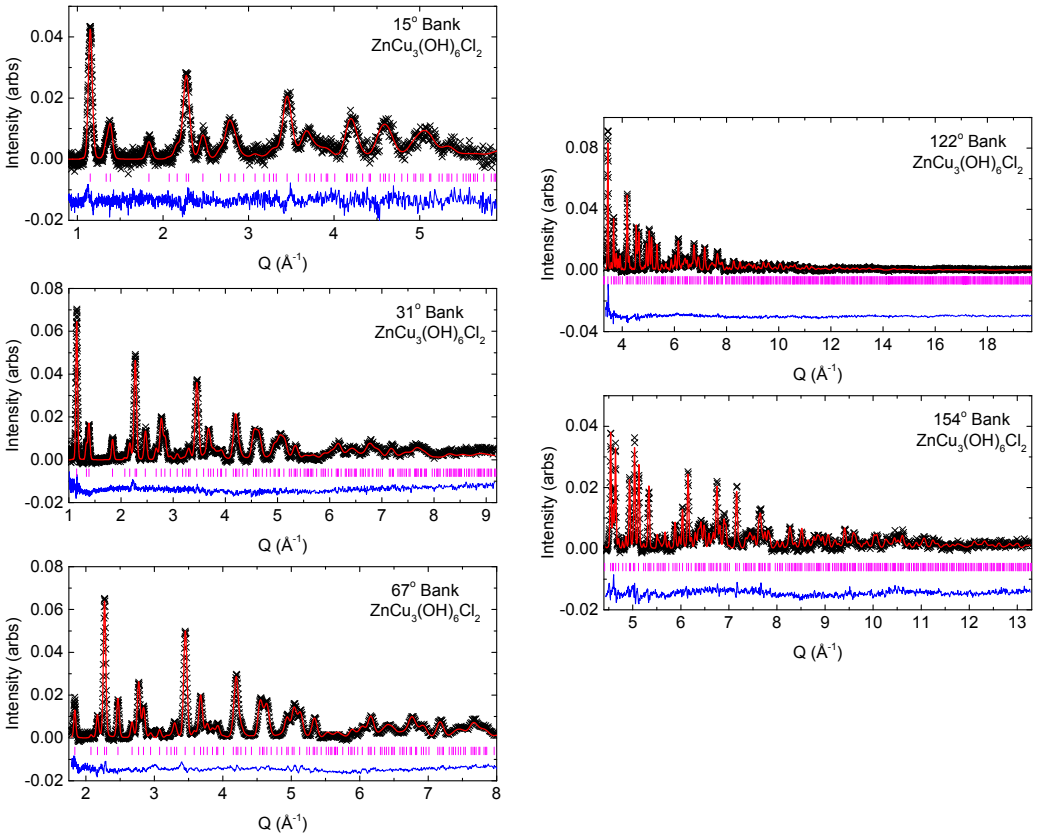

Figure 3.3.2: Rietveld refinement of time-of-flight neutron diffraction of the parent, $ZnCu_3(OH)_6Cl_2$ at $T = 300$ K on the NOMAD instrument. The Data (black Xs) and Rietveld analysis (red line) are in good agreement with the expected $R\bar{3}m$ (166) symmetry (magenta tick marks) having only minimal deviations in the difference (blue line).

Table 3.3.2: Crystallographic parameters for the parent, $ZnCu_3(OH)_6Cl_2$, using tetrahedral $R\bar{3}m$ (166) obtained from Rietveld refinement of NOMAD neutron diffraction data banks 1-5 at room temperature. Atomic displacement parameters (U_{iso}) for Zn1 to Cu2 were constrained with each other and occupancies of Zn, Cu, O, Cl, and H were fixed at nominal values. Errors reported are statistical uncertainties.

	TOF			R_{wp}	0.0201	
	$a = b$ (Å)	6.84271(11)		R_p	0.0176	
	c (Å)	14.1072(4)				
	$\alpha = \beta, \gamma$ (°)	90, 120		χ^2	2.975	
	V (Å^3)	572.043(21)				
Atom	Wyck. Pos.	x	y	z	U_{iso} (Å^2)	occ.
Zn1	3b	0.000000	0.000000	0.500000	0.0019(3)	0.8500
Cu1	9e	0.500000	0.000000	0.000000	0.0123(2)	1.0000
O1	18h	0.20498(9)	-0.20498(9)	0.0627(1)	0.01244(18)	1.0000
Cl1	6c	0.000000	0.000000	0.1950(1)	0.020(3)	1.0000
H1	18h	0.13139(17)	-0.13139(17)	0.0886(2)	0.0337(5)	1.0000
Cu2	3b	0.000000	0.000000	0.500000	0.0019(3)	0.1500

$$\chi^2 = \sqrt{\frac{\sum w_m (Y_{o,m} - Y_{c-m})^2}{M-P}}$$
$$R_p = \sqrt{\frac{\sum |Y_{o,m} - Y_{c,m}|}{\sum Y_{o,m}}}$$
$$R_{wp} = \sqrt{\frac{\sum w_m (Y_{o,m} - Y_{c,m})^2}{\sum w_m Y_{o,m}^2}}$$

Table 3.3.3: Crystallographic parameters for sample N, $ZnLi_{1.8}Cu_3(OH)_6Cl_2$, using tetrahedral $R\bar{3}m$ (166) obtained from Rietveld refinement of NOMAD neutron diffraction data banks 1-5 at room temperature. Atomic displacement parameters (U_{iso}) for Zn1 to Cu2 and Cu1 to Li1 were constrained with each other and occupancies of Zn, Cu, O, Cl, and H were fixed at nominal values. Errors reported are from statistical uncertainties

	TOF			R_{wp}	0.0199	
	$a = b$ (Å)	6.8399(4)		R_p	0.0177	
	c (Å)	14.1007(15)				
	$\alpha = \beta, \gamma$ (°)	90, 120		χ^2	1.884	
	V (Å^3)	571.31(8)				
Atom	Wyck. Pos.	x	y	z	U_{iso} (Å^2)	occ.
Zn1	3b	0.000000	0.000000	0.500000	0.0159(13)	0.8500
Cu1	9e	0.500000	0.000000	0.000000	0.0102(5)	1.0000
O1	18h	0.20376(24)	-0.20376(24)	0.06335(28)	0.0091(4)	1.0000
Cl1	6c	0.000000	0.000000	0.19434(29)	0.0337(9)	1.0000
H1	18h	0.1365(5)	-0.1365(5)	0.0873(7)	0.0889(20)	1.0000
Cu2	3b	0.000000	0.000000	0.500000	0.0159(13)	0.1500
Li1	6c	0.000000	0.000000	0.707280	0.0102(5)	0.85(5)

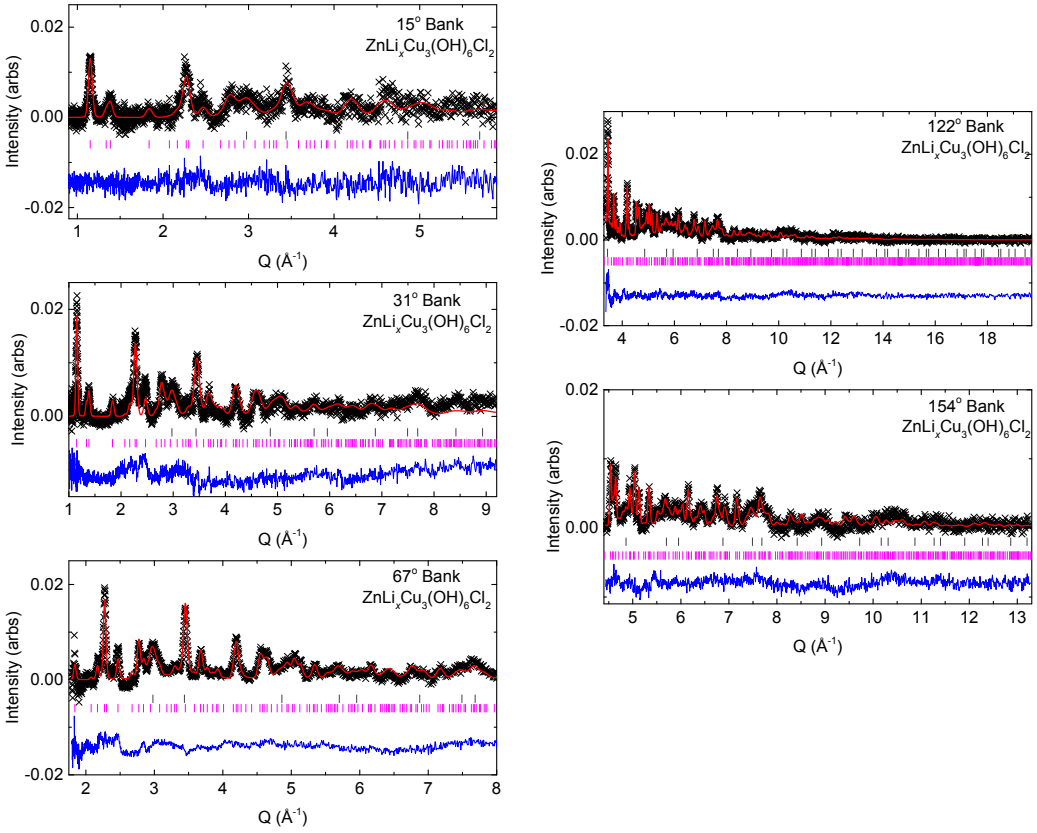

Figure 3.3.3: Rietveld refinement of time-of-flight neutron diffraction of the sample N, $ZnLi_{1.8}Cu_3(OH)_6Cl_2$ at 300 K on the NOMAD instrument. The data (black X's) and Rietveld analysis (red line) are in good agreement with the expected R$\bar{3}$m (166) symmetry (magenta tick marks) having only minimal deviations in the difference (blue line). The fit also includes a secondary Cu metal phase (dark gray tick marks).

Table 3.3.4: We attempted several combinations of sites for Li occupancy. Different combinations of refining both position and occupancy were exhausted for all possible positions as shown below. The site that most dramatically improved the fit was with Li in the Cu-Cl tetrahedral hole. Attempts to allow the Cl occupancy refine with the Li yielded unphysical high Cl and Li fractions, so Cl was fixed to full occupancy allowing the Li occupancy to converge at a value of ≈0.9 ($x = 1.8$ in $ZnLi_xCu_3(OH)_6Cl_2$, which is consistent with the physical properties and synthesis method.

x	y	z	Description:	Improved Fit?
0.000000	0.000000	0.700000	Cl-$(OH)_3$ tetrahedral hole	Yes
0.000000	0.000000	0.193893	On Cl site	No
0.000000	0.000000	0.000000	On Cu site	No
0.000000	0.000000	0.080000	Off set in O octahedral hole	No
0.000000	0.000000	0.380000	Zn-Cu_3 tetrahedral hole	No
0.100000	0.100000	0.000000	Off set in O octahedral hole (1/6 occ.)	No
0.000000	0.000000	0.500000	On Zn site	No
0.203000	-0.203000	0.063350	On O site	No
0.136500	-0.136500	0.087300	Li on H site, H in Cl-OH tetrahedral hole	No

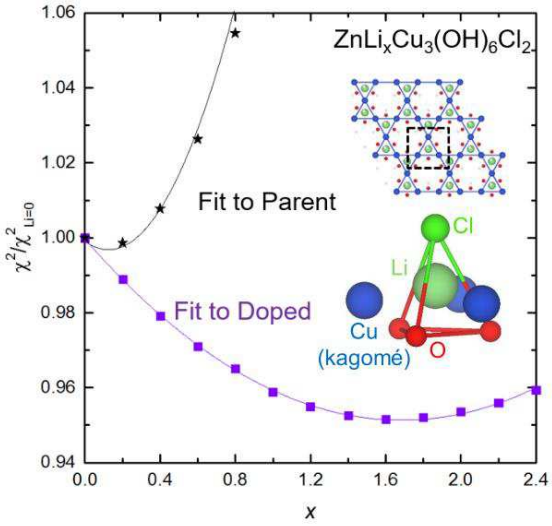

Figure 3.3.4: NOMAD Li fitting in the parent and doped data sets. Once the models were maximally refined for both the parent and the Li doped samples, different Li occupancies in the Cl-$(OH)_3$ tetrahedral hole were systematically tested. The Li doped pattern had the most improved fit at $x = 1.8$ while the parent pattern fit gets increasingly worse as Li occupancy is increased.

To determine the position of Li within the structure, we carried out neutron powder diffraction of the undoped and maximally Li-doped specimens using the high flux NOMAD diffractometer at the Spallation Neutron Source, Oak Ridge National Laboratory (Figure 3.3.2, Table 3.3.2, Figure 3.3.3, and Table 3.3.3). Rietveld analysis reveals that the previously reported structure accurately models the data of the doped specimens, with the exception of the presence of a pocket of negative scattering in a tetrahedral hole formed by three (OH^-) and one Cl^- group, located above and below the copper triangles in the kagomé layer. This is consistent with the presence of Li, which has a negative scattering factor. Although the site is physically small for a Li ion, the connectivity is consistent with a favorable tetrahedral bonding environment for Li. The XRPD studies are also consistent with this model. There are systematic changes in the O-Cu-Cl bond angle and the O-Cu, Cl-Cu, and O-O bond lengths (see Table 3.3.1). As the doping increased, the oxygen atoms move away from the Cu kagomé lattice and spread from one another. In concert, the Cl atom moves away from the kagomé lattice along the c-axis. These combined movements create more space in the Cl-$(OH)_3$ tetrahedral hole. Further, a similar geometry is found in $CuMg_2Li_{0.31}$[75], and a stable Rietveld refinement is obtained for the maximally doped sample N, when including Li in that site, with the occupancy refining to $\sim$0.9 ($x = 1.8(3)$ per formula unit, Figure 3.3.4). This structure puts the Li ion in close proximity to the Cl atom and appears to form a neutral LiCl dimer along the c-axis with a bond distance of $\sim$1.4 Å. Such a dimer is consistent with our attempts to intercalate the larger K^+ ion, which resulted instead in the formation of KCl. Future work is needed to determine if this model is an accurate description of the local atomic structure.

3.3.2 ^{7}Li NMR

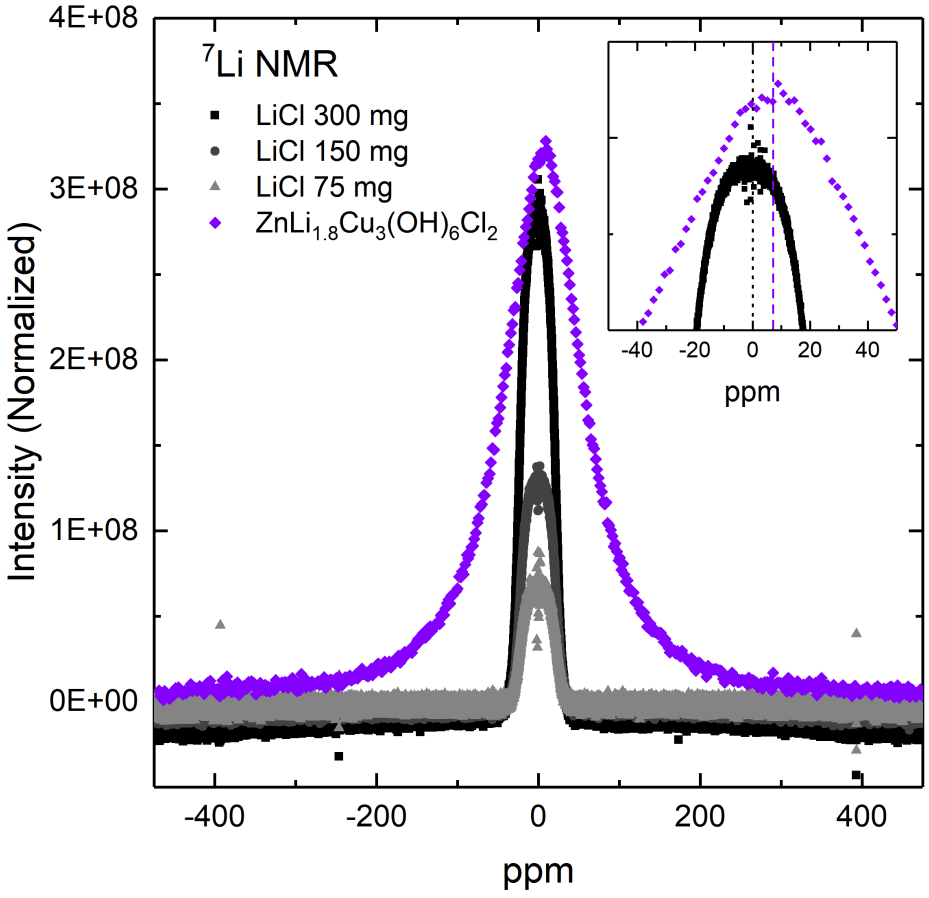

Figure 3.3.5: ^{7}Li NMR of solid LiCl and solid Li doped Herbertsmithite in a Bruker 400 MHz NMR.

To determine if there is Li was present in the Herbertsmithite, ^{7}Li nuclear magnetic resonance (NMR) was attempted on the sample using a 400 MHz NMR. The NMR was calibrated using different amounts of solid LiCl. Although run under normal conditions (not solid state magic angle NMR), a change in Li environment was detected for $ZnLi_xCu_3(OH)_6Cl_2$ compared to LiCl. The major features are a peak shift of 8 ppm and a broadening approximately ranging from -250 to 250 ppm. Paramagnetic materials, such as Herbertsmithite, have unpaired electrons with can strongly interact with nuclei and cause shifts and broadening.

3.3.3 X-ray Photoelectron Spectroscopy

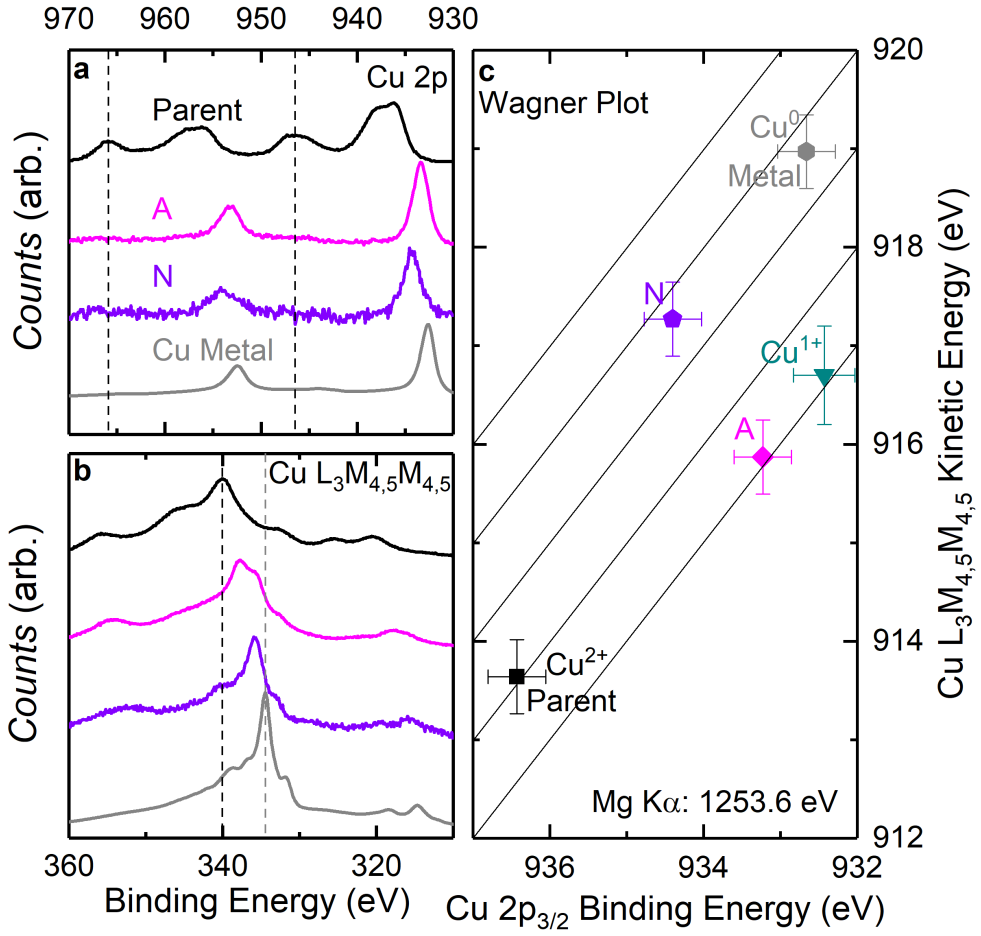

Figure 3.3.6: X-ray Photoelectron Spectroscopy (XPS). **a)** Cu 2p XP spectra of parent Herbertsmithite (black), Sample A (magenta), Sample N (violet), and Cu metal (gray). The black dashed line indicates locations of satellite peaks in the parent, characteristic of Cu^{2+}, which are significantly reduced in the doped samples. **b)** The X-ray generated Auger Cu $L_3M_{4,5}M_{4,5}$ spectra of the same four samples. The black and the gray dotted lines represent the location of the greatest intensity peak for the parent and the copper metal respectively. The peak shape and binding energy of the doped samples varies significantly from both the parent and the copper metal. **c)** A Wagner plot shows the relative chemical shift of the four samples and Cu^{1+} in $Cu(I)_2O$ (lit. teal) by plotting the kinetic energy from the Cu $L_3M_{4,5}M_{4,5}$ peak on the y-axis and the binding energy from the Cu $2p_{3/2}$ peak on the x-axis. The chemical shift is sensitive to the polarizability of the chemical environment

X-Ray Photoelectron Spectroscopy (XPS) provides a direct probe of the chemical environment of copper and was carried out on the parent and two maximally doped specimens,

A and N. The results are consistent with the reduction of Cu^{2+} to Cu^{1+}. Firstly, the four peaks in the parent Cu 2p envelope, Fig.3.3.6(a), are indicative of the two final states in divalent copper, (i) the $3d^{10}L^{-1}$ due to an exiting photoelectron leaving a core hole causing a charge transfer process between the surrounding ligands and Cu d shell and (ii) the $3d^{9}L$ satellite. In the doped samples, this satellite is greatly reduced due to the filled 3d shell in Cu^{1+} preventing this loss transition from occurring[76, 77]. If it were purely Robin-Day Class 1 mixed valence (pure Cu^{1+} and Cu^{2+} sites with no interactions of ground or excited states), we would expect a mixed XPS Signal of Cu^{1+} and Cu^{2+} with an approximate 2:1 ratio. In this case, however, there must be interactions between neighboring Cu^{1+} and Cu^{2+}, given the shared hydroxyl bridge, through which we know (from the parent) that adjacent Cu ions interact[78–80]. The result is a suppression of the Cu^{2+} XPS satellites, even though resistance measurements show the charges must be localized. This model (which has discrete Cu^{1+} and Cu^{2+} ions, Robin-Day Class 2), would not only suppress the Cu^{2+} satellites but also give rise to an optical intervalence charge transfer, which would explain the black color of the material upon even light doping.

Secondly, the photoelectron induced Auger Cu $L_3M_{4,5}M_{4,5}$ spectra, Fig.3.3.6(b), of the maximally doped specimens are in between and distinct from the $L_3M_{4,5}M_{4,5}$ spectra of the Cu foil and the parent Herbertsmithite. Further, a Wagner plot analysis, Fig.3.3.6(c), shows that the Li doped samples are in a distinctly different chemical environment than either the parent (fully Cu^{2+}) or Cu metal (fully Cu^{0})[81], consistent with the structure suggested by our neutron diffraction studies and indicative of the presence of Cu^{1+}[76, 77]. Although information on copper oxidation states is lost in a depth profile analysis with ion sputtering, it can be used to determine the chemical composition[82]. As expected from the topochemical synthesis method, a thin surface layer of Li and benzophenone starting material is detected; upon ion sputtering (up to 100 min), the ratio of Cu:Zn:Cl is in agreement with the expected parent Herbertsmithite phase, with Li located throughout (Figure 3.3.7).

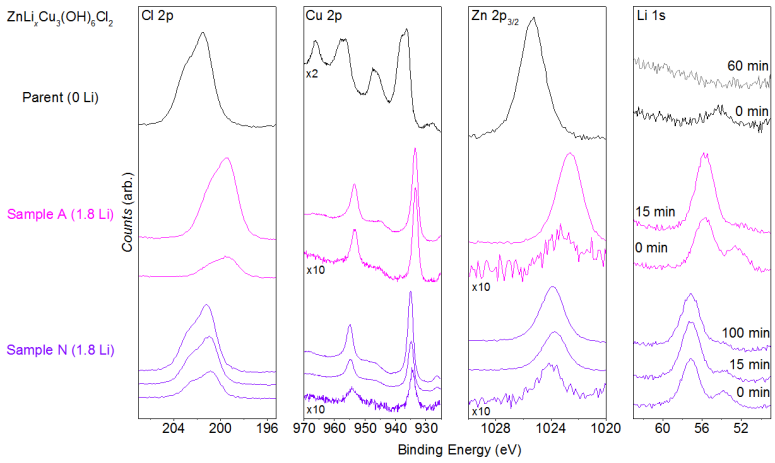

Figure 3.3.7: XPS multiplex spectra with various Ar^+ sputtering times for Cl, Cu, Zn, and Li. Ion sputtering experiments were completed on the Parent, Sample A, and Sample N. It can be seen that the Cu, Zn and Cl signals all coexist, which is consistent with observing the main phase. Significant amounts of C and Li can be seen on the surface before ion sputtering, consistent with having residual Li and benzophenone on the surface of the material. Also, the Li signal is persistent throughout the doped samples after ion sputtering, in agreement with having Li present throughout the material.

3.3.4 Physical Properties

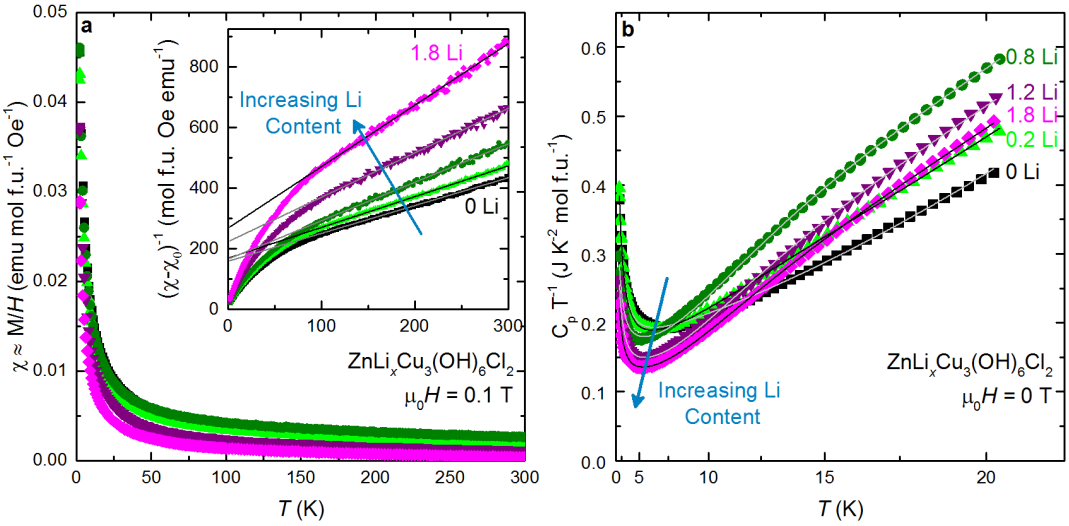

Figure 3.3.8: Physical properties of $ZnLi_xCu_3(OH)_6Cl_2$ series. **a)** The magnetic susceptibility, $\chi \approx M/H$, as a function of temperature for the doped $ZnLi_xCu_3(OH)_6Cl_2$ series. Black and gray lines are from high temperature Curie-Weiss analysis of the χ_0-corrected inverse magnetic susceptibility (inset). All samples have paramagnetic behavior and a decrease in susceptibility is seen as Li content increases. **b)** Heat capacity divided by temperature as a function of temperature under zero field from T =1.8-20 K. The low temperature region systematically decreases with increasing Li content across the series, while at higher temperatures the doped samples have increased entropy. Black and gray lines represent fits to the data.

Table 3.3.5: Extracted Curie Weiss parameters of $ZnLi_xCu_3(OH)_6Cl_2$ DC Magnetization data from the high temperature region (T = 100-300 K) and the low temperature region (T = 1.8-15 K).

Sample ID	Li Content x	HT θ(K) (K)	HT C (emu K mol^{-1} Oe^{-1})	HT χ_0 (emu mol^{-1} Oe^{-1})	LT θ (emu K mol^{-1} Oe^{-1})	LT C (emu mol^{-1} Oe^{-1})	LT χ_0
N	1.8(3)	-187(15)	0.50(5)	-9.0(2) x 10-4	-1.96(16)	0.082(8)	↑
A	1.8(3)	-132(11)	0.49(5)	-7.5(2) x 10-4	-1.91(15)	0.111(11)	
A2	1.2(3)	-152(12)	0.68(7)	3.5(2) x 10-4	-2.18(17)	0.151(15)	5.0(2) x 10-6
A3	0.8(3)	-130(10)	0.79(8)	8.0(2) x 10-4	-2.7(2)	0.21(2)	
B	0.2(15)	-166(13)	0.98(10)	-3.0(2) x 10-4	-2.8(2)	0.20(2)	
Parent	0.0(0)	-173(14)	1.09(11)	5.0(2) x 10-6	-3.0(2)	0.22(2)	↓

Table 3.3.6: HC model parameters from fit to zero field Heat capacity measurements to $ZnLi_xCu_3(OH)_6Cl_2$.

Sample ID	Li Content x	A_{LT} (mol f.u.$^{-1}$)	Δ_{LT} (K)	γ (J K^{-2} mol f.u.$^{-1}$)	A_{HT} (mol f.u.$^{-1}$)	Δ_{HT} (K)
A	1.8(3)	0.055(5)	↑	0.110(1)	0.84(8)	↑
A2	1.2(3)	0.066(7)		0.122(1)	0.99(10)	
A3	0.8(3)	0.065(7)	4.30(3)	0.152(1)	1.17(12)	73.250(8)
B	0.20(15)	0.114(11)		0.154(1)	0.42(4)	
Parent	0.0(0)	0.113(11)	↓	0.159(1)	0.00	↓

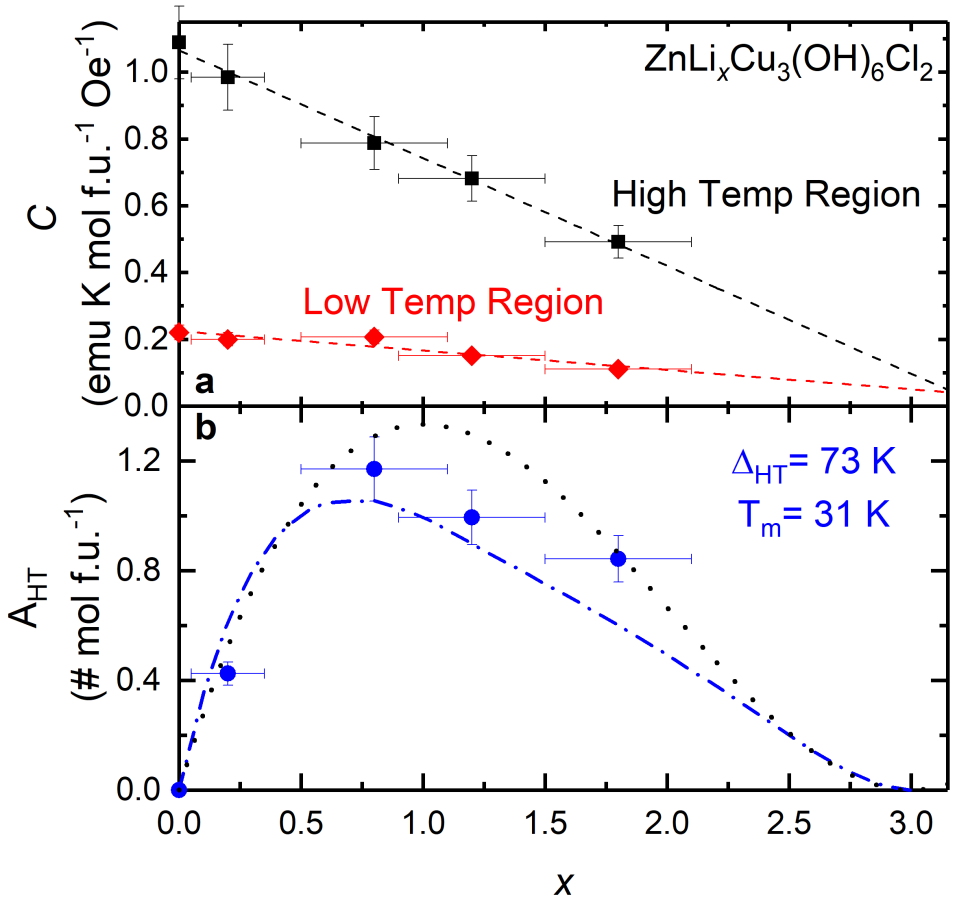

Figure 3.3.9: Magnetization and heat capacity fit parameters. **a)** The extracted Curie constants, C, from the high (black squares) and low (red diamonds) temperature Curie-Weiss analysis of the $ZnLi_xCu_3(OH)_6Cl_2$ series. The dashed lines are a guide to the eye that demonstrate a linear decrease. **b)** The Schottky anomaly parameter, A_{HT} (blue circles), from heat capacity fits to the doped Herbertsmithite series, which describes the feature in the high temperature heat capacity data. The blue dashed line and the black dotted line are two different models for singlet trapping in doped Herbertsmithite (see SI).

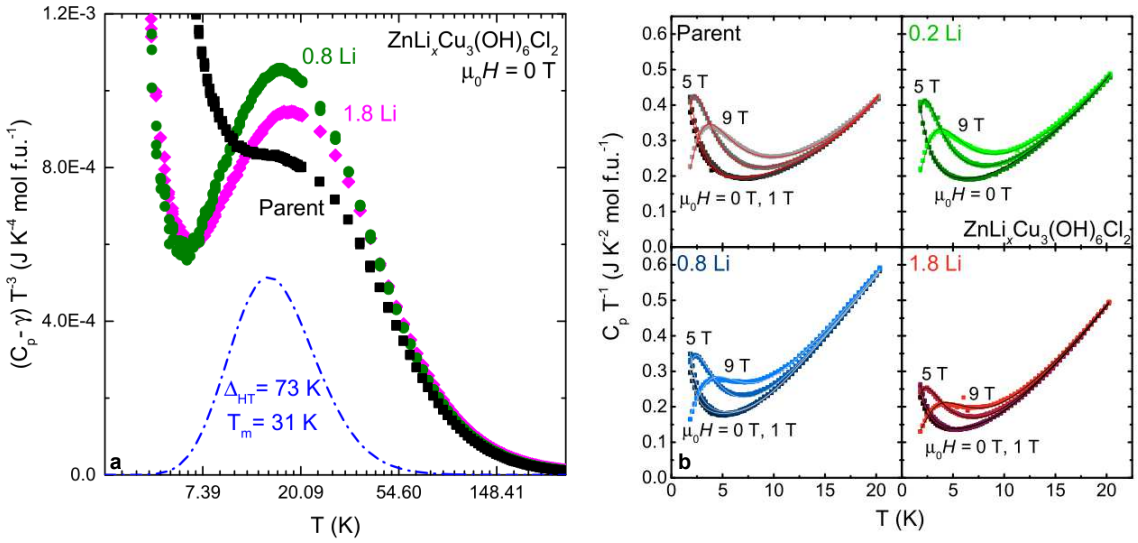

Figure 3.3.10: Detailed heat capacity analysis of $ZnLi_xCu_3(OH)_6Cl_2$ series. **a)** High temperature $(C_p - \gamma)\ T^{-3}$ Schottky analysis of the temperature range T =1.8-300 K for the parent $ZnCu_3(OH)_6Cl_2$ (black), $ZnLi_{0.8}Cu_3(OH)_6Cl_2$ (dark green), and $ZnLi_{0.8}Cu_3(OH)_6Cl_2$ (magenta). The dashed blue line is the high temperature Schottky anomaly of the extracted values from the zero field T = 1.8-20 K fits. It does a good job of describing the Schottky anomaly we see in the doped samples in higher temperature region of the heat capacity. Debye modes (which are a constant at low temperature and fall off at higher temperatures) are not shown for clarity. **b)** Simple model fits to field dependent heat capacity measurements. (top left) the Parent $ZnCu_3(OH)_6Cl_2$ (black), (top right) $ZnLi_{0.2}Cu_3(OH)_6Cl_2$ (green), (bottom left) $ZnLi_{0.8}Cu_3(OH)_6Cl_2$ (blue), and (bottom right) $ZnLi_{1.2}Cu_3(OH)_6Cl_2$ (red). The data sets go from a dark color at low fields to a lighter color at higher fields. The lines are fits as described in the text.

Table 3.3.7: HC model parameters from fit to field dependent heat capacity measurements of the $ZnLi_xCu_3(OH)_6Cl_2$ series

Sample ID	Li Content x	Applied $\mu_0 H$ T	A_{LT} (mol f.u.$^{-1}$)	Δ_{LT} (K)	γ (J K^{-2} mol f.u.$^{-1}$)	A_{HT} (mol f.u.$^{-1}$)	Δ_{HT} (K)
Parent	0	0	0.108(1)	4.73(5)	0.158(1)	0.00	0.00
Parent	0	1	0.128(1)	4.63(4)	↓	↓	↓
Parent	0	5	0.197(1)	7.58(2)			
Parent	0	9	0.211(1)	11.90(2)			
B	0.20(15)	0	0.115(1)	3.97(6)	0.160(1)	0.43(1)	75.6(8)
B	0.20(15)	5	0.183(1)	7.44(2)	↓	↓	↓
B	0.20(15)	9	0.197(1)	12.18(3)			
A3	0.8(3)	0	0.098(6)	2.6(1)	0.159(1)	1.10(1)	72.4(2)
A3	0.8(3)	1	0.118(4)	2.98(9)	↓	↓	↓
A3	0.8(3)	5	0.141(1)	7.88(3)			
A3	0.8(3)	9	0.162(1)	14.29(5)			
A	1.8(3)	0	0.062(1)	3.34(9)	0.115(1)	0.85(1)	75.5(2)
A	1.8(3)	1	0.077(1)	3.46(7)	↓	↓	↓
A	1.8(3)	5	0.101(1)	7.68(3)			
A	1.8(3)	9	0.114(1)	13.37(4)			

Despite the introduction of a substantial number of electrons, the material remains insulating: two probe room temperature resistance measurements on cold pressed pellets in a glovebox give a resistance > 2 MΩ for the doped series. Fig.3.3.8(a) shows the magnetic susceptibility, $\chi \approx M/H$, for the $ZnLi_xCu_3(OH)_6Cl_2$ series. For $x = 0$, the inverse magnetic susceptibility is well-known to be linear at high temperatures and dominated by the kagomé network, with the signal at $T < 20$ K containing significant contributions from defect Cu^{2+} ions on the Zn^{2+} site between kagomé layers[**?**]. We thus performed fits to the Curie-Weiss law in the low temperature (T = 1.8-15 K) and high temperature (T = 100-300 K) regions to extract estimates of the number of spins arising from the intrinsic and excess Cu ions respectively as a function of x. The extracted Curie constants of both the low and high temperature regions decrease linearly with increasing doping level, Fig.3.3.9(a). This systematic decrease is consistent with the reduction of magnetic Cu^{2+} ($S = 1/2$) to non-magnetic Cu^{1+} ($S = 0$). With an x-intercept value of $x = 3.3(5)$, the high temperature extrapolation to zero is also consistent with the known stoichiometry of Herbertsmithite, $Zn_{0.85}Cu_{3.15}(OH)_6Cl_2$, where $x = 3.15$ would be necessary to convert all Cu^{2+} to Cu^{1+}. All of the Weiss temperatures are negative, becoming less negative upon doping (see SI), in agreement with the expectation that the number of spins are reduced in the lattice. The low temperature extrapolation x-intercept value is $x = 3.9(9)$; this is within error equal to that found from the high temperature extrapolation. Any subtle divergence between the high and low temperature x-intercept likely reflects a difference in reducibility of the kagomé compared to the interlayer Cu^{2+} ions, since the high temperature paramagnetism includes both the kagomé and interlayer spins, whereas the latter is attributable only to the interlayer defect spins. Given the placement of the Li ions near the kagomé layer, it is no surprise the kagomé layers are more greatly reduced than the interlayer sites. Further, the difference in local coordination (interlayer Cu in O_6 octahedron vs kagomé Cu in O_4Cl_2 octahedron), would result in a difference in redox potential for $Cu^{2+} + e^- \rightarrow Cu^{1+}$ between the two sites, so reducing one should be slightly more favorable than reducing the other.

Fig.3.3.8(b) shows the low temperature heat capacity. There are two regions of significant entropy change as a function of doping: at $T \approx 5$ K, the heat capacity of the sample decreases with increasing Li content while at higher temperatures, there is an entropy gain at non-zero x. Qualitatively, the low temperature data can be explained by same mechanism as the magnetization, namely a reduction of the number of spins as Cu^{2+} is converted to Cu^{1+}.

Heat Capacity Model

To more quantitatively describe the changes, we parameterized the temperature-dependent data as a function of composition and applied magnetic field with the model:

$$C_p = \gamma T + \beta_3 T^3 + \beta_5 T^5 + A_{LT} f(\Delta_{LT}, T) + A_{HT} f(\Delta_{HT}, T) \tag{3.1}$$

$$A f(\Delta, T) = AR(\Delta/T)^2 \frac{e^{\Delta/T}}{(1+e^{\Delta/T})^2} \tag{3.2}$$

The γT term captures the linear contribution to the specific heat from the spin liquid (either intrinsic or due to defect spins). The phonon contribution is described by the $\beta_3 T^3$ and $\beta_5 T^5$ terms[**?**]. These phonon terms were calculated based on the field fit to the parent. The terms were then held constant for the remaining series at , $\beta_3 = 4.66(1)*10^{-4}$ J K^{-4} mol^{-1} and β_5 =4.45(1)*10^{-7} J K^{-6} mol^{-1} respectively. A two level Schottky anomaly, $A_{LT} f(\Delta_{LT}, T)$, where A_{LT} is the scaling factor which determines the peak intensity and Δ_{LT} the size of the gap, accounts for the contribution from defect spins from interlayer Cu^{2+}. A second two level Schottky anomaly, $A_{HT} f(\Delta_{HT}, T)$, describes the high temperature features. To reduce the number of independent parameters, the phonon contributions were held fixed across all refinements, as the inserted lithium should result in high frequency modes with only small perturbations of the low temperature phonon spectrum. Further, in initial fits, the magnitude of the gap, Δ_{HT} = 73 K (T_m = 31 K), of the high temperature Schottky anomaly was found to not vary significantly and thus held constant. Results from

the final refinements are given in the SI. While we caution against over-interpretation of many of the obtained values, the magnitude of the high temperature Schottky anomaly, A_{HT}, is robust; this was checked by comparing the predictions from fits up to T = 20 K, to the data extending up to T = 300 K in Fig.3.3.10(a). Upon doping, A_{HT} (Fig.3.3.9(b)) sharply increases then begins to gradually decrease.

This model also fits to the field dependent heat capacity, shown in Fig.3.3.10(b). Similar to the zero field data, the phonon terms, $\beta_3 T^3$ and $\beta_5 T^5$, were calculated based on the field fit to the parent and held constant at the above values for the remaining series. The parameters γ, A_{HT}, and Δ_{HT} were shared across fields for each sample and each sample was refined independently until convergence. These constraints yielded results consistent with the zero field fits. All the fits clearly demonstrate the field dependence of the low temperature feature which is consistent with a contribution from the magnetic interlayer Cu^{2+}. The low temperature magnetization measurements, sensitive to the interlayer Cu on the Zn site, indicate that these interlayer Cu atoms are also systematically reduced as a function of doping. If these Cu impurities give rise to the finite γ, it is expected that γ would also be reduced with doping as observed. Alternately, if the γT term describes the spin liquid contribution to the heat capacity, a systematic decrease in this value could be explained by the reduction of the spin liquid nature of the material as electrons are introduced into the system. More interestingly, the high temperature Schottky anomaly shows no field dependence and reproduces the trend seen in the zero field data. Direct assignment of the heat capacity terms to specific origins is future work, but it is promising that a single model recapitulates data across temperatures, fields, and composition.

3.3.5 Singlet Trapping and Electron Localization Models

This experimental data is in good agreement with two models for singlet trapping as a function of doping; a Monte Carlo simulation of the trapping of neighboring singlets by Cu^{1+} defects (blue dashed line Fig.3.3.9(b)) and a calculation of singlet trapping by local-

ized electrons on Cu triangles in the kagomé lattice (black dotted line) (described further below). Since the magnitude of the gap is on the same order as the expected singlet-triplet gap energy in isolated valence bonds in Herbertsmithite[83], it is alluring to interpret the growth in high temperature specific heat as arising due to the trapping of valence bonds into a glass or solid-like state. However, further work is needed to exclude other possibilities, such as a localized oscillator mode arising from the inserted Li ions. The singlet trapping models are also in agreement with the magnetization data. Every intercalated Li atom reduces one Cu atom, removing its spin contribution and yielding a one-to-one relationship. So upon doping, the Curie constant will linearly go to zero, in agreement with the experimental data.

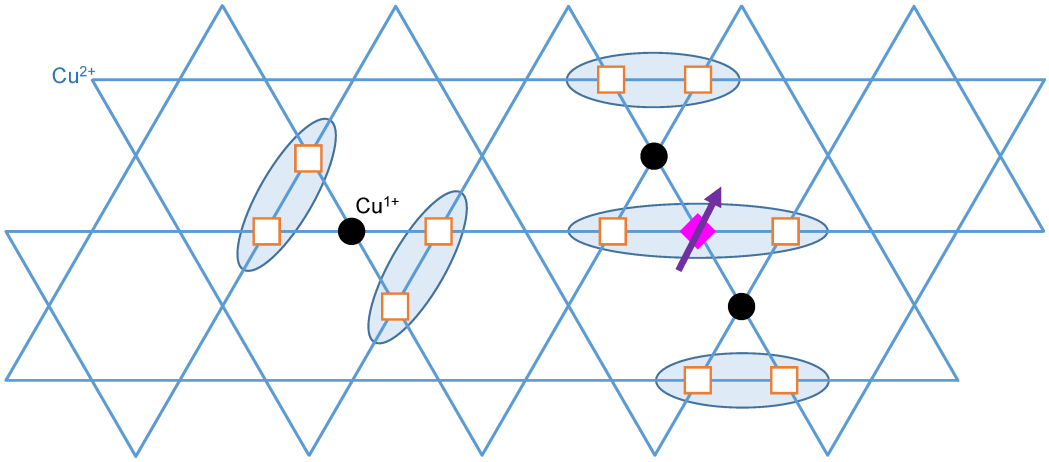

Figure 3.3.11: Singlet trapping schematic. This representation displays a possible configuration on the kagomé copper lattice using our counting rules. The blue lines represent the kagomé lattice of Cu^{2+} sites, the black circles are Cu^{1+} sites introduced into the lattice, the orange squares are constrained spin sites, and the magenta diamond is a unconstrained spin site. Singlet states are represented by light blue ovals.

In the first singlet trapping model, when Li is intercalated into the Herbertsmithite, a copper on the kagomé lattice is reduced from Cu^{2+} ($S = 1/2$) to Cu^{1+} ($S = 0$). This new Cu^{1+} site now has an electron pair, removing the magnetic moment on that Cu site

and trapping adjacent singlets. The singlet to triplet excitation could explain the excess heat capacity seen in the doped series. We preformed a Monte Carlo simulation using the following assumptions. In the case of a single Cu^{1+} defect, four neighboring Cu^{2+} sites have a constrained spin, giving rise to two singlet states (2 constrained spins = 1 singlet). The situation increases in complexity as more Cu^{1+} defects are introduced into the lattice, however the effects can be captured by a few counting rules. If multiple Cu^{1+} defects are present, any Cu^{2+} site that is neighbored by an odd number of defects is spin constrained, while an even number of defect neighbors would result in an unconstrained spin (Fig.3.3.11). Using these counting rules, a Monte Carlo simulation was run to map with the heat capacity parameter A_{HT} (mol f.u.$^{-1}$). The singlet trapping simulation is plotted (blue dotted line) in Figure 3.3.9(b) in the main text and they are in good agreement.

If it were purely Robin-Day Class 1 mixed valence (pure Cu^{1+} and Cu^{2+} sites with no interactions of ground or excited states), then indeed, we would expect a mixed XPS Signal of Cu^{1+} and Cu^{2+} with an approximate 2:1 ratio. In this case, however, no interactions between neighboring Cu^{1+} and Cu^{2+} is highly unlikely, given the shared hydroxyl bridge, through which we know (from the parent) that adjacent Cu ions interact. This model (which has discrete Cu^{1+} and Cu^{2+} ions, Robin-Day Class 2), would not only suppress the Cu^{2+} satellites but also give rise to an optical intervalence charge transfer, which would explain the black color of the material upon even light doping. But this is only one possibility. Li intercalation could also lead to localization on the Cu triangles as shown in Fig.3.3.12. This would be consistent with a Robin-Day class 3 mixed valence picture and also in agreement with the present data.

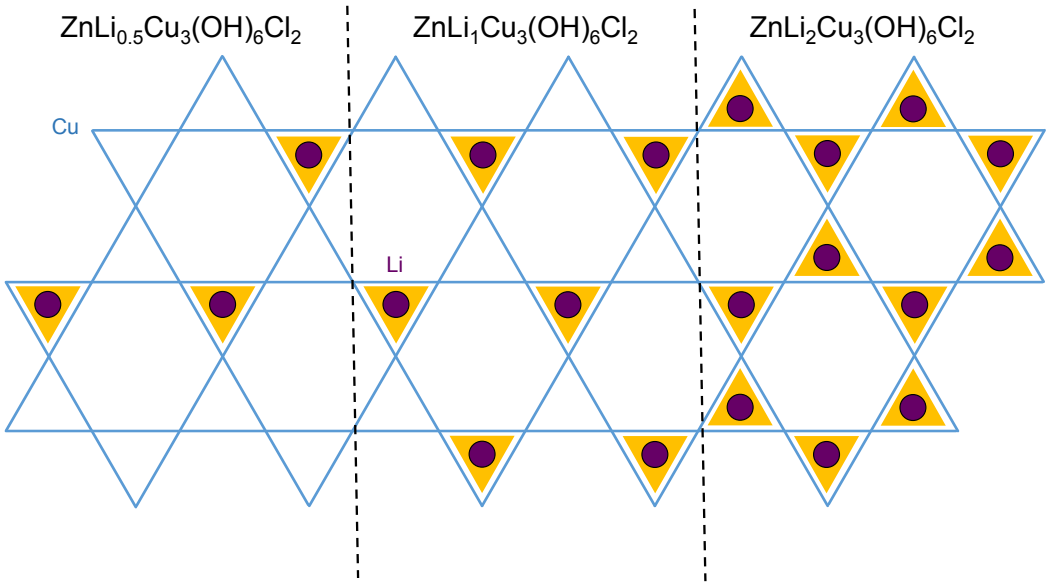

Figure 3.3.12: Electron trapping on the Cu Triangle schematic. This representation displays a possible configuration on the kagomé copper lattice. The blue lines represent the kagomé lattice of Cu^{2+} sites, the purple circles are intercalated Li^{1+} atoms introduced onto the lattice, and the yellow triangles are electron trapped on the triangle clusters.

To create a localized Cu triangle model to predict the singlet-triplet excitation's contribution to the heat capacity, it was assumed that the electrons were completely localized on Cu triangle sites. Given this, the Cu triangles could have a four possible states upon doping; 3 unconstrained electrons (parent state), 2 unconstrained electrons (singlet state), 1 unconstrained electron, and completely constrained (fully Cu^{1+}).

$$1 = (1-a)^3 + 3(1-a)^2 a + 3(1-a)a^2 + a^3 \tag{3.3}$$

The probability of each of those states is represented respectively by equation 3.3 as a function of a, where $a = 3x$ in $ZnLi_xCu_3(OH)_6Cl_2$. The 2 unconstrained electrons state would give rise a singlet to triplet excitation. If the high temperature feature in the heat capacity data is due to this excitation, one would expect probability of state 2, $3(1-a)2a$, to map with the heat capacity parameter A_{HT}. The localized Cu triangle model is plotted

(black dotted line) in Figure 3.3.9, and they are in good agreement. This model also has it limitations as it assumes completely localized Cu triangle clusters and does not take into account the effect of the position of subsequent Li atom, especially at higher concentrations ($x > 1$). Also, since the Cu triangles are limited to 4 possible states with single atom Cu oxidation states of 2+, 1.66+, 1.33+, and 1+ respectively, the calculation would be modeling a system with Robin-Day Class 2.

Despite the limitations of both models, they are in strong agreement with the observed magnitude of the higher temperature Schottky anomaly parameter, A_{HT}. Regardless of the microscopic details, the insulating nature of all specimens and the fact that the magnetic moments are monotonically and linearly reduced upon doping, directly demonstrates carrier localization. It is up to theorists to determine which is most likely in this material.

3.4 Conclusion

In conclusion, we have successfully introduced electrons into the prototypical kagomé quantum spin liquid Herbertsmithite. Despite the predictions, the doping of this system did not lead to metallicity or superconductivity down to T = 1.8 K. The magnetic field, temperature, and composition dependent specific heat all fit remarkably well to a single model. What are the precise physical origins responsible for this behavior? It is plausible that the location of the inserted Li ions provides a sufficiently strong disorder potential that Anderson localization is never overcome, irrespective of electron count, but other explanations cannot be ruled out[29][84]. The interesting physics is the following: why does charge doping this spin liquid not change it into a metal? The lower connectivity, with the 2-D kagomé lattice connects to four magnetic neighbors (n = 4) as compared to six magnetic neighbors of a 2-D triangular lattice (n = 6), may also play a role in the doped series behavior. Previous pressure and doping studies on higher connectivity frustrated geometries, such as organic triangular lattice κ-$(ET)_2Cu_2(CN)_3$[85], Na_xCoO_2[86], and

$Na_4Ir_3O_8$[87, 88] display metallicity. However, to our knowledge, no one has successfully induced metallic behavior in lower connectivity magnetically frustrated structures such as the kagomé (n = 4) or honeycomb lattice (n = 3). And finally, what is the nature of the ground state of doped Herbertsmithite? Our results demonstrate the need for an improved approach to describe and predict how electron doping effects magnetically frustrated narrow band insulators and implies that, if metallicity is to be induced, the doping method must involve chemical changes far from the kagomé layers.

3.5 Materials and Methods

Phase-pure Herbertsmithite was synthesized hydrothermally in a sealed 21 mL acid digestion vessel. Stoichiometric amounts of $ZnCl_2$ and $Cu_2(OH)_2CO_3$ in 10 mL of H_2O were ramped to 210 °C at 60 °C h^{-1}, held for 24 h, and cooled to room temp at 6 °C h^{-1}. Several batches were made by this process and thoroughly mixed in order to achieve a large supply of the parent material. All further chemical manipulations were done in Schlenk flasks using air-free techniques. Various amounts of Li were added to a 0.20 M benzophenone (Ph_2CO) in THF solution and allowed to stir overnight until all Li dissolved yielding a deep blue or purple solution depending on Li content. The parent Herbertsmithite was then added under the following conditions for the following samples: sample A ($x = 1.8$) was made by intercalation using 1 g of parent material in 50 mL with a molar ratio of 1:1.25 Ph_2CO:Li metal and refluxed for 24 h, sample B ($x = 0.2$) was made by intercalation using 1 g of parent material in 30 mL with a molar ratio of 1.1:1 Ph_2CO:Li metal and heated at 45 °C for 24 h, sample N ($x = 1.8$) was made by intercalation using 3 g of parent material in 200 mL with a molar ratio of 1:1.25 Ph_2CO:Li metal and refluxed for 48 h. 75 mg of sample A ($x = 1.8$) was deintercalated with 15.0 mL and 25.0 mL of 4.50(2) mM I_2 in acetonitrile at room temperature until solution became clear to create $x = 1.2$ (A2) and $x = 0.8$ (A3) samples respectively.

Laboratory X-ray powder diffraction patterns were collected using Cu Kα radiation (λ = 1.5418 $\AA$) on a Bruker D8 Focus diffractometer with a LynxEye detector. Powder neutron diffraction data of sample N at 300 K were collected at the Spallation Neutron Source NOMAD diffractometer (BL-1B) at the Oak Ridge National Laboratory and analyzed with the Rietveld method using GSAS/EXPGUI[89, 90]. Compositions of the maximally doped specimens were fixed at the values obtained from NPD; the composition of deintercalated samples was determined by the known quantity of oxidant consumed. All other compositions were estimated based on magnetization data.

X-ray photoelectron spectra were collected using Mg Kα radiation (1253.6 eV, 15 kV, 300 W) with a pass energy of 58.7 eV, 0.125 eV/step at 50 ms/step on a PHI 5600 XPS. Select samples were ion sputtered with 4 keV Ar^+ for 5, 15, 60 and 100 min (ion sputter area 6 x 6 mm^2, target current 1.0(3) μA) with a differential ion gun. XP spectra were energy adjusted to ion sputter cleaned copper metal $Cu2p_{3/2}$ with CasaXPS software. Error in peak position for the Cu 2p and Cu $L_3M_{4,5}M_{4,5}$ envelopes were estimated to be $\pm$ 3 step sizes (0.375 eV).

Magnetization and heat capacity measurements were measured on powders and cold pressed pellets respectively in a Quantum Design Physical Properties Measurement System. Magnetizations were measured from T = 1.8-300 K under a field of $\mu_0 H$ = 0.1 T and susceptibility estimated as $\chi = M/H$. Heat capacity was measured in triplicate at each point using the semi-adiabatic pulse technique. Data was collected from T = 1.8-300 K under $\mu_0 H$ = 0 T and from T = 1.8-20 K under $\mu_0 H$ = 1, 5, 9 T. Two probe contact resistivity measurements with a voltmeter on the series of cold pressed polycrystalline samples at room temperature indicated a resistance of $>$2MΩ.

3.6 Work in Progress and Future Outlook

3.6.1 Li Location and Local Structure: Neutron Powder Diffraction (NPD) and Pair Distribution Function (NPDF)

Additional neutron diffraction data was collected on Herbertsmithite and isotropically pure ^{7}Li doped derivatives at the Spallation Neutron Source at Oak Ridge National Laboratory (SNS ORNL) on the POWGEN and NOMAD beam lines (IPTS-16834). Six samples were measured: $Zn^7Li_xCu_3(OH)_6Cl_2$ with $x = 0$, 0.2, 1.8 and the deuterated counterpart $Zn^7Li_yCu_3(OD)_6Cl_2$ with $y = 0$, 0.2, 1.8. The isotropically pure Li allows for refinements with a known scattering factor, unlike the previous experiment which had an unknown mixture of Li isotopes.

Joint Rietveld refinements of x-ray and neutron powder diffraction experiments

The ^{7}Li POWGEN data is in agreement with the structure refinements reported earlier in this chapter. GSAS II is being used for the joint Rietveld refinement of the POWGEN neutron powder diffraction and x-ray synchrotron powder diffraction from the advance photon source (APS). The systematic refinements show slight differences in the parent vs. doped patterns. However, obtaining an excellent fit to the long range structure for the heavily doped samples remains challenging due to scattering from unknown decomposition products. The decomposition products are more prominent in the neutron data compared to x-ray suggesting that they are composed of lighter atoms such as organics. This is consistent with the carbon detected the XPS experiments.

Local Structure: Neutron Pair Distribution Function (NPDF)

Pair distribution function is a diffraction analysis technique which calculates the real space radial distribution of atoms. For example, a Cu-Cu bond with a distance of 3 Å will produce a peak at 3 Å, and a next nearest neighbor (NNN) Zn at 5 Å will produce another peak at

5 Å (and so on and so forth subsequent neighbors). NPDF data is collected similarly to other neutron diffraction such as POWGEN experiments. Where it differs is that NPDF diffractometers, such as NOMAD, collect data out to very high Q (momentum space). The data collected in momentum space is then Fourier transformed to calculate the real space PDF. PDF analysis can be performed with any diffraction data. However, for data with a small Q range, the Fourier transform is taken of a truncated data set leading to large termination ripples which obscures any significant structural components in the data. The large Q range allows NPDF analysis to probes the local structure of a material as opposed to normal PXRD experiments will measure the average long range structure. NPDF is therefore better equipped to probe the structure of doped Herbertsmithite since the Li is likely disordered over any significant distance.

Initial attempts to fit the NPDF data can be seen in Figure 3.6.1. The general strategy is to use the best fit long range structure from powder diffraction fits as a starting model, and then only refine the lattice parameters, thermal parameters, scale factor, and specific instrumental parameter. This shows the difference of the average model compared to the local structure data. From here, the local structure can be solved by refining the atomic positions, chemical short range order, anisotropic thermal parameters, and other local structure aspects. The parent Herbertsmithite, shown in **a)** and **b)**, has been fit to the NPDF data using the joint refinements (described above) as the starting model. Refining a few of the local parameters results in a qualitatively good fit. The NPD data most heavily doped sample, $Zn^{7}Li_{1.8}Cu_3(OD)_6Cl_2$, is overlaid on the parent data (purple) in Figure 3.6.1 **c)** and **d)**. It is evident that there are difference is both peak shape and intensities at different radial distances. Attempts to fit the doped samples are underway.

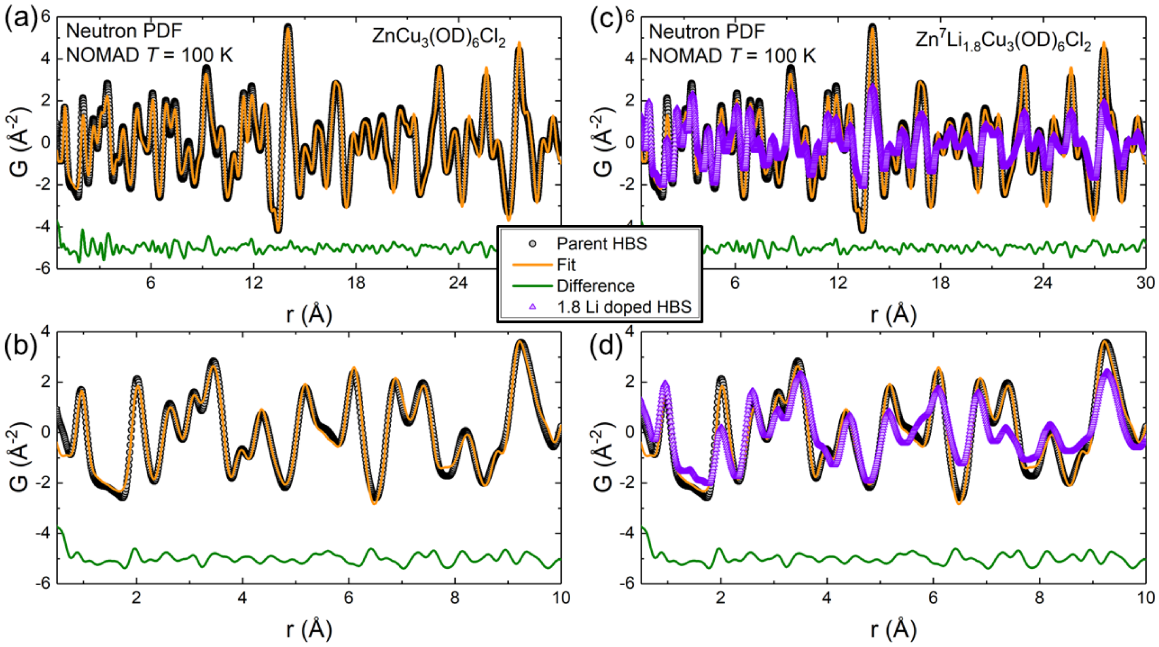

Figure 3.6.1: Neutron PDF fit (orange line) of **a)** parent $ZnCu_3(OD)_6Cl_2$ (black circle) overlaid with data collected on **c)** fully doped sample $ZnLi_{1.8}Cu_3(OD)_6Cl_2$. **b)** and **d)** are zoomed in to 0.5-10 Å to highlight the quality of the parent fit and the differences between the parent and doped samples.

Work continues on systematically adjusting structural models with different Li environments to best fit the NPD and XRPD data for the doped ^{7}Li samples to obtain the most accurate long range structure. Once a suitable long range structure has been solved, the model will be applied to the NPDF data to determine the local structure and possible locations of the Li atoms within the structure of Herbertsmithite.

3.6.2 Single Crystal Growth Optimization of Herbertsmithite

Introduction

Single crystals of quantum materials are often needed to better understand their ground states and properties. To measure the dynamics and quantum properties of these materials, crystals on the order of 1mm^3 are required for neutron scattering experiments and electronic measurements. Large single crystals are also needed to make devices which can be studied to design new electronic components utilizing their unique electronic prop-

erties. Polycrystalline synthetic Herbertsmithite, $ZnCu_3(OH)_6Cl_2$, was first grown under hydrothermal (aqueous) conditions in 2005.[65] Attempts to grow larger single crystals by this same method have failed. It has been proposed that this failure is due to the low decomposition temperature of $ZnCu_3(OH)_6Cl_2$ under these conditions and the formation of CO_2 bubbles causing a turbulent growth environment.[91] The overall reaction of the $ZnCu_3(OH)_6Cl_2$ hydrothermal synthesis is:

$$6H_2O + 3Cu_2(OH)_2CO_3 \rightarrow ZnCu_3(OH)_6Cl_2 + 3CO_3^{2-} + 6H^+ \tag{3.4}$$

$$CO_3^{2-} + 2H_3O^+ \leftrightharpoons HCO_3^- + H_3O^+ + H_2O \leftrightharpoons H_2CO_3 + 2H_2O \leftrightharpoons CO_2 + 3H_2O \tag{3.5}$$

Successful growth of millimeter size crystals of $ZnCu_3(OH)_6Cl_2$ was achieved in 2011 changing the copper source to CuO (eliminating CO_2 production and reducing initial Cu solubility) and by combining hydrothermal conditions with principles for another common crystal growth technique, chemical vapor transport. In chemical vapor transport, a temperature gradient is applied to a long reaction vessel, with the reactants on the hot end and the nucleation site on the cold end. The reactants go into solution, react, and eventually deposit the desired phase on the cold end. Typically, chemical vapor transport is done in the solid and vapor phases with the addition of a carrier gas to facilitate vaporization and transport. However, the $ZnCu_3(OH)_6Cl_2$ crystal growth, shown in Figure 3.6.2, is in an aqueous solution with the following overall reaction:

$$3H_2O + 3CuO + ZnCl_2 \rightarrow ZnCu_3(OH)_6Cl_2 \tag{3.6}$$

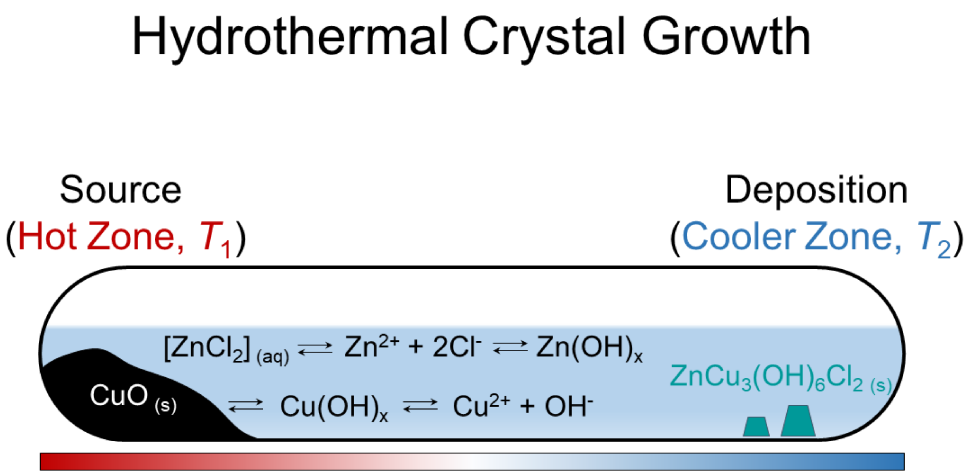

Figure 3.6.2: A diagram of the hydrothermal single crystal growth for $ZnCu_3(OH)_6Cl_2$. The starting material is heated in the source zone to increase solubility and to drive the reaction. The deposition zone is the cooler end where single crystals of $ZnCu_3(OH)_6Cl_2$ begin to grow.

Despite the successful growth of mm-size crystals, the reaction requires 20 weeks and has inconsistent results. For this type of crystal growth, there are a number of critical factors effecting consistency: the ratio of reactant availability and concentration, precise temperature control, stable temperature gradient, potential water currents causing mixing, and inconsistent nucleation surface between different glass vessels.

The crystal growth of $ZnCu_3(OH)_6Cl_2$ is likely highly dependent on the relative availability of Zn^{2+} and Cu^{2+} in solution compared to $Zn(OH)_2$ and $Cu(OH)_2$. This is supported by observing hydroxides formation in single crystal growth experiments. Herbertsmithite is the end member with the highest Zn content of the paratacamite family, $Zn_yCu_{4-y}(OH)_6Cl_2$, where $y = 0.85$, so a high availability of Zn^{2+} is important to achieve the correct stoichiometry. $Cu(OH)_2$ and $Zn(OH)_2$ are amphoteric allowing it to react with both acids and bases and also having different ion species availability under various conditions (Table 3.6.1). Given these equations, the thermodynamic speciation diagrams of the

Table 3.6.1: $Cu(OH)_x$ and $Zn(OH)_x$ equilibria in aqueous conditions

Equilibrium	K_f (K_{sp})
$Cu(OH)_2(s) \leftrightharpoons Cu(OH)_2(aq)$	(5 x 10^{-19})
$Zn^{2+} + H_2O \leftrightharpoons [Zn(OH)]^+ + H^+$	1.46 x 10^6
$Zn^{2+} + 2H_2O \leftrightharpoons Zn(OH)_2 + 2H^+$	1.51 x 10^{11}
$Zn^{2+} + 3H_2O \leftrightharpoons [Zn(OH)_3]^- + 3H^+$	7.59 x 10^{13}
$Zn^{2+} + 4H_2O \leftrightharpoons [Zn(OH)_4]^{2-} + 4H^+$	3.72 x 10^{15}
$Zn(OH)_2(s) \leftrightharpoons Zn(OH)_2(aq)$	(5 x 10^{-17})

dominant Cu and Zn species can be calculated as a function of pH as shown in Figure 3.6.3 **a** and **b**.

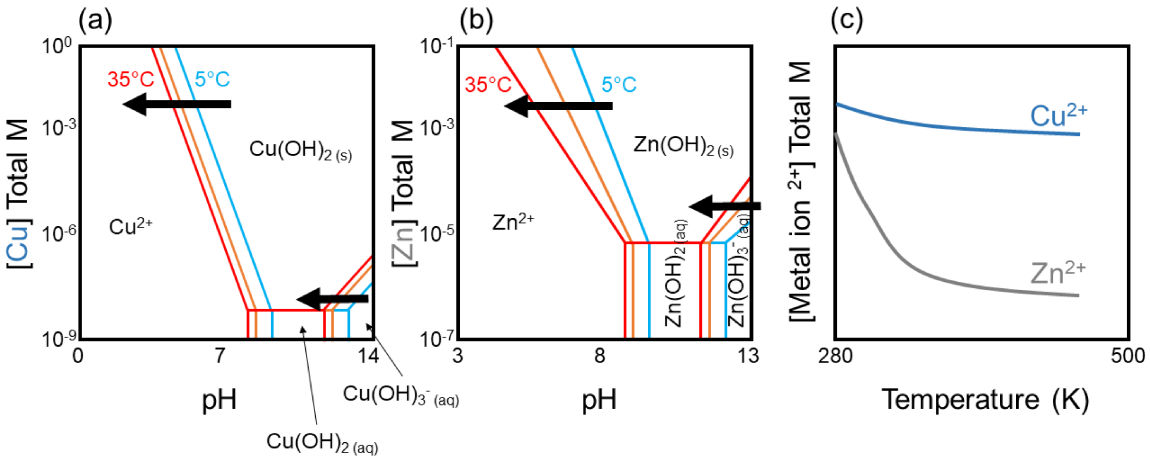

Figure 3.6.3: Representations of general thermodynamic speciation diagrams of the dominant **a** Cu and **b** Zn species as a function of pH and temperature. As the temperature increases from 5 °C (blue) to 25 °C (orange) to 35 °C (red), the dominant M^{2+} species area decreases. **c** a Sketch of the approximate effect of temperature on the availability of Cu^{2+} and Zn^{2+} as a function of temperature at a pH < 7.

Thermodynamic speciation diagrams show the dominant ionic species of a metal under different conditions. Although not shown, it is important to note that multiple species can coexist in each section. In the Cu diagram, Cu^{2+} is dominant at a lower pH values. As the temperature increases, the system begins to favor the hydroxides, especially at higher

concentrations. A similar trend is seen in the Zn diagram, however the effect of temperature is much greater, decreasing Zn^{2+} concentration at a faster rate as temperature increases compared to Cu^{2+} (Figure 3.6.3 **c**)

The goal is to understand the critical factors in the crystal growth of $ZnCu_3(OH)_6Cl_2$ to produce large reliable single crystals in the shortest time possible. The long growth times and inconsistent growths show that the current method is not fully optimized. This study examines the effects of different nucleation sites, temperature (magnitude and gradient), and the relative availability of Zn^{2+} and Cu^{2+} in solution through adjusting: the ratio and concentration of starting materials, the copper source, and the pH of the system. The growth principles discovered in Herbertsmithite can be leveraged to optimize the crystal growth conditions in other hydrothermal systems where sufficiently sized crystals are difficult to produce through typical methods.

Methods

Hydrothermal three zone Crystal Growth Experiments: A series of three zone hydrothermal crystal growth experiments were run to determine the critical factors for $ZnCu_3(OH)_6Cl_2$ single crystal growth. All three zone hydrothermal growth experiments were flame sealed in a 6 x 12 mm quartz tube. The reaction vessel is composed of an extra thick quartz to help withstand the pressure. At 180 °C, the pressure of water is about 10 bar, so only ∼50% of the vessel is filled with solution to allow compressible head space to avoid rupture due to the thermal expansion of water. All reagents were used as purchased without additional purification: CuO (99.995% BTC), $Cu_2(OH)_2CO_3$ (Cu 55% min Alfa Aesar), and anhydrous $ZnCl_2$ (99.95% Alfa Aesar). The quartz reaction vessels varied from 15-17 inches in total length to span all three zones. The specific concentrations and heating profiles for each reaction can be found in Tables 3.6.2, 3.6.4, 3.6.6, and 3.6.8.

Hydrothermal bomb (single temperature zone) Crystal Growth: All reactions were done in 21 mL Parr acid digestion vessel (bombs).The specific concentrations and heating pro-

files for each reaction can be found in Table 3.6.11.

Results and Discussion

During the crystal growth experiments, five types of macroscopic $ZnCu_3(OH)_6Cl_2$ structures were observed: Single crystal (SX), "dendrite" polycrystal (Dent), "high density" polycrystal (HDP), "light blue" polycrystal (LBP), and polycrystalline powder (pwdr). All structures are indistinguishable by powder X-ray diffraction with CuO (black powder) as the only impurity in some reactions. The ideal structure is single crystal as shown in figure 3.6.4 **a**. Single crystals consist of only one domain, however it is common during crystal growths for twinning, where a domain in a different orientation grows from one of the facets. The degree of twinning can vary from just one twin to many. The latter is the case for what will be referred to as the "dendrite" $ZnCu_3(OH)_6Cl_2$ structure (Figure 3.6.4 **b**). The dendrite structure is transparent and retains facets which are visible and clear but has multiple domains. Decreasing in crystallinity, the next macro-structure of $ZnCu_3(OH)_6Cl_2$ will be referred to as a high density polycrystal (HDP) which has randomly oriented domain sizes smaller than 0.05 mm and retains the dark blue-green color (Figure 3.6.4 **c**).

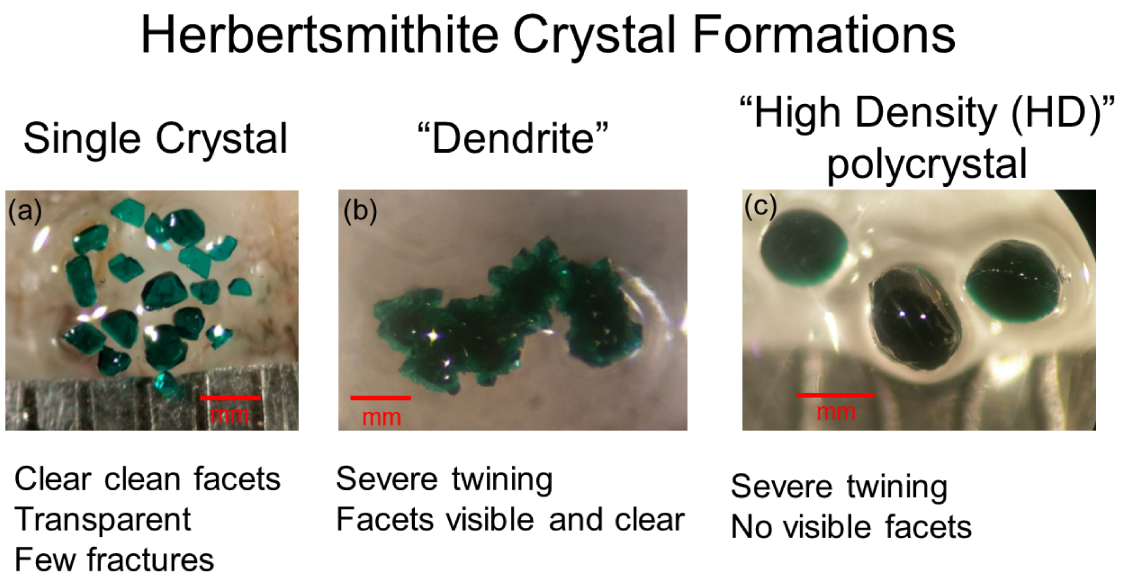

Figure 3.6.4: Photographs of three crystalline phases observed in $ZnCu_3(OH)_6Cl_2$ growth: **a)** single crystal, **b)** dendrite structure, and **c)** High density (HD) polycrystal. Crystallinity decreases from left to right

The forth structure is the ”light blue” polycrystal (LBP) which is distinct in color and shape compared to the above structures as shown in Figure 3.6.5 **a**. The LBP particles are roughly spherical with bumps on the surface and appear semi-transparent. Given the much lighter blue color, one possibility is that it is a different composition formed during a different stage of the reaction compared to the first three structures. The paratacamite family, $Zn_yCu_{4-y}(OH)_6Cl_2$, are all closely related in crystal symmetry which makes them extremely difficult to distinguish by XRD. Low temperature magnetization and elemental analysis are needed in order to determine the composition. For these experiments, the LBP structure will be considered a competing macro-structure of $ZnCu_3(OH)_6Cl_2$. The final structural state is the powder polycrystalline form of $ZnCu_3(OH)_6Cl_2$ which can either be a fine powder or in packed into clumps (Figure 3.6.5 **b**).

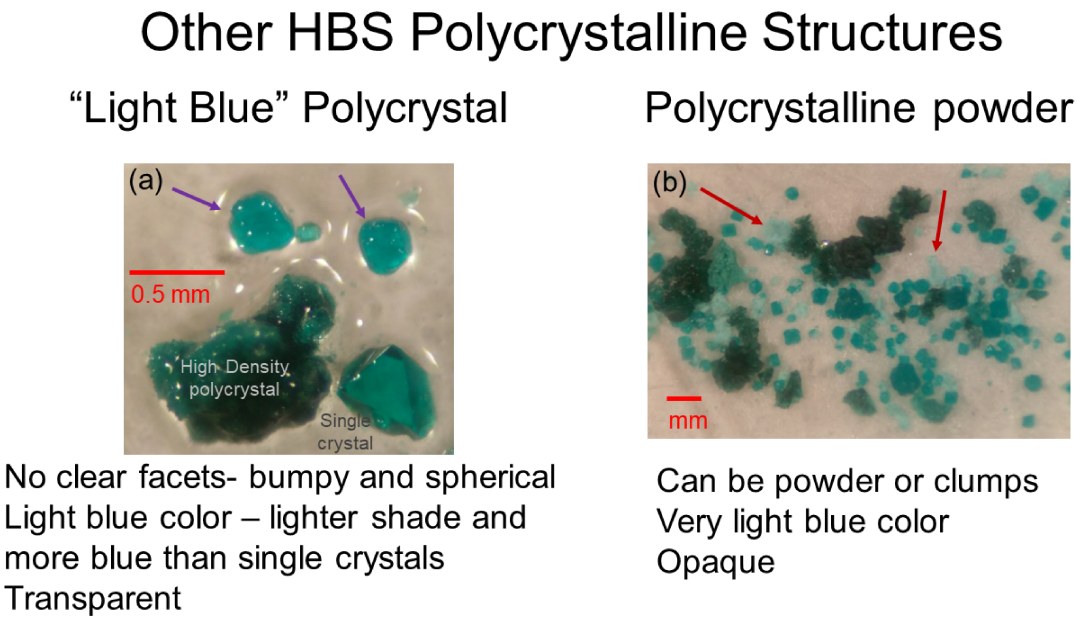

Figure 3.6.5: Photographs of two additional polycrystalline structures observed in $ZnCu_3(OH)_6Cl_2$ crystal growth: **a)** the light blue polycrystal (LBP) (purple arrows) and **b)** polycrystalline powder (red arrows). Photograph **b** is shown without oil to highlight the difference in color between dendrite, LBP, and polycrystalline powder.

Hydrothermal multiple zone Crystal Growth Experiments:

To determine the timescale for nucleation, several preliminary reactions were conducted at temperature ranging 180-210 °C (no gradient). The start of nucleation was seen after 1 day with noticeable growth to ~0.01 mm after 3 days (noticeable by eye). Next, a series of 8 day temperature gradient growths, Experiment 1: Table 3.6.2, were carried out to determine the rate of growth over this period. It consisted of three sets of reactions: 1) ZK148 8 day growth control 1, 2) ZK150 8 day growth control 2, and 3) ZK151 8 day growth 50% scale up. Within each set, the reactions were placed side-by-side in the same three zone furnace to control for temperature deviations.

Table 3.6.2: $ZnCu_3(OH)_6Cl_2$ crystal growth experiment 1 conditions.

Sample ID	Experiment	CuO (g)	CuO Conc (M)	$ZnCl_2$ (g)	$ZnCl_2$ Conc (M)	H_2O (mL)
ZK148-1	8 day growth	0.2352	0.657	2.0155	3.29	4.5
ZK148-2		0.2355	0.658	2.0154	3.29	4.5
ZK150-1	8 day growth	0.2355	0.658	2.0154	3.29	4.5
ZK150-2		0.2348	0.656	2.0155	3.29	4.5
ZK151-1	50% scale up - 8 day growth	0.3526	0.657	3.0255	3.29	6.75
ZK151-2		0.3522	0.656	3.0258	3.29	6.75

Table 3.6.3: $ZnCu_3(OH)_6Cl_2$ crystal growth experiment 1 results.

Sample ID	Single Xtals Present? (mm)	Other HBS structure (cold end)	Steps	Duration (h)
ZK148-1	less than 0.05 mm	LBP(greatest percent)	1.) All 180	96
ZK148-2	Yes (0.1-0.3)	LBP(greatest percent)	2.) gradient (180-160)	96
ZK150-1	not visible	LBP, jag HD, CuO, small Dents	1.) All 180	21
ZK150-2	Yes (0.3-0.5)	Mostly SX, some LBP, some jag HD	2.) gradient (180-160)	168
ZK151-1	No	LBP, jag HD with CuO, pwdr	1.) All 180	24
ZK151-2	No	Dent	2.) gradient (180-160)	168

The lack of repeatability in the first two sets demonstrates that this reaction is highly sensitive to several factors outside of broad temperature and concentration dependence, and it suggest that the current method is on the edge of stability for $ZnCu_3(OH)_6Cl_2$ single crystal growth. Furthermore the successful reactions produced crystals ranging from 0.1-0.5 mm demonstrating that a large portion of the growth occurs in a week time period suggesting that long crystal growth times (20 weeks) may not be necessary. The pressure of a reaction may play a role in single crystal formation as evident by the 50% scaled-up set of reactions, ZK151. Despite maintaining the same ratio, concentration, and temperature as the earlier sets and only increasing the solution volume to headspace ratio, the reactions failed to produce single crystals. Reaction ZK150-2 was the most successful, producing the both the largest single crystals and the greatest overall amount of SX structure relative to the other structures. The failed reaction of ZK150-1 consisted of LBP, jagger HDP, remnant CuO, with small Dents with domains less than 0.05 mm. In both the successful ZK148-2 and unsuccessful ZK148-1 trail, the dominant structure was LBP.

One potential factor that could be driving these inconsistent results within a reaction set is availability of nucleation sites. In experiment 2, several quartz tube treatments were tested to vary nucleation site type and concentrations: 1.) ZK153-A1 with and -A2 without quartz wool, 2.) ZK153-B quartz vessel defects on the cold end of the tube (B1-single dimple and B2-necked), and 3.) ZK153-C a pre-cleaning treatment with EtOH (C1-without and C2-with one dimple). The quartz wool was inserted after the initial reactants were added to keep all unsolvated particles (such as CuO) on the hot end so they can not act as a nucleation source on the cold end. The defects were produced with a torch before sealing the reaction and are proposed to change the type and concentration of nucleation sites as well as water circulation in that area. In the third set, the vessels were throughly cleaned with EtOH and Kim wipes to remove any possible dust or quartz particles. All reactions were heated in the same furnace for 7 days. The results are summarized in Table 3.6.4.

Table 3.6.4: $ZnCu_3(OH)_6Cl_2$ crystal growth experiment 2 conditions.

Sample ID	Experiment	CuO (g)	CuO Conc (M)	$ZnCl_2$ (g)	$ZnCl_2$ Conc (M)	H_2O (mL)
ZK153-A1	w/o q wool	0.2348	0.656	2.0148	3.28	4.5
ZK153-A2	w/ q wool	0.2347	0.656	2.0156	3.29	4.5
ZK153-B1	point dimple	0.2353	0.657	2.0149	3.28	4.5
ZK153-B2	neck	0.235	0.657	2.0151	3.29	4.5
ZK153-C1	EtOH clean w/o dimple	0.2351	0.657	2.0151	3.29	4.5
ZK153-C2	EtOH clean w/ dimple	0.2352	0.657	2.0149	3.28	4.5

Table 3.6.5: $ZnCu_3(OH)_6Cl_2$ crystal growth experiment 2 results.

Sample ID	Single Xtals Present? (mm)	Other HBS structure (cold end)	Steps	Duration (h)
ZK153-A1	No	LBP, jag HD with CuO	1.) All 180	24
ZK153-A2	No	LBP, q fiber (low yield)	2.) gradient (180-160)	144
ZK153-B1	No	LBP, jag HD, Dent, pwdr Chucks		
ZK153-B2	No	large round HD (snow cap)		
ZK153-C1	No	jag HD, pwdr Chunks		
ZK153-C2	No	jag HD with CuO/pwdr, pwdr Chunks, some btw Dent-HD		

None of these reactions produced single crystals despite having very similar temperature and concentration conditions as experiment 1. The quartz wool, ZK153-A2, seemed to be detrimental to the yield of $ZnCu_3(OH)_6Cl_2$ on the cold end of the vessel, instead preferring to remain at the hot end without transporting through the quartz wool to the cold end. This suggests that $ZnCu_3(OH)_6Cl_2$ may not very soluble after it is formed and that an insoluble particle may seed the reaction. Interesting, the LBP structure was the only $ZnCu_3(OH)_6Cl_2$ structure seen in the quartz wool reaction on the cold end. Lack of the HDP structure suggest that CuO may be responsible for seeding all HDP structures, which are seen in all the other reactions in experiment 2. Visual evidence also support an relationship between CuO and the HDP structure where some HDP formations can be observed growing off of black CuO particles. The prevalence of the LBP structure in the quartz wool reaction could also possibly be due to LBP nucleation by the wool itself.

Given this results, a third experiment was run to determine if $ZnCu_3(OH)_6Cl_2$ single crystal growth can be seeded by previously grown $ZnCu_3(OH)_6Cl_2$ single crystals. The reaction run time was extended to 12 weeks to determine if substantial growth took place. Many of the reactions are repeated conditions from experiment 2 with the addition of seed crystals as explained in Table 3.6.6.

Table 3.6.6: $ZnCu_3(OH)_6Cl_2$ crystal growth experiment 3 conditions.

Sample ID	Experiment	CuO (g)	CuO Conc (M)	$ZnCl_2$ (g)	$ZnCl_2$ Conc (M)	H_2O (mL)
ZK156-D1	1 dimple	0.2346	0.655	2.0153	3.29	4.5
ZK156-D2	1 dimple	0.2348	0.656	2.0152	3.29	4.5
ZK156-D3	neck - seeded	0.235	0.657	2.0149	3.28	4.5
ZK156-E1	Seeded two xtals w/ q wool	0.2352	0.657	2.0153	3.29	4.5
ZK156-E2	Seeded one xtal no wool	0.2354	0.658	2.0149	3.28	4.5
ZK156-E3	Control (no seed no wool no dimple)	0.235	0.657	2.0151	3.29	4.5

Table 3.6.7: $ZnCu_3(OH)_6Cl_2$ crystal growth experiment 3 results.

Sample ID	Single Xtals Present? (mm)	Other HBS structure (cold end)	Steps	Duration (h)
ZK156-D1	No	Dent, CuO coating some places (100% reacted)	1.) All 180	2
ZK156-D2	No	Dent, CuO coating some places (100% reacted)	2.) gradient (180-160)	2160
ZK156-D3	one shattered seed Xtal	pwdr		
ZK156-E1	(no trace of seed)	pwdr, pwdrChunks		
ZK156-E2	(no trace of seed)	pwdr, pwdrChunks		
ZK156-E3	Yes (0.1-0.3)	Dent, HD, LBP		

The unseeded reactions ZK153-D1 and D2 had the starting reactants on the hot end dislodge at some point in the growth producing a large piece of Dendrite structure covered in some CuO. All of the seeded reactions failed, resulting only in polycrystalline powder. One of the reactions, D3, the seed was found but fractured into several pieces. Seeds were not recovered for either E1 or E2. This could be due to the seeds being crushed into small pieces or being redissolved into the solution. Redissolving the seeds seems unlikely since the seed was recovered in ZK156-D3. The only reaction to produce SX was the control reaction, yielding single crystals ranging in size from 0.1-0.3 mm. The additional growth time did not add significantly to the growth of single crystals.

The solubility of CuO as well as its potential to act as a seed could be major contributors to the crystal growth environment. To test this, the Cu source was changed to more soluble $Cu_2(OH)_2CO_3$. Several conditions were tested as described in Table 3.6.8

Table 3.6.8: $ZnCu_3(OH)_6Cl_2$ crystal growth experiment 4 conditions.

Sample ID	Experiment	$Cu_2(OH)_2CO_3$ (g)	Conc (M)	CuO (g)	Conc (M)
ZK162A-1	New Cu source - Xtal Conc and ratio from CuO growth	0.6538	0.657		
ZK162A-2	New Cu source - Repeat of A1	0.653	0.656		
ZK162B	New Cu source - Hydrothermal conditions (conc and ratio)	0.6608	0.299		
ZK162C	New Cu source - higher conc hydrothermal bomb conditions	0.6607	0.664		
ZK162D	CuO control			0.2355	0.658
ZK164A-1	repeat of 162 A1 with higher temp (190-170 C)	0.6532	0.656		
ZK164A-2	repeat of 162 A1 with higher temp (190-170 C)	0.6534	0.657		
ZK162A-1	(with ZK164A1 and A2) 2nd Heat (190-170 C)				
ZK162A-1	(alone) 3rd Heat (190-170 C)				

Table 3.6.9: $ZnCu_3(OH)_6Cl_2$ crystal growth experiment 4 results.

Sample ID	$ZnCl_2$ (g)	Conc (M)	H_2O (mL)	SX Present? (mm)	Other HBS structure (cold end)	Steps	Duration (h)
ZK162A-1	2.0152	3.29	4.5	Yes (0.2-0.4)	large Dent-HD	1.) gradient (180-155)	48
ZK162A-2	2.0151	3.29	4.5	Yes (0.1-0.3)	large Dent-HD deposit	2.) gradient (180 - 160 C)	120
ZK162B	0.31	0.23	10	No	fine pwdr		
ZK162C	0.3109	0.51	4.5	No	fine pwdr		
ZK162D	2.0149	3.28	4.5	No	Dull blueish gray powder, CuO		
ZK164A-1	2.0157	3.29	4.5	No	HD, powder	1.) gradient 190-170	168
ZK164A-2	2.0148	3.28	4.5	No	HD, powder		
ZK162A-1				no change			
ZK162A-1				no change		1.) gradient 190-170	168

Under similar temperature and concentration condition as the CuO growth, reactions with $Cu_2(OH)_2CO_3$ successfully grew 0.2-0.4 mm single crystals in 1 week. Attempts to grow crystals under the conditions reported for hydrothermal polycrystalline powder yielded only fine polycrystalline powder. This demonstrates that the production of CO_2 is not the driving force behind unsuccessful crystal growths in hydrothermal bombs, but growth is dependent on the concentrations and ratios of the starting materials as well as the temperature gradient.

Hydrothermal bomb (single temperature zone) Crystal Growth:

Given the success of the $Cu_2(OH)_2CO_3$ single crystal synthesis, I wanted to determine how critical the temperature gradient and vessel geometry is for single crystal formation. To test this, a series of crystal growths were attempted using hydrothermal bombs. The use of hydrothermal bombs has the great advantage of precise temperature control. These reactions can be run in a highly accurate low temperature oven that is capable of cooling rates of 1 °C/h compared to the highly temperature variable three zone furnaces at low temperatures. The reactions are listed in Table 3.6.11.

Table 3.6.10: . $ZnCu_3(OH)_6Cl_2$ Hydrothermal single zone crystal growth experiment.

Sample ID	Conditions	$Cu_2(OH)_2CO_3$ (g)	Conc (M)	CuO (g)	Conc (M)	$ZnCl_2$ (g)	Conc (M)	H_2O (mL)
ZK199	Control	0.6536	0.657			2.0156	3.29	4.5
ZK200	FTO glass as substrate	0.653	0.656			2.0153	3.29	4.5
ZK201	seeded with two seeds	0.653	0.656			2.0151	3.29	4.5
ZK202	5 drops EtOH	0.6534	0.657			2.0154	3.29	4.5
ZK204	one seed (162 A2)	0.6602	0.299			0.8215	0.60	10
ZK205	one seed (162 A2)	0.6605	0.299			1.6309	1.20	10
ZK206	one seed (162 A2)			0.2347	0.295	2.0149	1.48	10
ZK207	one seed (162 A2)			0.2348	0.590	2.015	2.96	5
ZK208	CuO ratio			0.239	0.601	1.0075	1.48	5
ZK209	CuO ratio			0.239	0.601	4.03	5.91	5
ZK210	CuO ratio			0.12	0.302	2.015	2.96	5
ZK211	CuO ratio			0.4775	1.201	2.015	2.96	5

Table 3.6.11: . $ZnCu_3(OH)_6Cl_2$ Hydrothermal single zone crystal growth experiment continued.

Sample ID	SX?	Heating sequence	Results
ZK199	No	McNulty	fine blue/green powder
ZK200	No	3 days at 180 C - transfer to Snoop	fine blue/green powder - No Xtals - poor week coating
ZK201	No	Snoop - transfer	No new Xtals but recovered the seeds, looks similar in size and shape
ZK202	No	slow cool at 3 C/hr	fine blue/green powder - No Xtals
ZK204	No	Snoop	Fine blue/green powder
ZK205	No	3 days at 210 C	Fine blue/green powder
ZK206	No	slow cool at 2 C/hr	larger and darker HDP
ZK207	No		larger and darker HPD
ZK208	No	Snoop	larger and darker HPD
ZK209	No	3 days at 180 C	larger and darker HPD
ZK210	No	slow cool at 1 C/hr	larger and darker HDP
ZK211	No		larger and darker HPD

Despite having the same concentration and max temperature of the successful $Cu_2(OH)_2CO_3$ single crystal growths, only fine polycrystalline powder was formed in the $Cu_2(OH)_2CO_3$ hydrothermal growths. The seed was recovered in the reaction at 180 °C, ZK201, but were unable to be recovered in reactions at 210 °C. The CuO trials did produce some HDP structures, which further support the CuO seeding hypothesis. However no single crystals were grown. The temperature gradient and reaction vessel geometry of the three zone experiments appear to be instrumental for large $ZnCu_3(OH)_6Cl_2$ crystal growth.

Conclusions and Future Experiments

So far, it has been determined that there are 5 main structures that can be formed when attempting $ZnCu_3(OH)_6Cl_2$ single crystal growths. The current synthesis method is on the edge of stability where small differences in sample preparation greatly effecting the results. It has been determined that the majority of crystal growth can happen on the order of a few weeks, and $Cu_2(OH)_2CO_3$ can be successfully used to produce high quality single crystals. The three zone geometry and temperature gradient seem to be critical for successful growth as determined by the hydrothermal bomb experiments.

Currently, crystal growths experiments buffered at various pH values are being explored to tune the availability of Cu^{2+} and Zn^{2+} and potentially lead to more stable growths. Also, one of the major challenges is imprecise temperature control in the multi-zone furnaces. These furnaces are designed to be operated > 400 °C. While operating at 160-200 °C, drifts in temperature were measured at +/- 3 °C. It would be helpful to build a low temperature three zone transparent oven to carry out these measurements and be able to adjust temperatures based on real-time visible observations.

3.6.3 Barlowite Doping Attempts

Barlowite, $Cu_4(OH)_6BrF$, is a compound structurally related to Herbertsmithite which also has a $S = 1/2$ kagomé on a copper lattice and is a potential QSL candidate. As such, it

would be interesting to dope this material to see how it compares to the behavior seen in doped Herbertsmithite. Initial attempts to dope Barlowite (under the same conditions as Herbertsmithite) have lead to complete decomposition. Even under the mildest conditions, such as reducing the Li:Ph_2CO ratio below 1 to avoid the dianion and diluting the solution's concentration by a factor of 10, the Barlowite structure completely decomposes. Work is underway to find a different reducing system with a lower reduction potential of Li intercalation.

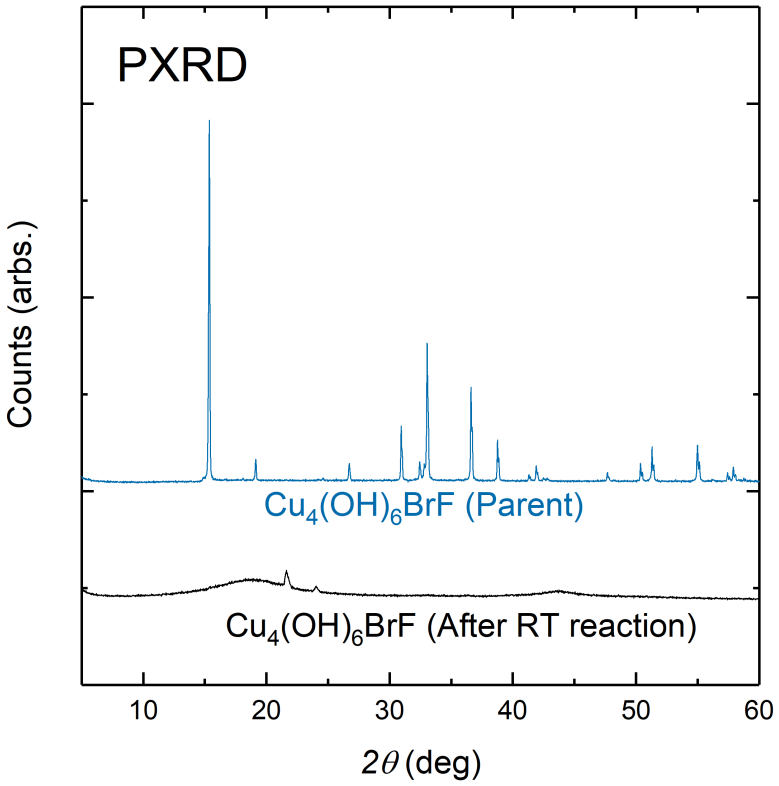

Figure 3.6.6: PXRD of Barlowite before and after the RT Li:Ph_2CO 0.91:1 reaction.

3.7 Acknowledgments

This work was supported by the NSF, Division of Materials Research (DMR), Solid State Chemistry (SSMC), CAREER grant under Award DMR-1253562 and the David and Lucile

Packard Foundation. TMM was supported by the Institute for Quantum Matter, under Grant No. DE-FG02- 08ER46544. Z.A.K. acknowledges the assistance of A. Huq and K. Page in collecting powder neutron data from POWGEN and NOMAD/SNS. Z.A.K and T.M.M. also thank H.D. Fairbrother and the Surface Analysis Laboratory in the Department of Material Science and Engineering at The Johns Hopkins University, and O. Tchernyshyov for useful discussions.

4 Emergent Ferroelectricity in the S = 1 Kagomé Magnet $Na_2Ti_3Cl_8$

This work was co-written with the following authors and is published under
the following citation:
(SUBMITTED) *npj Quantum Materials.* **X**, X-X (2018)
http://dx.doi.org/XXXXXXXXXXX

Zachary A. Kelly,[a,b] T.T. Tran[a,b] and Tyrel M. McQueen[a,b,c,*]

[a]Department of Chemistry, The Johns Hopkins University, Baltimore, MD, USA

[b]Institute for Quantum Matter, The Department of Physics and Astronomy,
The Johns Hopkins University, Baltimore, MD, USA

[c]Department of Materials Science and Engineering,
The Johns Hopkins University, Baltimore, MD, USA

[*]Corresponding Author

4.1 Abstract

Kagomé lattice magnets have emerged as a versatile platform on which to discover and explore the underlying physics of quantum spin liquids and related states of matter, though experimental examples of ideal kagomé lattices remain rare. Here we report the realization of an ideal $S = 1$ kagomé in $Na_2Ti_3Cl_8$. This material undergoes a discrete two-step trimeriza-

tion on cooling, transforming from a centrosymmetric high temperature (HT) $R\bar{3}m$ phase to non-centrosymmetric, ferroelectric intermediate (IT) and low temperature (LT) $R3m$ phases via successive first order phase transitions and the formation of metal-metal bonds. Symmetry mode decomposition analysis reveals the activation of the proper ferroelectric order parameter Γ_2^- upon trimerization. Thus $Na_2Ti_3Cl_8$ demonstrates a novel mechanism to obtain proper ferroelectricity driven by frustrated magnetism and metal-metal bonding, and highlights the rich physics arising from kagomé lattice materials.

4.2 Introduction

Magnetic frustration, born from strong antiferromagnetic interactions on a geometrically frustrated lattice, has proven to be a fertile playground for the discovery of exotic emergent phenomena. Many known frustrated systems, from the highly coordinated triangular and pyrochlore lattices to lower coordinated honeycomb and diamond lattices, display collective quantum behavior.[36, 92, 93] In particular, the kagomé -lattice, composed of corner sharing triangles with four nearest neighbors, is one of the most extensively studied magnetically frustrated systems since fractionalized excitations were observed in a S = 1/2 kagomé , Herbertsmithite, a hallmark of a realized quantum spin liquid state.[45] Interest has been growing in integer spin antiferromagnetic kagomé systems in search of various quantum ground states, such as the 2D valence bond solid.[51] This ground state has a spin gap formed by entangled S = 1/2 edge spins from termination of the S = 1 kagomé lattice, a 2D analog to the Haldane state in S = 1 chains. The S = 1 kagomé lattice has also been theorized to host other exotic ground states such as the hexagonal singlet state as well as structural instabilities leading to spontaneous trimerization.[49] To date, there are only a few candidates of these integer spin kagomé states for experimentalists to explore.[50, 94–96]

Recently, magnetic frustration has been shown to drive other emergent phenomena, such

as ferroelectricity, a spontaneous macroscopic electric polarization.[97, 98] Ferroelectrics are driven by a distortion which can be categorized as either proper, primary polar Brillouin zone-centered lattice distortion, or improper, nonpolar zone-boundary distortion which indirectly leads to ferroelectricity.[54]

Most highly frustrated ferroelectrics are classified as improper and have mechanisms involving charge or magnetic order, displaying ferroelectricity through strong electron correlations without a structural transition. Magnetically frustrated triangular lattice systems, such as $CuCrO_2$ and $NaFeO_2$, become magnetically ordered at low temperatures into complex spiral spin states.[99–102] However, there are no reports of magnetic frustration driving a proper ferroelectric transition. Here, we report the structure and properties of a perfect $S = 1$ kagomé , $Na_2Ti_3Cl_8$ which exhibits a discrete two-step trimerization upon cooling. Trimerization of an $S = 1$ kagomé to relieve magnetic frustration is predicted, however the stabilization of a discrete intermediate phase is entirely unexpected. Furthermore, this unique distortion driven by metal-metal bonding induces the activation of proper zone-center ferroelectric modes unlike any other reported ferroelectric. $Na_2Ti_3Cl_8$ hosts a novel inversion symmetry-breaking mechanism that can be used to design a new class of proper ferroelectrics through metal-metal bonding.

The structure of $Na_2Ti_3Cl_8$ was determined by single crystal and powder X-ray diffraction (PXRD). At $T = 300$ K, $Na_2Ti_3Cl_8$ adopts a high temperature (HT) $R\bar{3}m$ phase. The HT phase consists of 2D sheets of edge sharing $TiCl_6$ octahedra forming a perfect Ti kagomé lattice in the ab plane with $S = 1$ on each Ti (Fig. 1). The kagomé layers are separated by Na atoms nested in a trigonal prismatic Cl cage. Upon cooling, the polycrystalline powder goes through a first-order phase transition to an intermediate temperature (IT) $R3m$ phase followed by a second first order phase transition to a low temperature (LT) $R3m$ phase. However on warming, the LT phase persists until $T \approx 240$ K before converting back to the HT phase, bypassing the IT phase. This asymmetric hysteretic loop is observed in PXRD, magnetization, and heat capacity measurements. After trapping the IT

phase upon cooling, warming studies demonstrate its metastability with a hysteretic loop persisting up to $T \approx 220$ K.

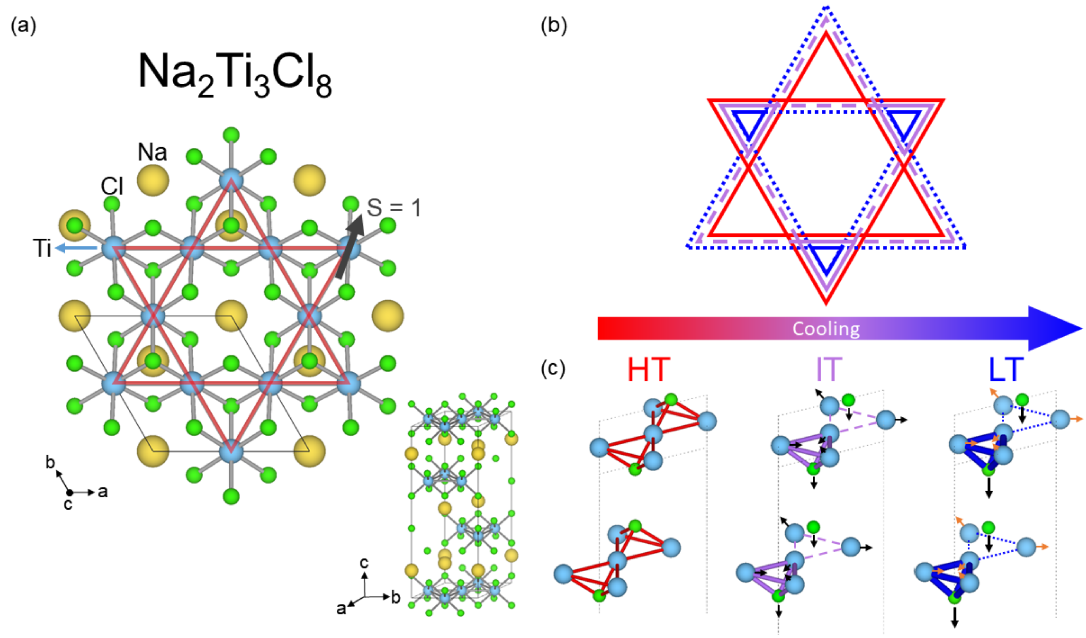

Figure 4.2.1: **a)** The top and side illustration of $Na_2Ti_3Cl_8$ high temperature (HT) $R\bar{3}m$ phase from single crystal X-ray diffraction. The solid red lines highlight the Ti kagomé lattice. A cartoon of the discrete two-step trimerization of the Ti kagomé lattice is shown in **b)** as the Ti form metal-metal bonds. **c)** The trimerization drives the formation of a ferroelectric state. Sodium atoms have been removed for clarity.

4.3 Results

4.3.1 Structure

Temperature dependent PXRD shows the existence of two successive first order phase transitions on cooling, Figure 4.3.1 **a** and **c**. There is a clear two-step contraction (expansion) of the a (c) lattice parameter as $Na_2Ti_3Cl_8$ transitions from HT $\rightarrow$ IT $\rightarrow$ LT. The a and c lattice parameters of the IT phase are almost exactly half way between the HT and LT phases as a = 7.41 $\rightarrow$ 7.22 $\rightarrow$ 6.99 $\AA$ and c = 19.72 $\rightarrow$ 19.97 $\rightarrow$ 20.28 $\AA$. A small, <5%, fraction of the IT phase persists down to $T = 12$ K. A large hysteresis is observed on warming, with a transition directly from the LT to HT phase at $T = 237$ K, Figure 4.3.1 **b** and **d**. This type

of asymmetric hysteresis is rare, especially given that the slow warming rate of 1 K h^{-1} should limit superheating.

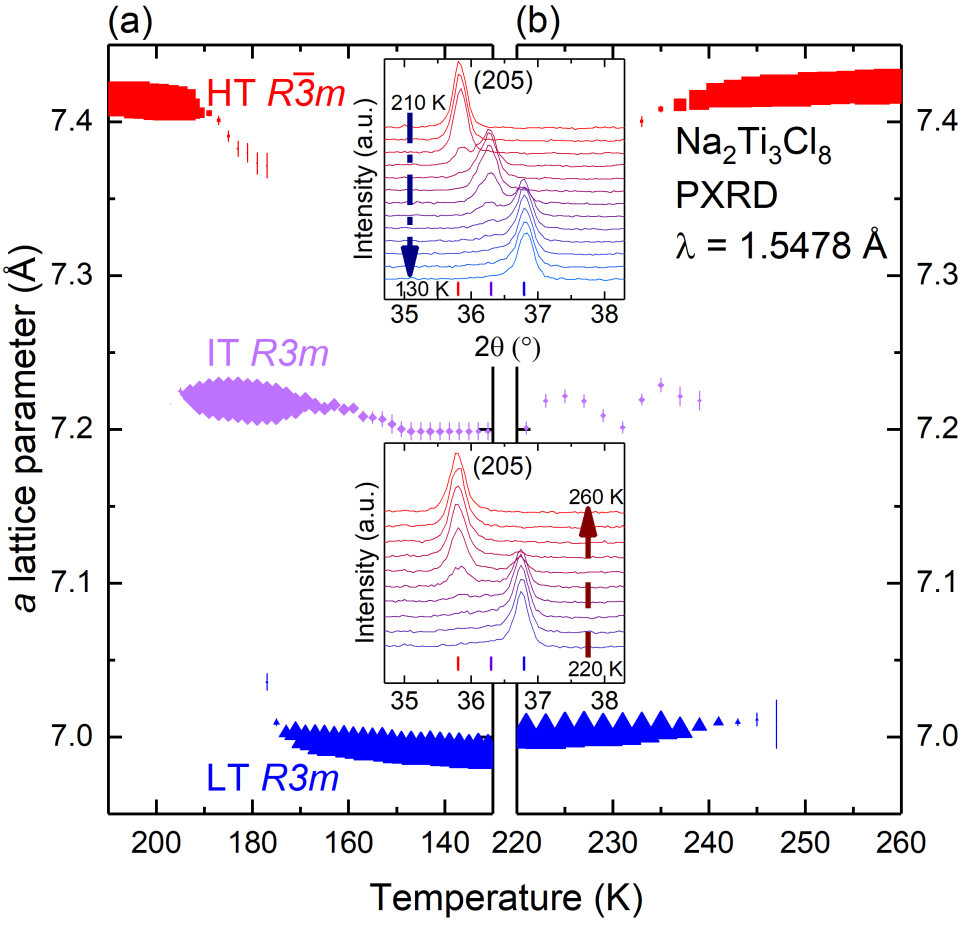

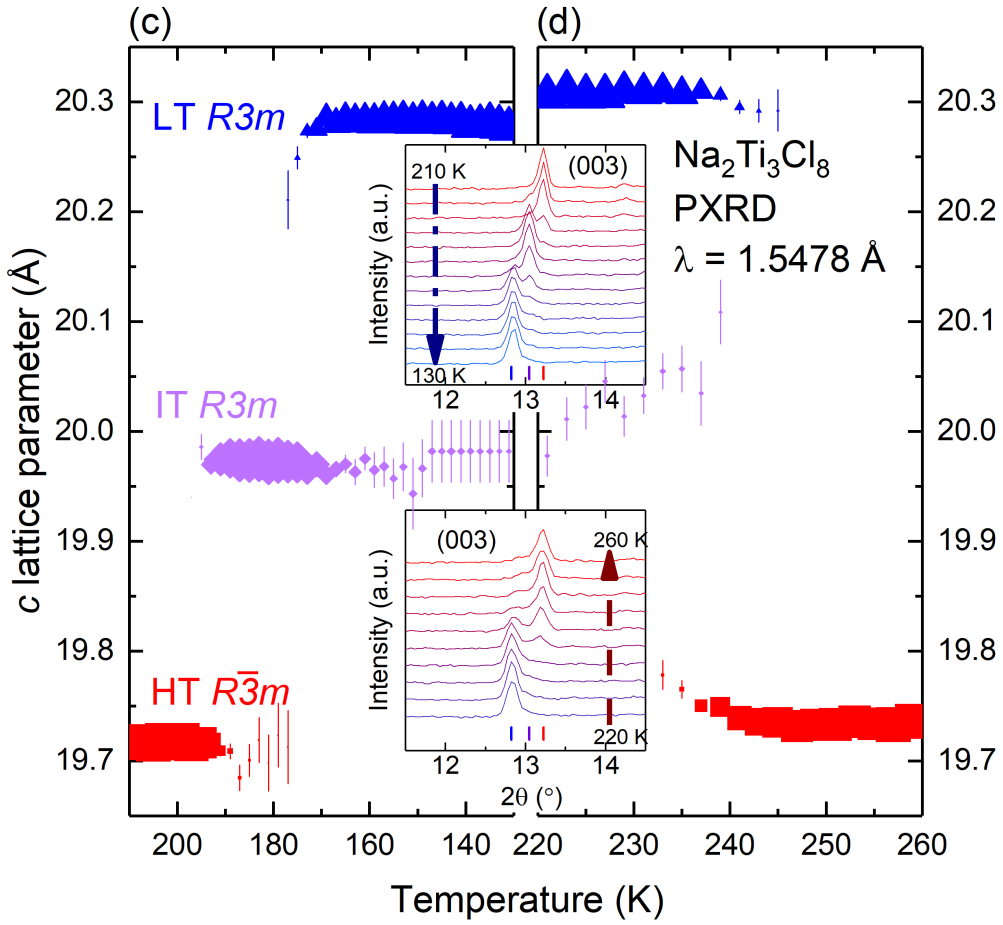

Figure 4.3.1: The resulting *a* and *c* lattice parameters from Rietveld refinements of laboratory powder X-ray data of $Na_2Ti_3Cl_8$ upon (**a** and **c**) cooling and subsequent (**b** and **d**) warming at a continuous rate of 1 K h^{-1}. Three distinct phases are present; a high temperature phase (HT - red squares) in space group $R\bar{3}m$, an intermediate temperature phase (IT - purple diamonds) in $R3m$, and a low temperature phase (LT - blue triangles) in $R3m$. The size of the marker corresponds to the phase fraction. The insets show the PXRD reflection (**a** and **b**) (205) and (**c** and **d**) (003) as a function of decreasing temperature (red to blue) moving down the y-axis. The IT phase reflection, represented by the purple tick, is strongly observed upon cooling while unobserved upon heating.

The large stepwise changes in lattice parameter are driven by significant changes in Ti-Ti distances, Figure 4.3.2 **a**. In the HT phase, all nearest neighbor distances are equivalent, 3.7 *Å*. Upon transitioning to the IT phase, there is trimerization resulting in large and small Ti_3 triangles, Figure 4.2.1**b**, with corresponding long and short Ti-Ti distances of 3.8 *Å* and

3.4 $\AA$, respectively. This trimerization is further enhanced to 3.9 $\AA$ and 3.1 $\AA$, respectively, upon transitioning to the LT phase. The Ti-Ti distances in the IT phase are approximately halfway between the values for the HT and LT phases.

This trimerization also drives the expansion along the c axis. Each Ti_3 triangle has a single apical Cl. These Cl atoms alternate above and below the kagomé plane for adjacent triangles. In the IT phase, every other Ti_3 triangle trimerizes. To maintain optimal Ti-Cl distances this drives all apical Cl atoms away from the kagomé plane on one side and towards the kagomé plane on the other. There are two important consequences: first the c lattice parameter increases; second the Ti_3Cl_8 plane develops a net electric polarization, i.e. becomes ferroelectric due to the asymmetric positions of Cl anions perpendicular to the kagomé layer. These displacements occur in the same direction in adjacent kagomé layers resulting in the loss of inversion symmetry and the formation of a ferroelectric state. As with the changes in the *ab* plane, these changes along c are enhanced upon the transition to the LT phase.

The main structural features of the HT and LT phases observed by PXRD are further supported by single crystal X-ray diffraction experiments (Table 4.3.1). No evidence of a supercell or incommensurate order was found for either the HT or LT phase. The Flack parameter was determined to be 0.42(2), indicating merohedral twinning. There is no correlation of atomic coordinates and thermal displacements between the atoms in the LT structure, confirming the loss of inversion center symmetry. Together these results demonstrate the formation of a ferroelectric state in LT-$Na_2Ti_3Cl_8$. In the single crystal X-ray diffraction experiments, the IT phase is not observed and the cooling transition temperature to the LT phase is significantly suppressed to $\sim$140 K. This is not surprising given the $\sim$5% contraction in a and $\sim$3% expansion in c are energy intensive to propagate across a large single crystal. Powder experiments with variable amounts of grinding show that the temperature of the transitions and the occurrence of the IT phase is strongly dependent on the particle size of the powder.

Table 4.3.1: Single crystal X-ray diffraction refinement results for $R\bar{3}m$ HT phase and $R3m$ LT phase of $Na_2Ti_3Cl_8$

$Na_2Ti_3Cl_8$	HT Phase	LT Phase
M/g mol^{-1}	473.28	473.28
T/K	220(2)	110(2)
λ/Å	0.71073	0.71073
Crystal system	trigonal	trigonal
Space group	$R\bar{3}m$ (166)	$R3m$ (160)
aÅ	7.3955(11)	6.9718(10)
c/Å	19.628(4)	20.208(4)
α/°	90	90
γ/°	120	120
V/Å^3	929.7(3)	850.6(3)
Z	3	3
Dc/g cm^{-}3	2.536	2.772
μ/mm^{-1}	3.626	3.963
2θ min/°	3.114	3.024
2θ max/°	33.124	32.8
Number of reflections	476	814
Number of parameters	17	32
R_{int}	0.0524	0.0794
GOF	1.149	1.077
$R(F)^a$	0.0398	0.0775
$R_w(F_o^2)^b$	0.0773	0.1856
Flack	N/A	0.42(2)

Table 4.3.2: Powder Rietveld refinement of $Na_2Ti_3Cl_8$ intermediate temperature (IT) *R*3*m* phase.

$Na_2Ti_3Cl_8$	IT Phase
M/g mol^{-1}	473.28
T/K	179(1)
λ/Å	1.5418
Crystal system	trigonal
Space group	*R*3*m* (160)
a/Å	7.2181(5)
c/Å	19.974(2)
α/°	90
γ/°	120
V/Å^3	901.2(2)
Grain Size L/nm	100(6)
Strain G	0.54(2)
V/Å^3	901.2(2)
Dc/g cm^{-3}	2.616
R_p	9.09
R_wp	11.50
GOF (χ^2)	1.29

Table 4.3.3: Powder Rietveld refinement of $Na_2Ti_3Cl_8$ intermediate temperature (IT) *R*3*m* phase. Occupancies were fixed at unity base on single crystal X-ray diffraction of the HT and LT phase. Isotropic temperature factors, B_{eq}, were jointly refined for each element type. Errors represent statistical uncertainties.

Site	Np	*x*	*y*	*z*	Atom	Occ.	B_{eq}
Ti1	9	0.513(1)	1.025(3)	0.997(3)	Ti	1	1.2(3)
Na1	3	1	1	0.835(2)	Na	1 2.1(7)	
Na2	3	1	1	0.157(2)	Na	1 2.1(7)	
Cl1	3	1	1	0.598(1)	Cl	1 0.7(2)	
Cl2	3	1	1	0.409(1)	Cl	1 0.7(2)	
Cl3	9	0.827(2)	0.173(2)	0.069(1)	Cl	1	0.7(2)
Cl4	9	0.173(2)	0.826(2)	0.924(1)	Cl	1	0.7(2)

4.3.2 Mode Decomposition

To further explore the nature of the low temperature phase transitions a mode decomposition analysis of the structural changes was performed. According to the Landau theory, a phase transition can be understood as a symmetry-breaking distortion, where the lower symmetry distorted phase is a subgroup of higher symmetry parent phase.[54] Symmetry modes defined by irreducible representations (irreps) describe mutually exclusive collective movement of atoms making them extremely useful for quantifying the structural degrees of freedom resulting from a distortion. Mode decomposition analysis captures changes in lattice parameter and atomic position by breaking down a phase transition into strains and amplitudes of these allowed symmetry-modes.[55] The type of irrep is determined by the phase transition pathway defined by the starting and ending space group. This analysis allows for the exhaustive and quantitative understanding of the distortions within the unit cell during a phase transition and the identification of allowed properties such as ferroelectricity. In the case of $Na_2Ti_3Cl_8$, the inversion center is broken as HT ($R\bar{3}m$) $\rightarrow$ IT and LT ($R3m$), described by the irrep $\Gamma_2{}^-$. The $\Gamma_2{}^-$ irrep allows the proper ferroelectric symmetry-modes. Within this primary order parameter there are a set of allowed displacive modes classified according to the atoms involved.[103] Using ISODISTORT, the phase transition decomposes into 6 distinct atom-specific symmetry-modes: 2 Ti modes ($\Gamma_2{}^-$ B_{u1}, $\Gamma_2{}^-$ B_{u2}), 1 Na mode ($\Gamma_2{}^-$ A_1) and 3 Cl modes($\Gamma_2{}^-$ A_1, $\Gamma_2{}^-$ $A\prime_1$, $\Gamma_2{}^-$ $A\prime_2$) in a (1,0,0), (0,1,0), (0,0,1) basis. This is in addition to the movements allowed within the parent group $R\bar{3}m$ (not discussed further here).

To begin the mode decomposition analysis, the HT and LT structures were solved using single crystal XRD in $R\bar{3}m$ and $R3m$ respectively, and used as starting points for the PXRD refinements. The IT phase was solved in $R3m$ by Rietveld refinement of the $T =$ 179 K PXRD data using the pattern with the highest IT phase fraction (Table 4.3.2 and 4.3.3). Attempts to refine the IT structure with $R\bar{3}m$ and $R\bar{3}$ resulted in a visually and statistically less satisfactory refinement ($R\bar{3}m$ and $R\bar{3}$ have a $R_{wp} = 11.61$ vs. $R_{wp} = 11.50$

for $R3m$). Use of $R3$ reduced the number of equivalent positions from 18 to 9 and added an additional independent parameter but did not improve the fit relative to $R3m$. It is possible that the IT phase is an extended superstructure, as suggested by Hänni et al., but due to the imposed geometric constraints any trimerization will result in loss of inversion symmetry.[104] Therefore solving in $R3m$ is useful to quantify the net degree of activation of modes. These structures were then transformed into the local mode basis and each coefficient was allowed to vary in Rietveld refinements of all of the data sets (See 4.6).

The results of these refinements are shown in Figure 4.3.2(b). Two Ti ferroelectric modes are found to be active, Γ_2^- Bu_1 and Γ_2^- Bu_2. The Ti Γ_2^- Bu_1 mode results in trimerization of the kagomé lattice and the Ti Γ_2^- Bu_2 mode moves all the Ti atoms collectively down with respect to the Na atoms in the unit cell. Starting from the HT phase, cooling into the IT state results in activation of both of these modes with normalized amplitudes of +0.2 and -0.3 respectively. Further cooling into the LT state results in an increase of the mode amplitudes of +0.41 and -0.45 respectively. On warming, the LT mode amplitudes are maintained up to $T = 237$ K before falling to zero with the transformation to the HT phase. To confirm that the HT to IT phase transition is first order, a second cooling experiment that isolated the IT phase at $T = 179$ K was performed. On warming, the sample retained the IT mode amplitudes until the transition to the HT phase at $T = 220$ K.

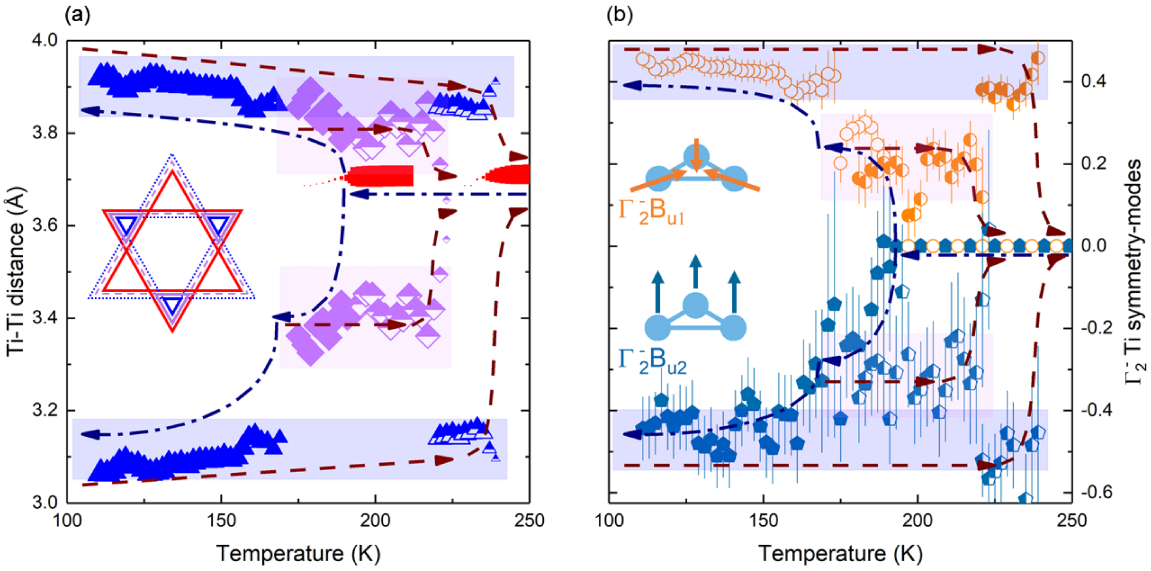

Figure 4.3.2: **a)** Ti-Ti interatomic distances as a function of temperature for the three phases, HT (red squares), IT (purple diamonds) and LT (blue triangles). The size of the marker corresponds to the phase fraction. **b)** Mode decomposition analysis of the ferroelectric Ti modes via powder X-ray Rietveld refinements of $Na_2Ti_3Cl_8$ measured upon cooling (royal blue dot dash arrow) and subsequent heating (dark red dash arrow) at a continuous rate of 1 K h^{-1}. Due to the continuous scanning method, scans near the transitions with large changes in phase fraction disrupted peak intensity consistency across a single phase resulting in increased symmetry-mode refinement errors. To account for this, only points with a phase fraction $> 25\%$ are shown and data points were averaged with its neighboring points to help stabilize data near large changes in phase fraction. At $T = 195$ K, two Ti modes, Γ_2^- B_{u1} (open orange circles) and Γ_2^- B_{u2} (teal pentagons) become active. The uniform markers were collected on heating and the half-filled markers on cooling. Purple and blue shading are used to highlight the occurrence of the IT and LT phase.

4.3.3 Physical Properties

The temperature-dependent ac magnetic susceptibility, χ, of polycrystalline powder $Na_2Ti_3Cl_8$ for both cooling and warming is shown in Figure 4.3.3(a). The LT phase maintains paramagnetic behavior down to $T = 2$ K. However, the response below $T = 100$ K is dominated by a Curie tail that likely originates from defects from the extreme air sensitivity of this material. Notably, the percent drop in susceptibility from HT $\rightarrow$ IT and

IT $\rightarrow$ LT with respect to HT $\rightarrow$ LT upon cooling is robust across all measured samples, indicative of intrinsic behavior. The average drop in χ from HT $\rightarrow$ IT and IT $\rightarrow$ LT is 37(2)% and 63(2)%, respectively, which is in agreement with previously reported values of 35.8% and 64.2%.[104, 105] This decrease in magnetic susceptibility is consistent with the electrons associated with the $S = 1$ moments on the Ti^{2+} kagomé sites delocalizing to form metal-metal bonds in the trimerized $[Ti_3]^{6+}$ clusters.

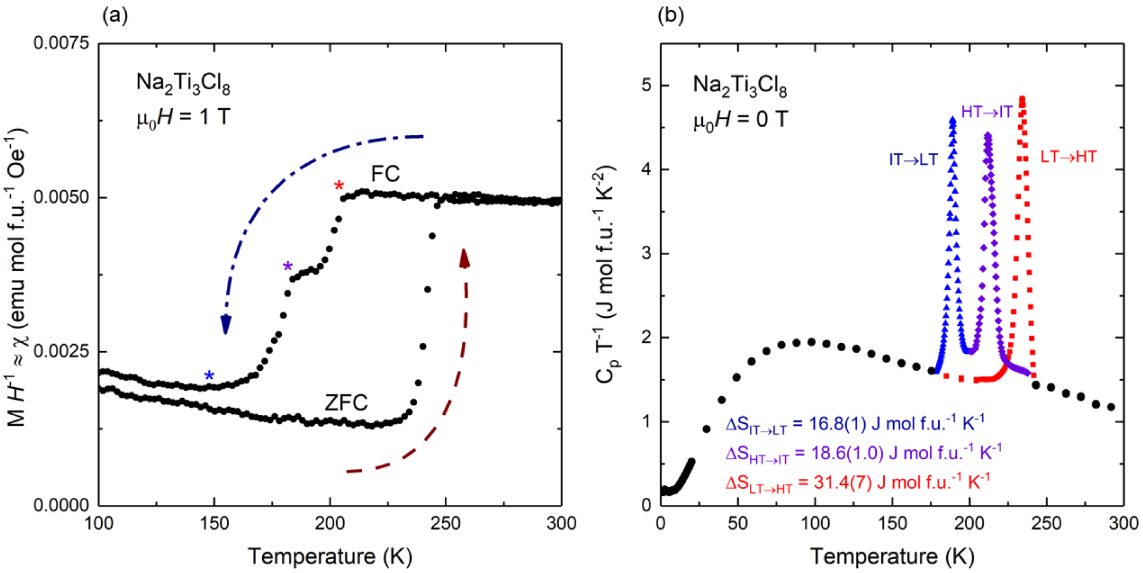

Figure 4.3.3: **a)** Magnetic susceptibility of $Na_2Ti_3Cl_8$ for zero field cooled upon warming (dark red dashed arrow) and field cooled upon cooling (royal blue dot dash arrow) under a 1 T applied field. **b)** Heat capacity over temperature versus temperature for NaTiCl collected using short pulse (black circles) and long pulse (red squares, purple diamonds, and blue triangles) techniques.

The heat capacity analysis of $Na_2Ti_3Cl_8$ is shown in Figure 4.3.3(b). The semi-adiabatic short pulse method was used to measure molar heat capacity from $T = 2$-300 K (black circles), but it was unable capture the large first order phase transitions. Therefore a long pulse experiment was used to characterize the phase transition upon heating and cooling.[106] The most representative fits from this analysis for each transition are included together in Figure 4.3.3(b) to give the overall heat capacity. The heat capacity of the transition is unaffected by magnetic fields up to $\mu_0 H = 9$ T.

The calculated change in entropy of all three transition are $\Delta S_{LT\rightarrow HT} = 31.4(7)$ J mol f.u.$^{-1}$ K^{-1}, $\Delta S_{HT\rightarrow IT} = 18.6(1.0)$ J mol f.u.$^{-1}$ K^{-1}, and $\Delta S_{IT\rightarrow LT} = 16.8(1)$ J mol f.u.$^{-1}$ K^{-1}. The sum of the entropy changes HT $\rightarrow$ IT and IT $\rightarrow$ LT is 35.4(1.2) J mol f.u.$^{-1}$ K^{-1} slightly larger than that estimated for the LT $\rightarrow$ HT transition. This is likely an artifact of the long pulses not capturing all of the entropy on warming. Regardless the total entropy change is larger than $3Rln(3) = 27.4$ J mol f.u.$^{-1}$ K^{-1} indicating loss of all magnetic degrees of freedom in addition to the entropy changes from the large structural transformations.

The specific heat below $T = 20$ K shows signatures of a T-linear contribution to the specific heat, unexpected as $Na_2Ti_3Cl_8$ is a dark forest green insulator indicating a band gap $\sim$ 1.7 eV (Figure 4.3.4). However, the extreme air sensitivity of the sample complicates further investigation as it is known that defects can induce T-linear terms in related materials.[107]

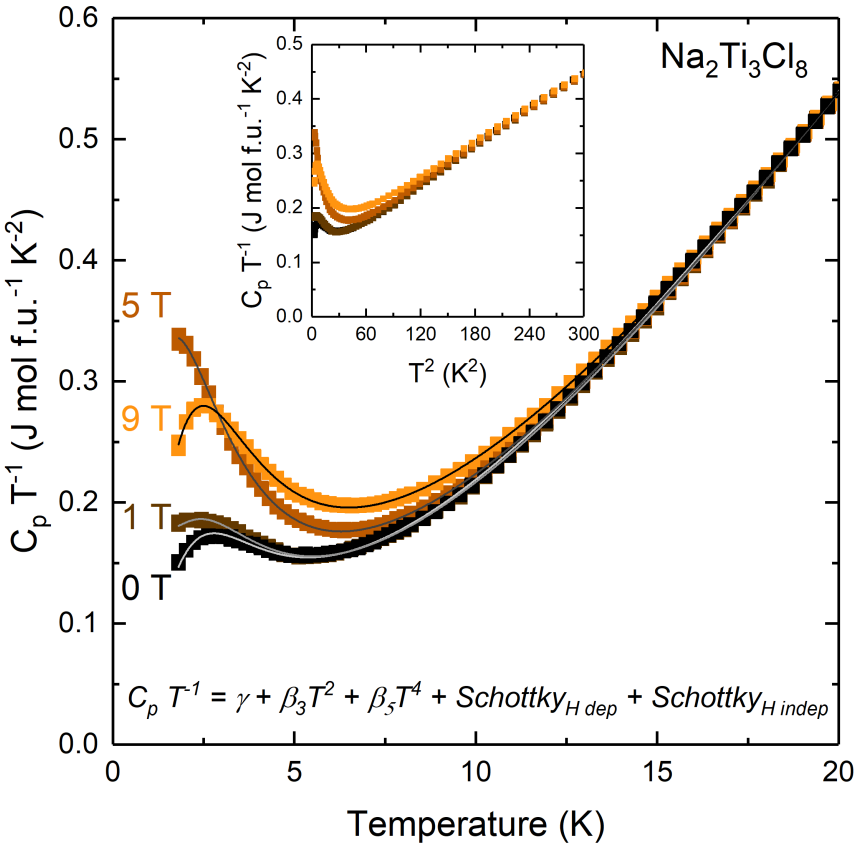

Figure 4.3.4: The field dependence of the low temperature heat capacity over temperature of $Na_2Ti_3Cl_8$. The inset shows C_p T^{-1} vs. T^2 to highlight the T-linear contribution to the heat capacity.

The short pulse field dependent heat capacity was analyzed using the following model:[**?**]

$$C_p = \gamma T + \beta_3 T^3 + \beta_5 T^5 + A_{Hindep} f(\Delta_{Hindep}, T) + A_{Hdep} f(\Delta_{Hdep}, T) \tag{4.1}$$

$$Af(\Delta, T) = AR(\Delta/T)^2 \frac{e^{\Delta/T}}{(1+e^{\Delta/T})^2} \tag{4.2}$$

Where the γT is the linear contribution, $\beta_3 T^3 + \beta_5 T^5$ are the phononic contributions, and $A_{Hindep} f(\Delta_{Hindep}, T)$ and $A_{Hdep} f(\Delta_{Hdep}, T)$ are Schottky anomalies term to describe field independent (H indep) and dependent (H dep) features at low temperatures.1 At $\mu_0 H = 0$ T, there is a feature at 2.7 K. The given the size of the peak and the extreme air-sensitivity

Table 4.3.4: Low temperature heat capacity fit parameters for $Na_2Ti_3Cl_8$. *The upper bound for A_{Hdep} was set to 0.15, which was hit by the refinement. Since the majority of the feature is at a temperature below the collected data, there is a number of possible solutions that would fit the field dependent component of the data.

Field (T)	0	1	5	9	Units
A_{Hindep}	0.0755(8)	0.0755	0.0755	0.0755	unitless
Δ_{Hindep}	8.45(3)	8.45	8.45	8.45	K
γ	0.0725(7)	0.0732(3)	0.0787(3)	0.0956(4)	J mol f.u.$^{-1}$ K^{-2}
β_3	0.00144(1)	0.00140(1)	0.00137(1)	0.00131(1)	J mol f.u.$^{-1}$ K^{-4}
β_5	-6.9(1)E-07	-5.91(8)E-07	-5.72(8)E-07	-5.09(9)E-07	J mol f.u.$^{-1}$ K^{-6}
A_{Hdep}	0	0.15(20)*	0.0913(2)	0.0615(4)	unitless
Δ_{Hdep}	0	0.8(6)	4.62(2)	7.30(2)	K
gJ	N/A	0.408	0.463	0.406	unitless

of $Na_2Ti_3Cl_8$, this peak could be due to orphan spins from defects or surface states created by slight decomposition of the sample. Application of a 1 T field does not appear to shift the peak at 2.7 K but an additional low temperature component can be seen growing in that is likely from Zeeman splitting of free spins. As the field increases to 5 T and 9 T, the field dependent feature becomes prominent and is well described by $A_{Hdep}f(\Delta_{Hdep},T)$. To determine if this is Zeeman splitting from the remnant magnetism of the $Na_2Ti_3Cl_8$ LT Phase, it was calculated by $\Delta_{Zeeman} = 2gJ\mu_B H$.

the low temperature heat capacity has a large T-linear contribution, $\gamma = 72$ mJ mol f.u.$^{-1}$ K^{-2}, typically attributed to the electronic contribution. In a related magnetic compound, $S_{eff} = \frac{1}{2}$ cluster magnet Nb_3Cl_8, a significant T-linear contribution of $\gamma = 13$ and 18 mJ mol f.u.$^{-1}$ K^{-2}, across two different single crystals is also found despite being an insulator.[107] They observe significant sample dependence, suggesting this contribution comes from defects rather than the bulk. The fivefold difference in γ between these compounds could be due to greater concentration defects in the polycrystalline $Na_2Ti_3Cl_8$ pellet as compared to Nb_3Cl_8 single crystals. This is consistent the magnetization data where it is clear that defects and surface states play a significant role in magnetic properties. Another consideration is the impact of integer spin vs. half integer spin. In 1D antiferromagnetic chains, the Haldane state in $S = 1$ systems contributes a large T-linear specific heat from these spin

edge states, considerably more compared to their $S_{eff} = \frac{1}{2}$ spin liquid counterparts.[108]

4.4 Discussion

There are many interesting questions raised by our results: how can the IT be stabilized on cooling but not on warming? How does this trimerization induce a ferroelectric state? What is the balance of electronic interactions that drives the trimerization? Are any of the phases observed related to the theoretical hexagonal singlet state?

The features of the observed hysteresis for both the IT and LT phases provides insight for the potential energy surface of the phase transitions. This energy surface can be described by a set of harmonic potential wells with the functional form $\frac{1}{2}kx^2$, where k is the bond force constant and x is the atomic displacement. The bond force constant is directly proportional to the Ti-Ti bond length, so as Ti-Ti distance decreases from HT $\rightarrow$ IT $\rightarrow$ LT, the width of the potential well will also decrease. This accounts for the asymmetry of the hysteresis, since narrow free energy potential of the LT phase will create a sufficiently large energy barrier to stabilize the IT phase on cooling while also trapping the LT phase on warming. As the system cools, the IT and LT wells will lower in energy relative to the HT phase. Using these general principles, a simple potential energy scheme was constructed that captures the overall features of the phase transitions in $Na_2Ti_3Cl_8$ (Figure 4.4.1). More theory is needed to understand the ground states of all three of these phases and their relation to the predicted hexagonal singlet and 2D valence bond solid states.

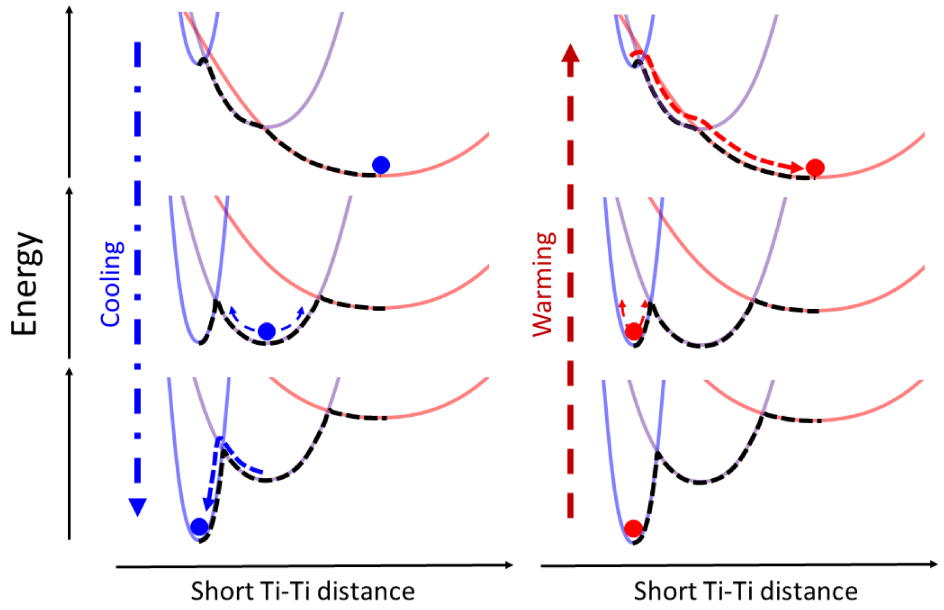

Figure 4.4.1: A schematic representation of the potential energy surfaces for the HT, IT, and LT states as a function of short Ti-Ti metal distance. The left panel shows the most likely path of the transition (blue ball) upon cooling while the right panel is upon warming (red ball).

One key feature of the observed trimerized states is that they are ferroelectric. This arises from a combination of two factors. First, each kagomé layer has apical Cl atoms alternating above and below the Ti layer. In the nonpolar HT phase, all kagomé triangles are equivalent and consequently all apical Cl atoms are equidistant from the kagomé plane. Upon trimerization, smaller and larger triangles are formed within the kagomé layer. This drives all of the apical Cl atoms on one side toward the kagomé plane and all of the Cl atoms on the other side away from the kagomé plane to maintain optimal Ti-Cl bond lengths. This spontaneously produces a ferroelectric polarization within one Ti_3Cl_8 layer and will be a general feature of trimerization of any kagomé network with alternating apical ligands. Whether or not the bulk material is ferroelectric then depends on the relative orientation of the polarization of successive layers. In the case of the Nb_3X_8 family of compounds, which contain trimerized kagomé lattices at all measured temperatures, orientation of adjacent layers results in either antiferroelectricity, as in α-Nb_3Cl_8 ($P\bar{3}m1$), or ferroelectricity, as in

Nb_3SeI_7 ($P6_3mc$).[109] In the case of $Na_2Ti_3Cl_8$ we find that adjacent layers polarize in the same direction producing a bulk ferroelectric.

This is a surprising result. To our knowledge, $Na_2Ti_3Cl_8$ is the first example of the collapse of magnetism and formation of metal-metal bonds driving a phase transition from an inversion symmetric to a proper ferroelectric state. All previously reported frustrated ferroelectric systems with large electronic correlations undergo improper mechanisms to break inversion symmetry. In many of these cases, the spontaneous polarization is driven not through structural changes, but through strong electron correlations on a geometrically frustrated lattice. For example, the charge-frustrated $LuFe_2O_4$ breaks symmetry by producing a charge density wave of Fe^{2+} and Fe^{3+} on a frustrated triangular lattice creating a net polar superstructure.[110] Its ferroelectric properties are strictly driven through charge disproportionation to create a mixed valence state. Other frustrated triangular ferroelectrics, such as $ACrO_2$ (A = Cu, Ag, Li or Na), $CuFeO_2$, $RMnO_3$ (R = Tb and Dy), $Ni_3V_2O_8$, $CoCr_2O_4$, $LiCu_2O_2$, and α-$NaFeO_2$, are driven by interacting spiral-spin states from complex magnetic order to achieve ferroelectricity.[99–102] The structurally related polar magnet $Fe_2Mo_3O_8$ displays giant magnetoelectricity originating from coupled atomic displacements and ferrimagnetic ordering of the interlayer iron atoms.[111]

By contrast, in the case of $Na_2Ti_3Cl_8$, it is the formation of metal-metal bonds to eliminate magnetic frustration that drives a major polar structural phase transition activating proper zone-center ferroelectric modes. Inversion symmetry-breaking mechanisms for proper ferroelectrics have only been reported in ABO_3 perovskite structures and are limited to either distortions through covalent bonding between the cation (d^0 transition metal) and anion (oxygen) or lone pair effects from heavy A site atoms such as Bi or Pb (Figure 4.4.2).[98]

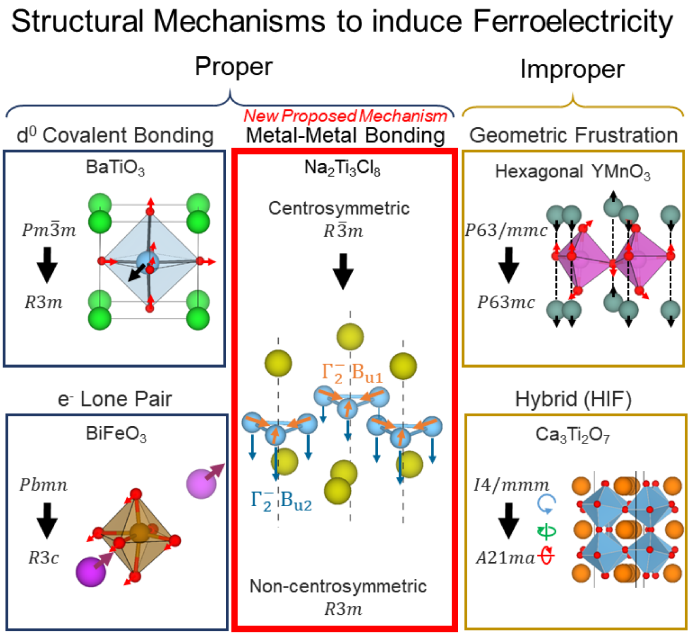

Figure 4.4.2: Structural inversion symmetry-breaking mechanisms for activation of ferroelectric modes.

4.5 Conclusion

In summary, $Na_2Ti_3Cl_8$ displays rich $S = 1$ kagomé physics, raising many questions about the fundamental physics of the kagomé lattice: What is the nature of the ground state in the IT phase and does it have a relation to the hexagonal singlet state? Is a specific defect or surface state is giving rise to the T-linear specific heat?

More concretely, our results demonstrate how quantum magnetism can be used to engineer and design novel ferroelectrics. The $Na_2Ti_3Cl_8$ metal-metal bonding mechanism opens the door to the discovery of fundamentally new classes of ferroelectrics. Related materials, such as Nb_3Cl_8 and molecular Fe_3 complexes, are already known to form metal-metal trimers while maintaining strong magnetic interactions.[107**?**] Using the design principles of strong magnetic frustration, highly correlated electrons, and metal-metal bonding, kagomé lattice materials could be the key to rationally designing the next generation of multifunctional quantum materials.

4.6 Methods

4.6.1 Materials synthesis

A forest green powder of $Na_2Ti_3Cl_8$ was synthesized by mixing a 2:3 molar ratio of dry NaCl and $TiCl_2$ (Sigma Aldrich 99.98%) powders in an evacuated quartz tube and heated at 450 C for 48 h. Pure powder samples were quenched in air while small crystal samples were grown on the quartz tube via self-vapor transport by slow cooling. Attempts to make $Na_2Ti_3Cl_8$ with starting materials as a pressed pellet yielded significant amounts of the off stoichiometric impurities suggesting the synthesis is mediated primarily through the gas phase. All reagents were handled with stringent air-free techniques due to extreme air and moisture sensitivity.

4.6.2 Characterization

All laboratory low-temperature XRD data was collected on a Bruker D8 Advance powder diffractometer with CuK radiation (λ = 1.5424 $\AA$), a scintillator point detector with 0.6 mm slits, and an Oxford Cryosystems PheniX low-temperature closed cycle cryostat. PXRD patterns were collected every 2 K while continuously cooling, $T =$ 210-130 K, and warming, $T =$ 220-260 K, at a rate of 1 K h^{-1}. A second set of patterns was collected where the sample was cooled for a second time to $T =$ 180 K from $T =$ 300 K to obtain the IT phase then continuously warmed at the same rate. Commercial Bruker Topas software, VESTA/citeMomma and ISODISTORT[55] were used to perform the mode decomposition analysis and Rietveld refinements. ISODISTORT was used to convert the atomic positions to symmetry modes in the IT and LT structure files for refinement. In both the PXRD cooling and warming series, each scan was systematically analyzed by Rietveld refinement. The subsequent refinement used the previous fit as its starting point. Both the IT and LT phases were constrained to the HT atomic positions, allowing the scale, lattice parameters, particle size, strain, and symmetry-modes to refine freely. Na Γ_2^- A_1 was fixed at

zero for all scans to serve as a reference point for the remaining modes. All instrumental parameters, preferred orientation, and sample roughness were fixed across all scans.

The single crystal XRD data was collected at $T = 110$ K and 220 K on a SuperNova diffractometer equipped with an Atlas detector using graphite-monochromated Mo Kα radiation ($\lambda = 0.71073$ Å) with the program CrysAlisPro (Version 1.171.36.32 Agilent Technologies, 2013). This program was also used to refine the cell dimensions and for data reduction. The temperature was controlled using the system Oxford Instruments Cryojet .The structure was solved with the program SHELXS-2014/7 and was refined on F2 with SHELXL-2014/7.[113]

Magnetization and specific heat data were collect on a Quantum Design Physical Properties Measurement System (PPMS). The heat capacity sample was a cold pressed pellet of polycrystalline powder. The semi-adiabatic pulse technique and dual slope analysis method was used for the short pulse data from $T = 2$ 300 K. Long pulse measurements were collected every 5 K from $T =$ 155-210 K and analyzed via LongHCPulse [106] software, a multi-point single slope method. The pulses with the most complete peaks were integrated to calculate the entropy of each transition.

4.7 Work in Progress and Future Outlook

4.7.1 Measuring the Dielectric Constant

With regards to terminology, "ferroelectricity" can refer to different things in the literature. In this manuscript, the term ferroelectric refers to a material which undergoes a spontaneous macroscopic polarization (becomes polar) through a inversion symmetry breaking distortion. Ferroelectrics can be further sub-divided into two categories: a) materials that may *in principle* be switched to a symmetry-equivalent state (switch polarization) by the application of an electric field or b) materials where polarization switching has been experimentally demonstrated.[114, 115] This ability is the property that gives ferroelectrics their

functionality for memory and electronic applications.

The most common method to test for polarization switching is to observe it directly using a Sawyer-Tower circuit as shown in Figure 4.7.1 **a**.[116, 117] The ferroelectric material is placed inside a capacitor and an alternating voltage is applied to generate a polarization vs. electric field measurement (Figure 4.7.1 **b**). This method requires cm-size single crystals and a circuit that can carry very high voltages (1-10^6 V). Due to several factors (the extreme air-sensitivity of $Na_2Ti_3Cl_8$, the challenges of obtaining cm-size single crystals, and the voltage restrictions on the PPMS circuitry) this measurement can not be practically performed on this material.

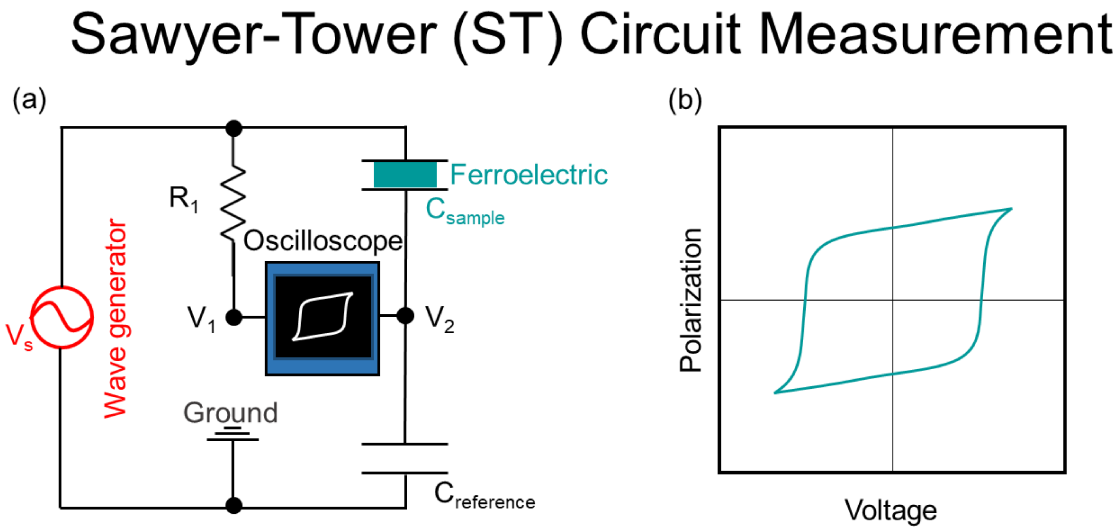

Figure 4.7.1: **a)** The Sawyer-Tower (ST) circuit most typically used for measuring polarization switching in ferroelectrics. **b)** A schematic representation of the hallmark polarization-voltage (P-V) hysteresis loop observed in ferroelectrics by this method.

Although the P-V loop can not be observed directly, the dielectric constant, ε, can be extracted through an impedance measurement of the sample in a resistor-capacitor (RC) circuit (Figure 4.7.2 **a**) When a ferroelectric material undergoes a ferroelectric-paraelectric phase transition, it displays a large increase in its dielectric constant as show in Figure

4.7.2 **b**.[116, 117] This circuit is sensitive to changes in dielectric constant when operating at low voltages (1-3 V), allowing it to be integrated into the PPMS circuitry which allows the $Na_2Ti_3Cl_8$ sample to be measured in a temperature controlled **inert** atmosphere. It is also conducive for powder samples, so large single crystals are not required.

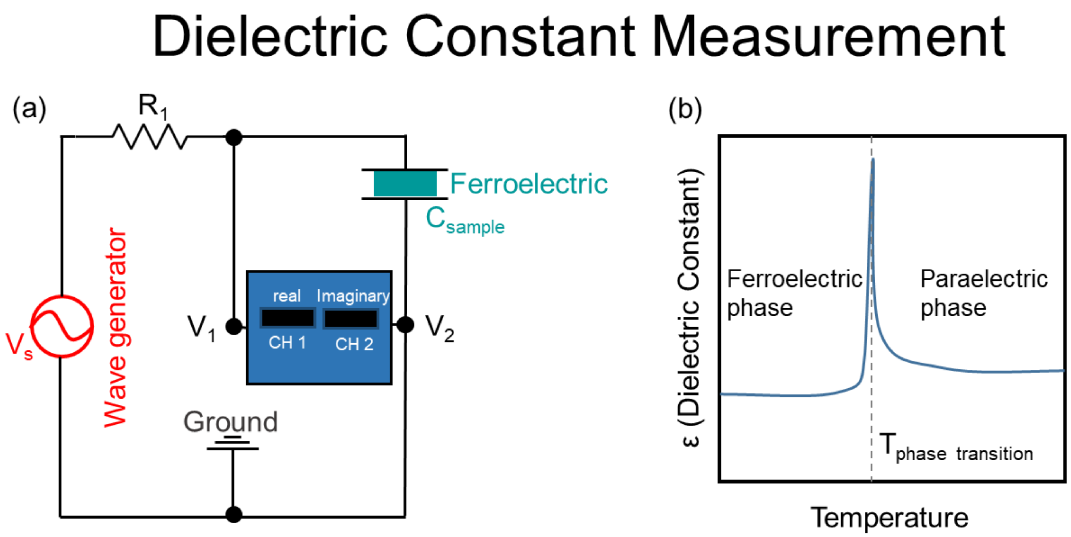

Figure 4.7.2: **a)** a resistor-capacitor (RC) circuit constructed to measure the change in dielectric constant of $Na_2Ti_3Cl_8$ as a function of temperature. **b)** A schematic representation of the expected dielectric constant anomaly as a material goes through a ferroelectric phase transition.

The impedance of a circuit is the vector sum of the reactance and resistance. It describes the phase difference and the ratio of the amplitudes between sin-varying voltage and sin-varying current at a given frequency. For an RC circuit, the impedance is the sum of the resistor and capacitor resulting in the following equations:

$$Z = R + \frac{1}{i\omega C} \tag{4.3}$$

$$|Z| = \sqrt{R^2 + \frac{1}{(\omega C)^2}} \tag{4.4}$$

$$tan(\phi) = -\frac{1}{(\omega CR)} \tag{4.5}$$

$$Z = |Z|(cos(\phi) + isin(\phi) \tag{4.6}$$

where Z is the impedance, R is the resistance, i is the imaginary number, ω is the frequency, C is the capacitance, and ϕ is the phase. Equation 4.6 describes the impedance in terms of a real and imaginary component which can be directly measured in the circuit described in Figure 4.7.2 **a**. From these values, the capacitance of the sample can be calculated and the dielectric constant values can extracted by:

$$C = \varepsilon_r \varepsilon_0 \frac{A}{d} \tag{4.7}$$

where ε_r is the dielectric constant of the material, ε_0 is the permittivity of free space, A is area of the overlap of the parallel plates, and d is the distance between the plates.

Custom capacitor cells were designed and built using glass slides, copper foil, electrical tape, glass slides, and epoxy as shown in Figure 4.7.3. The electrical tape served as masks and plate spacers to help prevent the plates from shorting. Polycrystalline powder of $Na_2Ti_3Cl_8$ was placed in the cell and was sealed using epoxy in the glovebox. The capacitor cell was then connected to a PPMS resistivity insert in order to operate it inside the PPMS dewer. The dewar provides an inert atmosphere and variable temperature control.

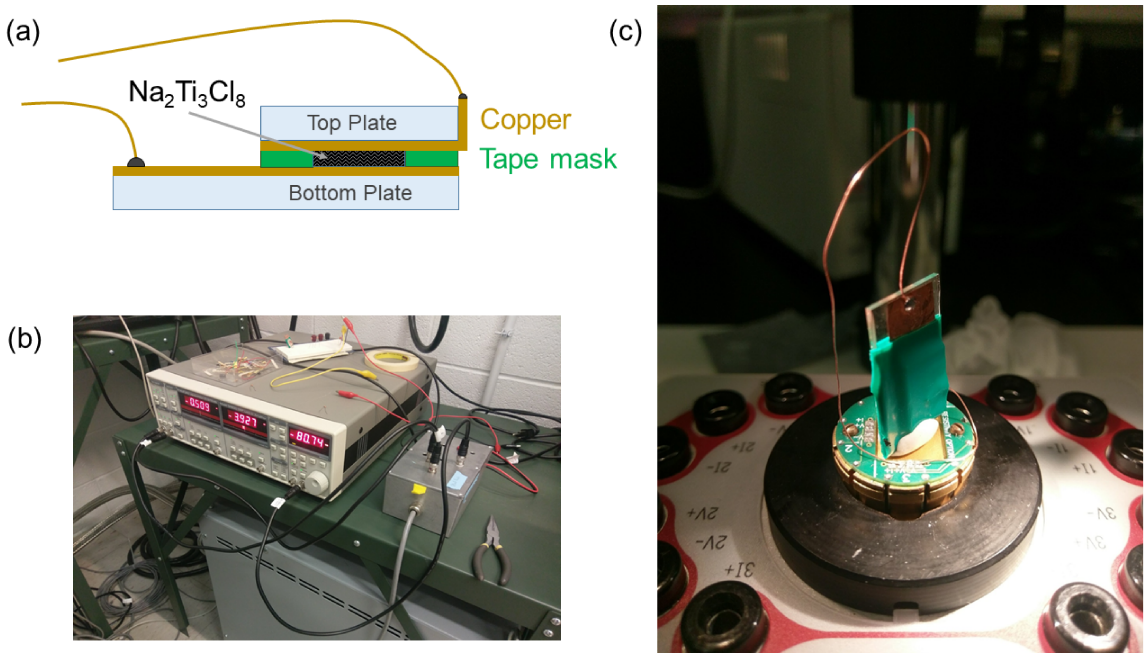

Figure 4.7.3: a) a schematic of the custom $Na_2Ti_3Cl_8$ capacitor. **b)** A photograph of the actual circuit (capacitor in the PPMS).**c)** A photograph of the constructed capacitor attached to a quantum design resistivity insert.

Several attempts were made to measure the dielectric constant of $Na_2Ti_3Cl_8$. The capacitance of the whole capacitor cells are $\sim$20 pF. With a resistor of a 5 MΩ, the circuit has been show to be sensitive to capacitance changes down to 1 pF. Temperature dependent studies on $Na_2Ti_3Cl_8$ are currently ongoing. The circuit still requires some adjustment to eliminate noise and shorting during changes in temperature. The next steps are to measure the empty capacitor cell, $Na_2Ti_3Cl_8$, and other known ferroelectrics which goes through a ferroelectric transition at $T <$ 300 K.

4.8 Acknowledgments

This work was supported by the NSF, Division of Materials Research (DMR), Solid State Chemistry (SSMC), CAREER grant under Award No. DMR- 1253562. T. M. M. was supported by the Institute for Quantum Matter, under Grant No.DE-FG02- 08ER46544. Z. A. K. would like to thank Allen Scheie for guidance with the HCLongPulse software and

M. Siegler for assistance with single crystal XRD data collection. Z. A. K. and T. M. M. thank H. Changlani and O. Tchernyshyov for useful discussions.

Author contributions: T. M. M. and Z. A. K designed the research. Z. A. K. synthesized the material and performed and all the analysis. T. T. T solved the structures using single crystal diffraction data. All authors contributed to the manuscript.

5 Utilizing Topochemical Reactions and High-Pressure Synthesis to Discover Novel Magnetic Honeycomb Iridates

5.1 Abstract

This work is the result of a collaboration with Prof. Hiroshi Kageyama at Kyoto University, Japan, supported by the National Science Foundation's East Asian and Pacific Summer Institutes (NSF EAPSI) fellowship. In the Kageyama lab, I explored both low temperature techniques and high pressure syntheses to target new quantum spin liquid materials with strong spin-orbit coupling. More specifically, the analytically solvable Kitaev model predicts the emergence of a unique type of quantum spin liquid state in the presence of anisotropic exchange arising from spin-orbit coupling. Both soft chemistry and high pressure techniques were attempted to modify the recently discovered iridium based honeycomb lattice, $Sr_3CaIr_2O_9$, to produce a material realization of the Kitaev spin liquid model. This honeycomb iridate contains all the structural components necessary for the Kitaev spin liquid model, and is unique due to its corner-sharing connectivity that will suppress the Heisenberg exchange terms that plague other honeycomb materials. In order to

satisfy the requirements of the model, Ir in $Sr_3CaIr_2O_9$ must be reduced from the $5d^4$ to the $5d^5$ electronic configuration while maintaining its honeycomb motif. Attempts to reduce $Sr_3CaIr_2O_9$ by various high-temperature ambient pressure strategies have failed, but reduction is potentially possible by analogy to closely related materials which have been successfully reduced.

5.2 Introduction

Soft chemistry is a powerful technique to alter the chemical composition and atomic structure of compounds to invoke exotic electronic and magnetic phenomena, such as a quantum spin-liquid (QSL) state. This quantum state has strongly interacting spins that are restricted by the lattice geometry so that a low energy ground state (perfect antiferromagnetic ordering of spins) cannot be satisfied.[40, 43] As a result, the spins remain disordered even at $T = 0$ K, and exhibit gapless excitations that could be harnessed to build quantum computers and spintronic devices. Theoretical models have predicted several potential QSL candidates containing specific structural motifs and magnetic properties; most notably perfect kagomé lattices and distorted honeycomb lattices.[118, 119] The overarching goal is to use innovative synthetic techniques to chemically alter these structural motifs in real compounds in search of emergent phenomena such as QSL behavior, and even superconductivity.[36]

One promising candidate that can be modified to potentially host exotic states is the honeycomb iridate $Sr_3CaIr_2O_9$.[48] While several iridates containing honeycomb connectivity have been reported, $Sr_3CaIr_2O_9$ is the only material in which the honeycomb lattice is formed by corner-sharing IrO_6 octahedra. This unique connectivity, combined with strong spin-orbit coupling, facilitates strongly anisotropic antiferromagnetic exchange between adjacent spins, which is a key requirement of the Kitaev model.[42] This type of Kitaev exchange is theoretically predicted (without numerical approximation) to produce a unique type of QSL. While previous attempts have gotten close to realizing this type of

QSL, there are no known examples.[47] The parent phase of $Sr_3CaIr_2O_9$ does not satisfy the desired electronic state of $J = 1/2$ on the octahedral iridium sites, instead the iridium is in the $5d^4$ electronic configuration yielding an electronic state of $J = 0$. However, by reducing Ir in $Sr_3CaIr_2O_9$ from the $5d^4$ to the $5d^5$ electronic configuration and maintaining the corner-sharing motif, it will satisfy all of the requirements of the Kitaev model. Hence, $Sr_3CaIr_2O_9$ is well suited to be reduced to produce the first example of a strong spin-orbit coupling iridate spin liquid.

Recently there has been significant progress of the applications and understanding of topochemical reduction using metal hydrides for transition metal oxides, most notably by the Kageyama group from Kyoto University, Japan.[59] They are at the forefront of the advancement of hydride reductions and high pressure reactions leveraging these techniques to create and characterize new and otherwise unattainable metastable phases. Hydride reductions have been applied broadly and successfully to perovskite family materials. Hydride reactions can reduce the metal center by either removing O to create vacancies or exchanging O^{2-} with H^+. This is demonstrated by recent reports of the synthesis and properties of $EuTiO_{3-x}H_x$ and (Ca,Sr,Ba)$TiO_{3-x}H_x$, using low-temperature CaH_2 reduction.[120, 121] The Kageyama group has also shown that CaH_2 can be utilized in a labile hydride strategy to synthesize heavily nitridized BaTiO3.[122]

Given the success of metal hydride reduction and high pressure synthesis in the perovskite family, $Sr_3CaIr_2O_9$, a perovskite, is particularly well-suited for studies implementing soft chemistry. Further precedent for the possible success of this reaction could be found with the compound $Sr_3CaRu_2O_9$, which shares the same 2:1 ordered perovskite structure as $Sr_3CaIr_2O_9$. $Sr_3CaRu_2O_9$ can be readily converted to $Sr_3CaRu_2O_8$ by treatment in 1 atm flowing argon for 24 h at 1200 °C and back to $Sr_3CaRu_2O_9$ by flowing 1 atm oxygen at 1000 °C for 24 h, demonstrating the reversible conversion of Ru^{4+} to Ru^{3+} while preserving the underlying connectivity.[123] This particular method has not been successful with reducing $Sr_3CaIr_2O_9$, however it does demonstrate that it is possible for

this structure type to be reduced.

The goal of this project is to design a novel class of spin liquid material with strong spin orbit coupling by preparing a reduced form of $Sr_3CaIr_2O_9$ that should exhibit quantum spin liquid behavior consistent with the Kitaev model. This was attempted by two approaches:

Approach 1: Use a series of metal hydrides under different reaction conditions to convert the parent honeycomb iridate, $Sr_3CaIr_2O_9$, to a reduced $Sr_3CaIr_2O_{9-x}H_z$ derivative.

Approach 2: Use high-pressure synthesis to prepare a reduced form of $Sr_3CaIr_2O_9$ through cation substitution of Sr with La or Ca with Y to yield $La_xSr_{3-x}CaIr_2O_9$ or $Sr_3(Ca_{1-x}Y_x)Ir_2O_9$ respectively.

5.3 Results and Discussion

5.3.1 Approach 1: Ambient Pressure, Low-Temperature Hydride Reduction

The metal hydride reductions were performed with three metal hydrides, NaH, LiH, and CaH_2, to attempt to reduce the $Sr_3CaIr_2O_9$. Polycrystalline $Sr_3CaIr_2O_9$ and metal hydride where mixed and ground throughly in a mortar and pestle in a glove box, pelletized, and sealed in a evacuated Pyrex tube. The sealed tubes were then heated for 2-7 days at different temperatures shown in Table 5.3.1. After reacting, the samples were crushed, added to 1 M NH_3Cl in methanol, and stirred for 1 h to remove any unreacted hydride and soluble byproducts. The samples were then filtered, washed with methanol, and dried in a desiccator.

Table 5.3.1: Low-temperature metal hydride reduction of $Sr_3CaIr_2O_9$ at ambient pressures.

Reducing agent	Molar Ratio Parent:MH_x	Temperature °C	Duration h	Results
CaH_2	1:2	300	46	reduced to Ir metal
CaH_2	1:2	350	65	reduced to Ir metal
CaH_2	1:2	400	43	reduced to Ir metal
LiH	1:2	300	46	No change in lattice parameters
LiH	1:2	400	43	reduced to Ir metal and $Ca(Sr_2Ca)IrO_6$
NaH	1:2	170	114	No change in lattice parameters
NaH	1:2	200	65	No change in lattice parameters
NaH	1:2	225	114	No change in lattice parameters

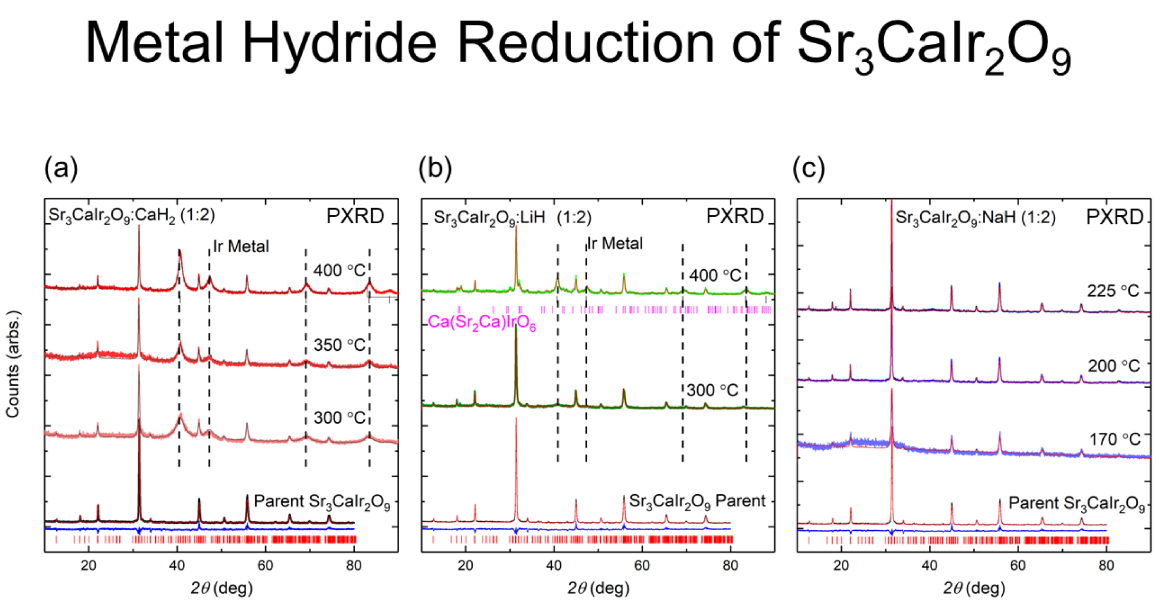

Figure 5.3.1: Laboratory powder x-ray diffraction (PXRD) patterns and Rietveld refinements for $Sr_3CaIr_2O_9$ reduction by **a)** CaH_2 at 300, 350, and 400 °C (Data-red Fit-gray), **b)** LiH at 300 and 400 °C (Data-green Fit-red), and **c)** NaH at 170, 200, and 225 °C (Data-purple Fit-red). The starting material, $Sr_3CaIr_2O_9$, is shown on the bottom for comparison. Ir metal is denoted by black dashed lines and the impurity phase, $Ca(Sr_2Ca)IrO_6$, is denoted by magenta tick marks.

The powder x-ray diffraction (PXRD) patterns of the metal hydride reduction reactions are shown in Figure 5.3.1. If $Sr_3CaIr_2O_9$ reacted to form $Sr_3CaIr_2O_{9-x}H_z$, it would be expected to show systematic changes in the lattice parameters of the unit cell (in $P2_1/c$).

All the CaH_2 reactions reduced the compound to Ir metal (Figure 5.3.1 **a**). The remaining material maintained the parent structure and did not have any detectable difference in lattice parameters from the parent which suggests that it is unreacted starting material. Similar results occurred for the LiH reactions at 400 °C, reducing $Sr_3CaIr_2O_9$ to Ir metal and forming a secondary phase of $Ca(Sr_2Ca)IrO_6$. The NaH reactions were performed at lower temperatures based on previous literature, and the reducing environment was mild enough to avoid making Ir metal. There were no significant changes in the lattice parameters, but there were some differences in relative peak intensities. The difference in intensity is a change in scattering intensity at a particular site which could be due to the removal of oxygen. To determine if the sample behaved differently DC-magnetization was performed (Figure 5.3.2).

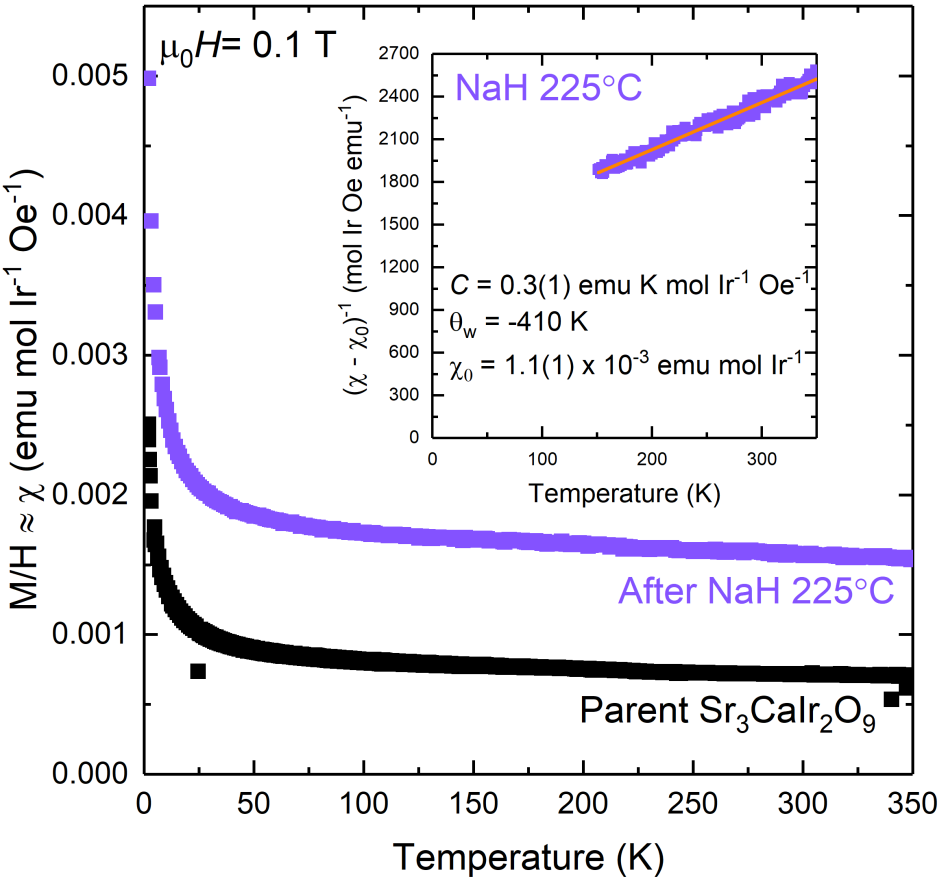

Figure 5.3.2: Magnetic susceptibility data collected on the parent $Sr_3CaIr_2O_9$ (black) and after a reaction with NaH at 225 °C (purple) are shown. All magnetic data were collected on polycrystalline samples by a squid magnetometer in direct current (DC) mode. The inset shows the χ_0-corrected inverse susceptibility.

There is a distinct difference between $Sr_3CaIr_2O_9$ before and after the reaction with NaH. Curie Weiss analysis of the reacted NaH 225 °C sample shows an increase in the temperature independent susceptibility ($\chi_0 = 1.1(1)$ x 10^{-3} emu mol), the Curie constant ($C = 0.3(1)$ emu K mol Ir^{-1} Oe^{-1}), and Weiss temperature (θ_w = -410 K). These results are promising given the parent's values were calculated to be $\chi_0 = 6.6(1)$ x 10^{-4} emu mol, $C = 0.17(1)$ emu K mol Ir^{-1} Oe^{-1}, and $\theta_w = 4$ K. The paramagnetic behavior with a large Weiss temperature is expected for a magnetically frustrated system. However more experiments are need to make sure that the magnetic response is due to the bulk sample and

repeatable and not due to some side product or contamination.

5.3.2 Approach 2: High Pressure synthesis

High pressure reactions, explained in detail in section 2.1.3, can dramatically shift the equilibrium by applying large pressures to access unexplored regions of the phase diagram. This method is attempted to replace elements in the $Sr_3CaIr_2O_9$ structure in order to make the compound magnetic while maintaining the honeycomb structure. Four compounds were targeted via high pressure synthesis: replacement of Sr with La to form $La_xSr_{3-x}CaIr_2O_9$ ($x = 1, 2$) and replacement of Ca with Y to form $Sr_3(Ca_{1-y}Y_y)Ir_2O_9$ ($y = 0.5, 1$). For ambient pressure (AP) reactions, stoichiometric amounts of $SrCO_3$, (La_2O_3 or Y_2O_3), $CaCO_3$ and IrO_2 were combined, ground and pelletized where high pressure reactions combined SrO, (La_2O_3 or Y_2O_3), CaO and IrO_2. $KClO_4$ was added as an oxygen source for the $La_1Sr_2CaIr_2O_9$ reactions. All sample pellets were wrapped in Pt foil, placed in standard HP cubic pressure transfer medium (Figure 2.1.1), and reacted a cubic anvil high-pressure apparatus. Table 5.3.2 records the pressure (0-7 GPa), temperature (1050-1500C) and duration of all the reactions.

Sr cation replacement with La: $La_xSr_{3-x}CaIr_2O_9$ ($x = 1, 2$)

Ambient pressure reactions targeting $La_2Sr_1CaIr_2O_9$ were attempted to serve as a comparison to the high pressure reactions. The resulting product assumed an off-target $P2_1/n$ CaS_3IrO_6 structure type. In this structure, the Ir honeycomb framework is lost as the IrO_6 octahedra are disconnected and share no bridging oxygens for superexchange. The HP reactions (2 and 5 GPa) targeting $La_2Sr_1CaIr_2O_9$ at 1050 °C resulted in incomplete reactions returning mostly starting material. The temperature was increased to 1500 °C for the remaining experiments. The PXRD patterns for the 1500 °C $La_2Sr_1CaIr_2O_9$ target reactions are shown in Figure 5.3.3 **a**. The starting materials are absent and given the general pattern, a perovskite-like phase is present. There are several differences in the pattern compared to

Table 5.3.2: High Pressure substitution reactions targeting $La_xSr_{3-x}CaIr_2O_9$ ($x = 1$, 2) and $Sr_3(Ca_{1-y}Y_y)Ir_2O_9$ ($y = 0.5$, 1)

Target Formula	Target Ir ox. state	Pressure (GPa)	Temperature °C	Duration h
$La_2SrCaIr_2O_9$	4+	AP	1050	12
	4+	2	1050	0.5
	4+	2	1050	0.5
	4+	5	1050	0.5
	4+	3	1500	0.5
	4+	5	1500	0.5
	4+	7	1500	0.5
$LaSr_2CaIr_2O_9$	4.5+	AP	1050	12
	4.5+	3	1500	0.5
	4.5+	5	1500	0.5
	4.5+	7	1500	0.5
	4.5+	AP	1500	30
$Sr_3YIr_2O_9$	4+	3	1200	1
	4+	5	1500	1
	4+	7	1500	1
$Sr_3(Ca_{0.5}Y_{0.5})Ir_2O_9$	4.5+	7	1200	1
	4.5+	7	1500	1
	4.5+	5	1500	1

the parent. Peak splitting is seen in the resulting HP products compared to the single phase of $Sr_3CaIr_2O_9$ which is highlighted at $2\theta = 31.5$ in Figure 5.3.3 **b**. There were attempts to fit the HP samples to common perovskite phases: a single phase in $P2_1/c$ (The space group of parent structure), a single phase of higher symmetry P4/mbm (127), and two separate phases in $Pm\bar{3}m$. Fits to single phases were unsatisfactory as some observed peaks were not predicted in the fit. In the HP samples, the difference in the shape and broadness of the "split" peaks suggests the two peaks belong to different phases. The two phase refinement resulted in a better description of the structure, however the calculated pattern did not fully match the peak positions and intensities present in the collected pattern.

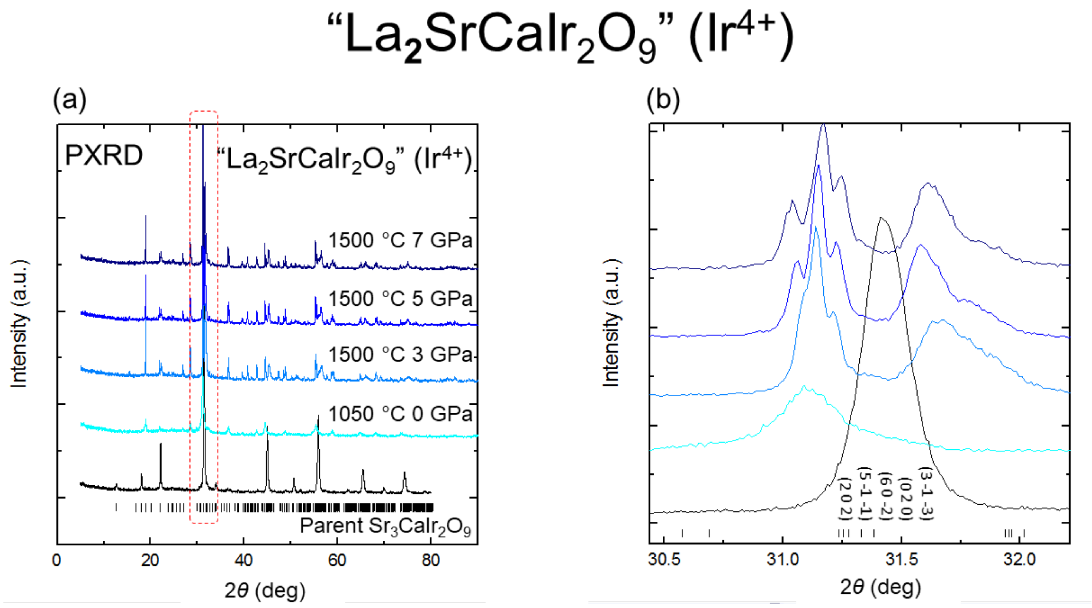

Figure 5.3.3: a) Laboratory powder x-ray diffraction (PXRD) patterns for HP targeted compound "$La_xSr_{3-x}CaIr_2O_9$" reacted at under four different conditions: 1500 °C at 7, 5, 3 GPa and 1050 °C at ambient pressure (AP). **b)** A zoomed view of the 31.2 2θ peak to illustrate the splitting of the target "$La_xSr_{3-x}CaIr_2O_9$" compounds. Given the difference in shape and broadness of the split peaks, it appears to be two separate phases. Attempts to fit the HP "$La_xSr_{3-x}CaIr_2O_9$" phases to a higher symmetry space groups resulted in a unsatisfactory fits.

Similar to $La_2Sr_1CaIr_2O_9$, $La_1Sr_2CaIr_2O_9$ also assumed the $P2_1/n$ CaS_3IrO_6 structure under ambient pressure. The HP synthesis targeting $La_1Sr_2CaIr_2O_9$ was run at 1500 °C

under 3, 5, and 7 GPa of pressure. The PXRD patterns for the HP samples, Figure 5.3.4, also appears to show multiple phases. These phases do not match any known structures in the ICSD database, and are likely new structures. However, having multiple unknown phases makes structure determination extremely complex. Ideally, synthesis would continue to be systematically optimized to isolate one or both of the phases. Once isolated, multiple independent techniques can be combined to solve the structure, such as simulated annealing coupled with unit cell determination by TEM. To see if these materials held any features of magnetic frustration, DC-magnetization was collected.

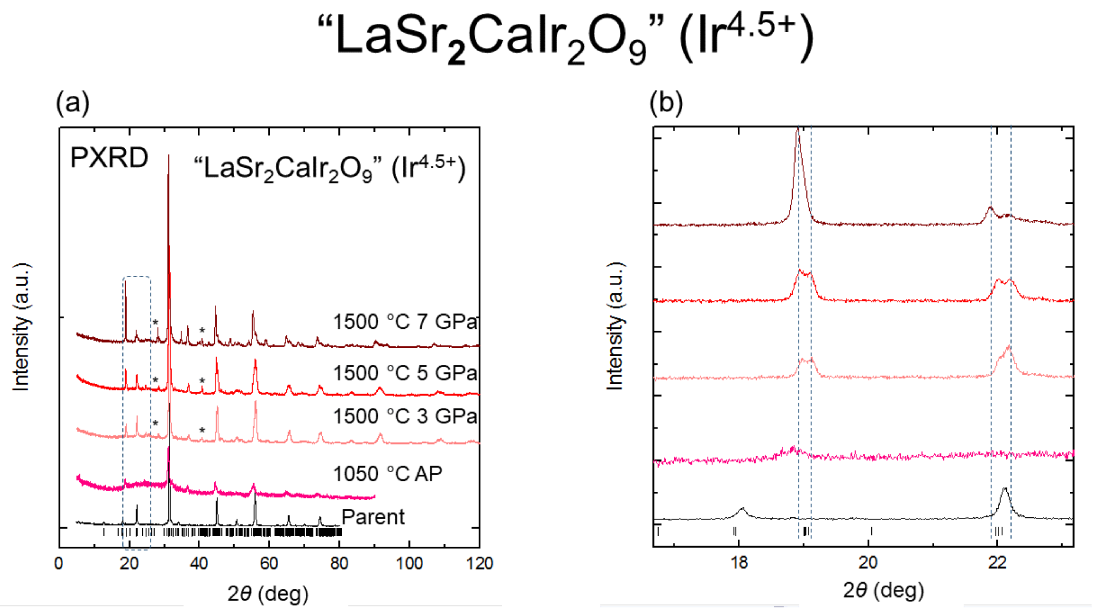

Figure 5.3.4: a) Laboratory powder x-ray diffraction (PXRD) patterns for HP targeted compound "$La_xSr_{3-x}CaIr_2O_9$" reacted at under four different conditions: 1500 °C at 7, 5, 3 GPa and 1050 °C at ambient pressure (AP). **b)** A zoomed view of the 31.2 2θ peak to illustrate the splitting of the target "$La_xSr_{3-x}CaIr_2O_9$" compounds. Given the difference in shape and broadness of the split peaks, it appears to be two separate phases. Attempts to fit the HP "$La_xSr_{3-x}CaIr_2O_9$" phases to a higher symmetry space groups resulted in unsatisfactory fits.

The magnetic susceptibility of resulting HP compounds targeting $LaSr_2CaIr_2O_9$ and $La_2SrCaIr_2O_9$ are shown in Figure 5.3.5. In the $LaSr_2CaIr_2O_9$ susceptibility data, there is a typical ferromagnetic response at low temperature seen during zero field cooled ex-

periments (ZFC). During the field cooled (FC) experiment, the susceptibility continually increases upon cooling, a known feature of ferromagnetic or spin glass ordering. At higher temperatures, the 3 GPa $LaSr_2CaIr_2O_9$ sample (Pink) and 7 GPa $La_2SrCaIr_2O_9$ (Blue) maintain a significant offset that can be distinguished from the temperature independent susceptibility. This is determined by the samples' low temperature ZFC response, which drops below the high temperature offset as shown in Figure 5.3.5 **b**. This feature demonstrates some sort of inherent field induced magnetic order that remains at high temperatures. Overall, all the samples display a smaller signal than what would be expected in a bulk ferromagnet. One possibility is that the ferromagnetic component is a minor phase, which is possible given the PXRD patterns. Another possibility is that the overall ferromagnetic response arises from the canting of an antiferromagnetic exchange. It is interesting to note that the 7 GPa $LaSr_2CaIr_2O_9$ (dark red) has the smallest response. This hints that the phase denoted by the green dotted line in Figure 5.3.4 **b** (shifted to higher angles in the diffraction data), which is more prevalent in the 3 and 5 GPa samples, could be responsible for the magnetic response (Figure 5.3.4). $La_2SrCaIr_2O_9$ has the largest ferromagnetic response under zero field cooled conditions.

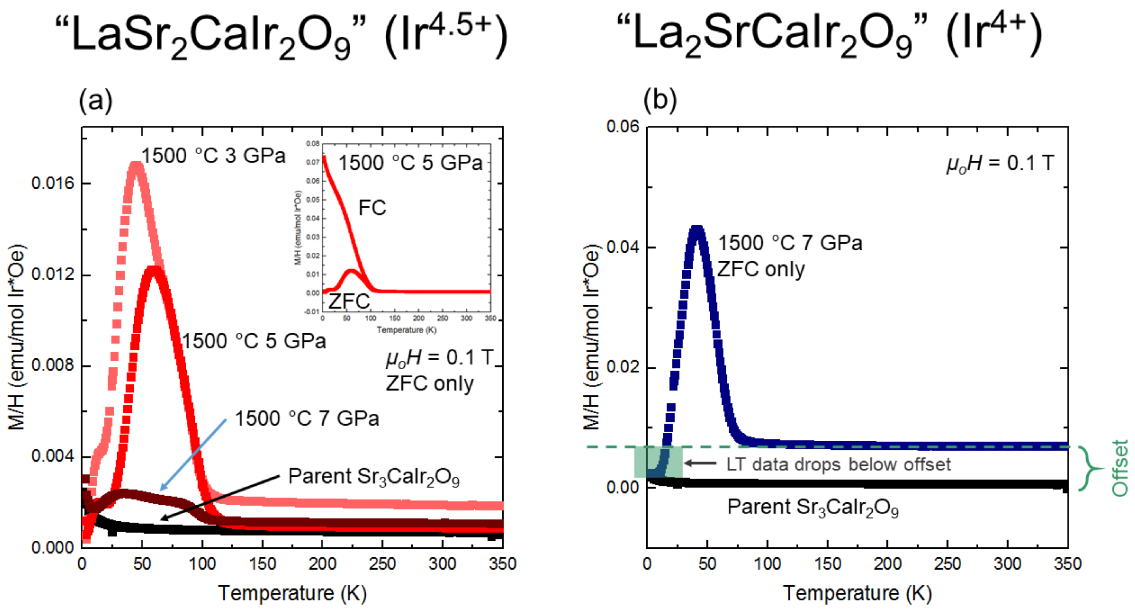

Figure 5.3.5: a) Magnetic susceptibility data collected on the parent $Sr_3CaIr_2O_9$ (black) and the HP "$LaSr_2CaIr_2O_9$" series (3, 5, and 7 GPa are light red, red, and dark red respectively) are shown. The inset shows the field cooled (FC) and zero field cool (ZFC) susceptibility. **b)** Magnetic susceptibility data collected on the parent $Sr_3CaIr_2O_9$ (black) and the 7 GPa 1500 °C "$La_2SrCaIr_2O_9$" sample are shown. All magnetic data were collected on polycrystalline samples by a squid magnetometer in direct current (DC) mode.

Ca cation replacement with Y: $Sr_3(Ca_{1-y}Y_y)Ir_2O_9$ ($y = 0.5, 1$)

The next set of experiments, laid out in the second half of Table 5.3.2, attempt to substitute Ca with Y. The 3 GPa $Sr_3Y_1Ir_2O_9$ resulted in the formation of $P2_1/n$ (14) Sr_2YIrO_6, a structure which is already reported. The PXRD patterns of the 5 and 7 GPa HP samples do not match previously reported structures making them more promising to be a novel material. Both of their patterns look similar but have different relative intensities for some sets of peaks. Also the 5 GPa pattern also having a few extra peaks which could be due to more impurity phases. The 7 GPa displays a nearly 2:1 peak intensity ratio for neighboring peak pairs. Also the peak shapes are much more consistent with one another. The 5 GPa sample has a different ratio of approximately 3:4 in a peak at 22 2θ and 4:3 in peaks ranging from 40-80 2θ. The variation in the intensity ratio between these two samples alludes to

the possibility of a secondary phase.

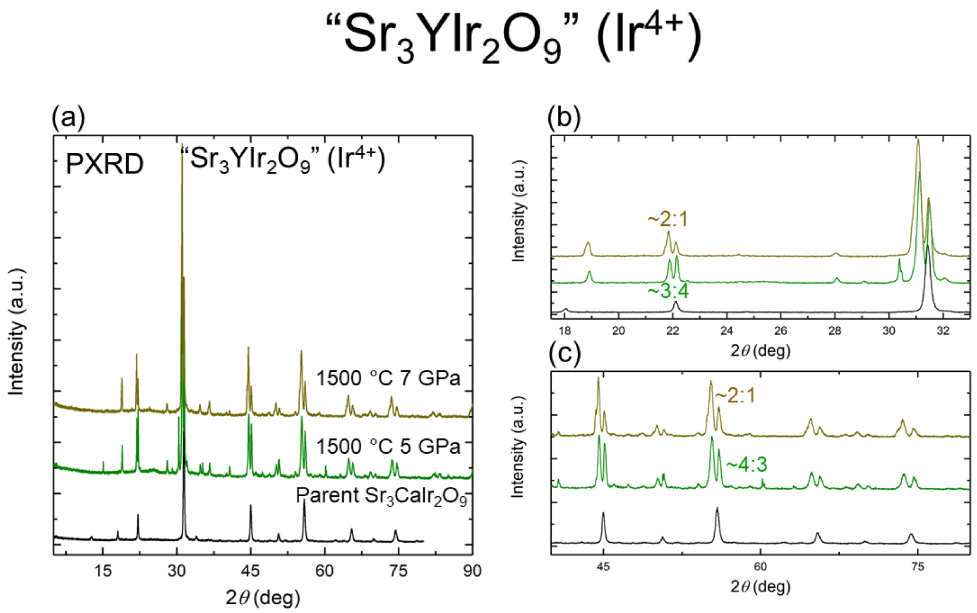

Figure 5.3.6: a) Laboratory powder x-ray diffraction (PXRD) patterns for HP targeted compound "$Sr_3YIr_2O_9$" reacted at under two different conditions: 1500 °C at 7 and 5 GPa. **b) c)** zoomed-in views ranging from 16-33 and 40-80 2θ peak to illustrate relative peak intensities and shapes.

The PXRD data for the half substituted target reactions at 7 GPa, $Sr_3Ca_{0.5}Y_{0.5}Ir_2O_9$, is shown in Figure 5.3.7. Even though both were run at 7 GPa, the lower temperature reaction at 1200 °C has sharper peaks than the 1500 °C reaction. Similar to the fully substituted $Sr_3YIr_2O_9$, $Sr_3Ca_{0.5}Y_{0.5}Ir_2O_9$ also has the features of a multiphase sample which are noticeable in the 31.5 2θ peak (Figure 5.3.7 **b**).

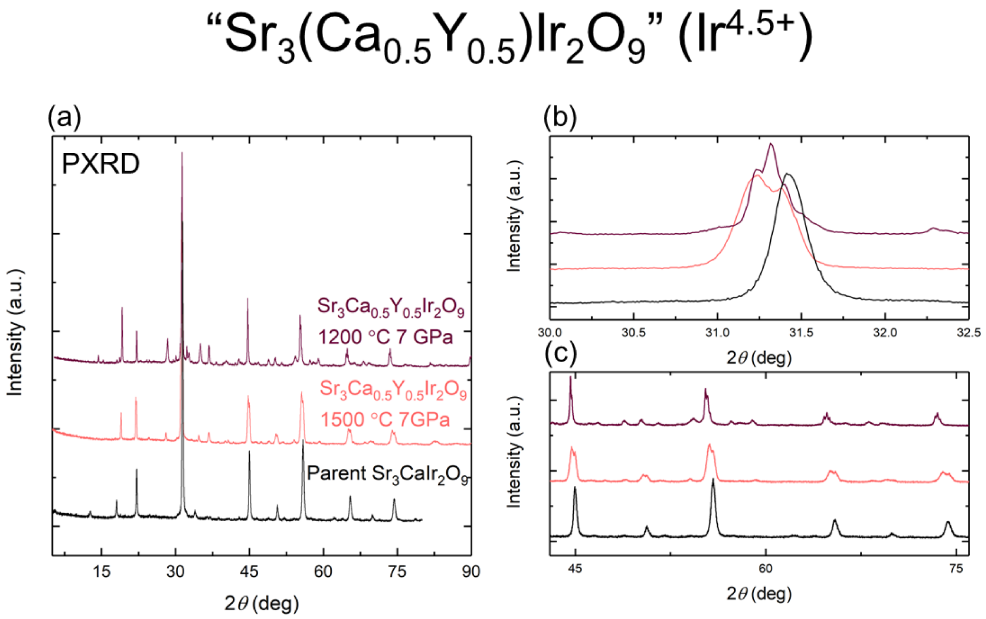

Figure 5.3.7: a) Laboratory powder x-ray diffraction (PXRD) patterns for HP targeted compound "$Sr_3Ca_{0.5}Y_{0.5}Ir_2O_9$" reacted at under two different conditions: 1500 °C at 7 GPa (rose)and 1200 °C at 7 GPa (purple). **b) c)** Zoomed-in views ranging from 30-32.5 and 42-78 2θ to illustrate relative peak intensities and shapes.

The magnetic susceptibility of the HP $Sr_3YIr_2O_9$ 7 GPa 1500 °C sample trends with the parent compound with overall paramagnetic response with a slight bit of hysteresis during field cooling (Figure 5.3.8 **a**). This could be from similar origins as we see in the $La_xSr_{3-x}CaIr_2O_9$ or it could be due to some type of spin glass behavior. All the HP $Sr_3Ca_{0.5}Y_{0.5}Ir_2O_9$ sample also show paramagnetic behavior. During the ZFC and FC measurements on the 7 GPa samples, a slight hysteresis is observed. The inverse susceptibility data deviates from normal Curie-Weiss behavior, making Curie-Weiss analysis uninformative. What can be inferred is the ferromagnetic contribution seen in the HP $La_xSr_{3-x}CaIr_2O_9$ samples is not significantly present in the Y substituted samples.

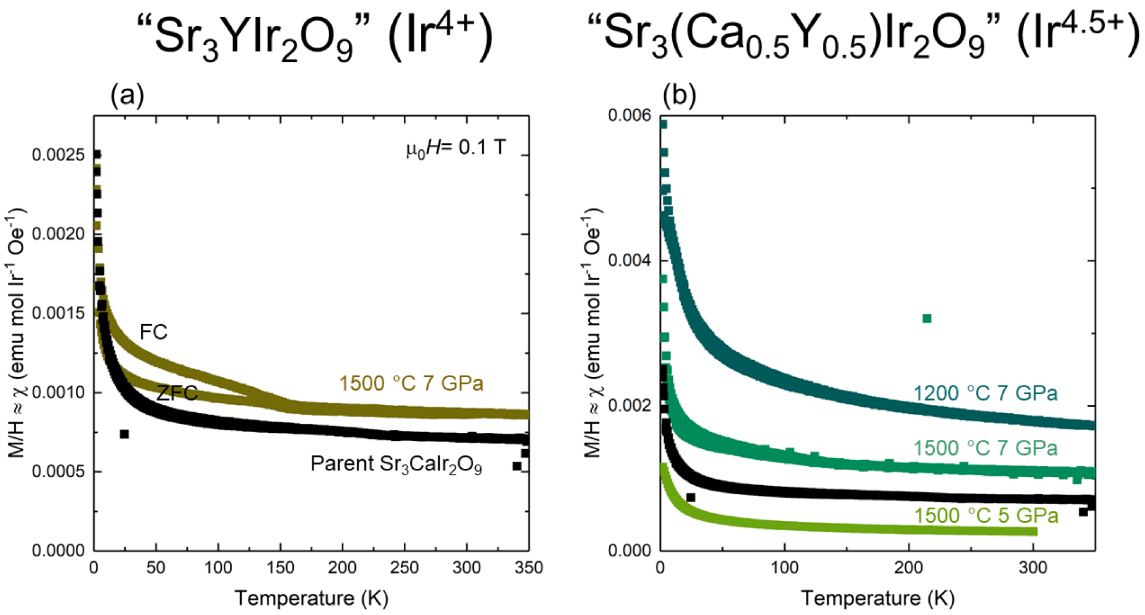

Figure 5.3.8: a)) Magnetic susceptibility of HP reactions targeting $Sr_3Y_1Ir_2O_9$ and **b)** HP reactions targeting $Sr_3Ca_{0.5}Y_{0.5}Ir_2O_9$. The parent is shown in black for reference. All magnetic data were collected on polycrystalline samples by a squid magnetometer in direct current (DC) mode.

5.4 Work in Progress and Future Outlook

These the high pressure reactions yielded new compounds which have not been previously reported. Work is continuing in order to elucidate the structure and measure the properties of these new materials, however the analysis is complex due to the multiple phases present in the samples. More experiments are needed to optimize reaction conditions to isolate each individual phase. With the phase pure samples, additional diffraction experiments could be performed to completely solve the structure. Currently, work is on going to determine any of these new materials contain the targeted magnetic Kitaev honeycomb lattice.

5.5 Acknowledgments

This work was supported by the NSF EAPSI fellowship. Z.A.K. would like to thank Kageyama Sensei for being a gracious host and for his chemical guidance. Z.A.K. deeply thanks Prof. Yamamoto and Prof. Tassel for useful discussions and all of Prof. Kageyama's graduate students for their training. Z.A.K. also thanks Prof. McQueen for his support and for allowing Z.A.K to pursue this opportunity.

Bibliography

[1] T. M. McQueen. Solid State Chemistry Course, 2013.

[2] M. Falk. Thermodynamics of Materials Course Notes, 2014.

[3] J. Bardeen, L. N. Cooper, and J. R. Schrieffer. Theory of superconductivity. Physical Review, **108**(5): 11751204, 1957. ISSN 0031899X. doi: 10.1103/PhysRev.108.1175.

[4] F. Zhang, Y. Wen, and X. Guo. CRISPR/Cas9 for genome editing: Progress, implications and challenges. Human Molecular Genetics, **23**(R1):4046, 2014. ISSN 14602083. doi:10.1093/hmg/ddu125.

[5] P. W. Anderson. More Is Different. Science, 177(4047):393396, 1972.

[6] N. W. Ashcroft and N.D. Mermin. Solid State Physics. Holt, Rinehart and Winston, 1976.

[7] A.R. West. Basic Solid State Chemistry. Wiley, 5 edition, 1984.

[8] I.N. Levine. Quantum Chemistry. Pearson Education, London, 6 edition, 2009.

[9] M. de Podesta. The band theory of solids. Michael de Podesta, 2002. ISBN 0-415-25788-3.

[10] J. B. Goodenough. Spin-Orbit-Coupling Effects in Transition-Metal Compounds. Physical Review, 171(2):466479, 1968.

[11] R. Hoffmann. How Chemistry and Physics Meet in the Solid State. pages 846878, 1987. doi:10.1002/anie.198708461.

[12] J. B. Goodenough. Magnetism and the Chemical Bond. In F. Albert Cotton, editor, Interscience Monographs on Chemistry. John Wiley & Sons, Ltd, 1963.

[13] M. P. Shores, B. M. Bartlett, and D. G Nocera. Spin-frustrated organic-inorganic hybrids of lindgrenite. Journal of the American Chemical Society, **127**(51):179867, 2005. ISSN 0002-7863.doi: 10.1021/ja056666g.

[14] J. H. de Boer and E. J. W. Verwey. Semi-conductors with partially and with completely filled 3d -lattice bands. Proceedings of the Physical Society, **49**(4S):5971, 1937. ISSN 0959-5309. doi: 10.1088/0959-5309/49/4S/307.

[15] J. Hubbard. Electron Correlations in Narrow Energy Bands. Proceedings of the Royal Society A: Mathematical, Physical and Engineering Sciences, 276(1365):238257, nov 1963. ISSN 1364-5021. doi: 10.1098/rspa.1963.0204.

[16] A. Yamada. Magnetic properties and Mott transition of the Hubbard model for weakly coupled chains on the anisotropic triangular lattice. Physical Review B - Condensed Matter and Materials Physics, 90(23):1618, 2014. ISSN 1550235X. doi: 10.1103/PhysRevB.90.235138.

[17] P.W. Anderson. The Resonating Valence Bond State in La 2 CuO 4 and Superconductivity. Science (New York, N.Y.), 235(4793):11961198, mar 1987. ISSN 0036-8075. doi: 10.1126/science.235.4793.1196.

[18] A P Cracknell. Crystals and their Structures. Pergamon Press, 1969. ISBN 0080138837.

[19] Z. A. Kelly, M. J. Gallagher, and T. M. McQueen. Electron Doping a kagomé Spin

Liquid. Physical Review X, 6(4):041007, 2016. ISSN 2160-3308. doi: 10.1103/PhysRevX.6.041007.

[20] R. E. Newnham. Properties of Materials. Oxford University Press, New York, 2005.

[21] R. DeHoff. Thermodynamics In Material Science. Taylor & Francis Group, New York, 2 edition, 2006. ISBN 9781420005851.

[22] G. H. Kwei, A. C. Lawson, S. J.L. Billinge, and S. W. Cheong. Structures of the ferroelectric phases of barium titanate. Journal of Physical Chemistry, 97(10):23682377, 1993. ISSN 00223654. doi: 10.1021/j100112a043.

[23] M. S. Dresselhaus. Solid State Physics - Part III Magnetic Properties of Solids. 2011. ISBN 9780444410849. doi: 10.1016/B978-0-444-41084-9.50005-9.

[24] S. Koide and T. Oguchi. Theories on the Magnetic Properties of Compounds. John Wiley & Sons. Inc., 5 edition, 1963.

[25] R. J. Baxter. Exactly Solved Models in Statistical Mechanics. Academic Press, 1982.

[26] A. Harrison. First catch your hare: The design and synthesis of frustrated magnets. Journal of Physics Condensed Matter, 16(11 SPEC. ISS.), 2004. ISSN 09538984.doi: 10.1088/0953-8984/16/11/001.

[27] S. G. Brush. History of the Lenz-Ising model. Reviews of Modern Physics, 39(4):883893, 1967. ISSN 00346861. doi: 10.1103/RevModPhys.39.883.

[28] M. Aizenman and B. Simon. A comparison of plane rotor and Ising models. Physics Letters A, 76(3-4):281282, 1980. ISSN 03759601. doi: 10.1016/0375-9601(80)90493-4.

[29] P. W. Anderson. Absence of diffusion in certain random lattices. Physical Review, 109(5):14921505, 1958. ISSN 0031899X. doi: 10.1103/PhysRev.109.1492.

[30] J. B. Goodenough. Theory of the role of covalence in the perovskite-type manganites [La,M(II)]MnO3. Physical Review, 100(2):564573, 1955. ISSN 0031899X. doi: 10.1103/Phys-Rev.100.564.

[31] J. Kanamori. Superexchange interaction and symmetry properties of electron orbitals. Journal of Physics and Chemistry of Solids, 10(2-3):8798, 1959. ISSN 00223697. doi: 10.1016/0022-3697(59)90061-7.

[32] K. Yosida. Magnetic properties of Cu-Mn alloys. Physical Review, 106(5):893898, 1957. ISSN0031899X. doi: 10.1103/PhysRev.106.893.

[33] B. Normand. Frontiers in frustrated magnetism. Contemporary Physics, 50(4):533552, 2009. ISSN00107514. doi: 10.1080/00107510902850361.

[34] A. P. Ramirez. Strongly Geometrically Frustrated Magnets. Annual Review of Materials Science, 24(1):453480, 1994. ISSN 0084-6600. doi: 10.1146/annurev.ms.24.080194.002321.

[35] R. Moessner and J. Chalker. Low-temperature properties of classical geometrically frustrated anti-ferromagnets. Physical Review B - Condensed Matter and Materials Physics, 58(18):1204912062, 1998. ISSN 1550235X. doi: 10.1103/PhysRevB.58.12049.

[36] L. Balents. Spin liquids in frustrated magnets. Nature, 464(7286):199208, 2010. ISSN 0028-0836.doi: 10.1038/nature08917.

[37] L. Savary and L. Balents. Quantum Spin Liquids. 2016.

[38] P. A. Lee. Quantum spin liquid: a tale of emergence from frustration. Journal of Physics: Conference Series, 529:012001, 2014. ISSN 1742-6588. doi: 10.1088/1742-6596/529/1/012001.

[39] T. Imai and Y. S. Lee. Do quantum spin liquids exist? Physics Today, 69(8):3036, 2016. ISSN 00319228. doi: 10.1063/PT.3.3266.

[40] P. A. Lee. Physics. An end to the drought of quantum spin liquids. Science (New York, N.Y.), 321 (2008):13061307, 2008. ISSN 0036-8075. doi: 10.1126/science.1163196.

[41] S. Yan, D. A. Huse, and S. R. White. Spin-Liquid Ground State of the S = 1/2 kagom Heisenberg Antiferromagnet. Science, **332**(6034):11731176, 2011. ISSN 0036-8075. doi: 10.1126/science.1201080.

[42] A. Kitaev. Anyons in an exactly solved model and beyond. Annals of Physics, **321** (1):2111, 2006. ISSN 00034916. doi: 10.1016/j.aop.2005.10.005.

[43] P.W. Anderson. Resonating valence bonds: A new kind of insulator? Materials Research Bulletin, **8**(2):153160, 1973. ISSN 00255408. doi: 10.1016/0025-5408(73)90167-0.

[44] M. Fu, T. Imai, T.-H. Han, and Y. S. Lee. Evidence for a gapped spin-liquid ground state in a kagomé Heisenberg antiferromagnet. Science (New York, N.Y.), 350 (6261):655658, 2015. ISSN 0036-8075. doi: 10.1126/science.aab2120.

[45] T. Han, J. S. Helton, S. Chu, D. G. Nocera, J. A. Rodriguez-Rivera, C. Broholm, and Y. S Lee. Fractionalized excitations in the spin-liquid state of a kagomé -lattice antiferromagnet. Nature, 492(7429):406410, 2012. ISSN 0028-0836. doi: 10.1038/nature11659.

[46] K. W. Plumb, et al. α-$RuCl_3$: A spin-orbit assisted Mott insulator on a honeycomb lattice. Physical Review B - Condensed Matter and Materials Physics, 90(4):15, 2014. ISSN 1550235X. doi: 10.1103/PhysRevB.90.041112.

[47] H. Kim, V. Shankar V., A. Catuneanu, and H. Y. Kee. Kitaev magnetism in honeycomb

$RuCl_3$ with intermediate spin-orbit coupling. Physical Review B, **91**(24):241110, 2015. ISSN 1098-0121. doi: 10.1103/PhysRevB.91.241110.

[48] D. C. Wallace and T. M. McQueen. New honeycomb iridium oxides: $NaIrO_3$ and $Sr_3CaIr_2O_9$. Dalton Trans., (1), 2015. ISSN 1477-9226. doi: 10.1039/C5DT03188E.

[49] H. J. Changlani and A. M. Luchli. Trimerized ground state of the spin-1 Heisenberg antiferromagnet on the kagomé lattice. Physical Review B - Condensed Matter and Materials Physics, 91 (10):26, 2015. ISSN 1550235X. doi: 10.1103/PhysRevB.91.100407.

[50] N. Wada, et al. Observation of Spin-Gap State in Two-Dimensional Spin-1 Kagomé Antiferromagnet m-MPYNN-BF 4. Journal of the Physics Society Japan, 66(4):961964, 1997. ISSN 0031-9015. doi: 10.1143/JPSJ.66.961.

[51] T. Matsushita, N. Hamaguchi, K. Shimizu, N. Wada, W. Fujita, K. Awaga, A. Yamaguchi, and H. Ishimoto. Quantum Spin State and Magnetization Plateaus in an S =1 Kagomé Heisenberg Antiferromagnet. Journal of the Physical Society of Japan, 79(9):093701, 2010. ISSN 0031-9015. doi: 10.1143/JPSJ.79.093701.

[52] A. Niazi, et al. Single-crystal growth, crystallography, magnetic susceptibility, heat capacity, and thermal expansion of the antiferromagnetic S=1 chain compound CaV_2O_4. Physical Review B - Condensed Matter and Materials Physics, **79** (10):121, 2009. ISSN 1550235X. doi: 10.1103/PhysRevB.79.104432.

[53] G. Jaeger. The Ehrenfest Classification of Phase Transitions: Introduction and Evolution. Archive for History of Exact Sciences, **53**(1):5181, 1998. ISSN 0003-9519. doi: 10.1007/s004070050021.

[54] J. Toledano and P. Toledano. Landua Theory Of Phase Transitions. World Scientific, Singapore, 1987. ISBN 9789971500252. doi:10.1142/9789812799395 0 005.

[55] B. J. Campbell, H. T. Stokes, D. E. Tanner, and D. M. Hatch. ISODISPLACE: A web-based tool for exploring structural distortions. Journal of Applied Crystallography, 39(4):607614, 2006. ISSN 00218898. doi: 10.1107/S0021889806014075.

[56] M. Hayward. Topochemical reactions of layered transition-metal oxides. Semiconductor Science and Technology, 29:064010, 2014. ISSN 0268-1242. doi: 10.1088/0268-1242/29/6/064010.

[57] R. Schollhorn. From Electronic / Ionic Conductors to Superconductors : Control of Materials Properties. Angew. Chem. Int. Ed. Engl., 27(10):13921400, 1988.

[58] C. Sanchez, L. Rozes, F. Ribot, C. Laberty-Robert, D. Grosso, C. Sassoye, C. Boissiere, and L. Nicole. Chimie douce: A land of opportunities for the designed construction of functional inorganic and hybrid organic-inorganic nanomaterials. Comptes Rendus Chimie, 13(1-2):339, 2010. ISSN 16310748. doi: 10.1016/j.crci.2009.06.001.

[59] T. Yamamoto and H. Kageyama. Hydride Reductions of Transition Metal Oxides. Chemistry Letters, 42(9):946953, 2013. ISSN 0366-7022. doi: 10.1246/cl.130581.

[60] N. G. Connelly and W. E. Geiger. Chemical Redox Agents for Organometallic Chemistry. Chemical reviews, 96(2):877910, 1996. ISSN 1520-6890. doi: 10.1021/cr940053x.

[61] Y. Kobayashi, et al. Gas phase contributions to topochemical hydride reduction reactions. Journal of Solid State Chemistry, 207:190193, 2013. ISSN 00224596. doi: 10.1016/j.jssc.2013.09.006.

[62] C. Tassel, Y. Goto, Y. Kuno, J. Hester, M. Green, Y. Kobayashi, and H. Kageyama. Direct synthesis of chromium perovskite oxyhydride with a high magnetic-transition temperature. Angewandte Chemie (International ed. in English), 53(39):1037780, 2014. ISSN 1521-3773. doi: 10.1002/anie.201405453.

[63] B. H. Toby. R factors in Rietveld analysis: How good is good enough? Powder Diffraction, 21 (2005):6770, 2006. ISSN 0885-7156. doi: 10.1154/1.2179804.

[64] A. Tari. The Specific Heat of Matter at Low Temperatures. Imperial College Press, London, 1 edition, 2003. ISBN 1860943144.

[65] Matthew P. Shores, Emily a. Nytko, Bart M. Bartlett, and Daniel G. Nocera. A structurally perfect S = 1/2 metal-organic hybrid kagomé antiferromagnet. Journal of the American Chemical Society, 127(39):13462 13463, 2005. ISSN 00027863. doi: 10.1021/ja709991u.

[66] D. E. Freedman, et al. Site specific X-ray anomalous dispersion of the geometrically frustrated kagomé magnet, Herbertsmithite, $ZnCu_3(OH)_6Cl_2$. Journal of theAmerican Chemical Society, 132(45):1618516190, 2010. ISSN 1520-5126. doi: 10.1021/ja1070398.

[67] Shaoyan Chu, Tyrel M. McQueen, Robin Chisnell, Danna E. Freedman, Peter Muller, Young S. Lee, and Daniel G. Nocera. A Cu^{2+} (S = 1/2) Kagomé Antiferromagnet: $Mg_xCu_{4x}(OH)_6Cl_2$. Journal of the American Chemical Society, 132(16):55705571, 2010. ISSN 0002-7863. doi: 10.1021/ja1008322.

[68] I. I. Mazin, et al. Theoretical prediction of a strongly correlated Dirac metal. Nature communications, 5(May):4261, 2014. ISSN 2041-1723. doi: 10.1038/ncomms5261.

[69] D. Guterding, H. O. Jeschke, and R. Valenti. Prospect of quantum anomalous Hall and quantum spin Hall effect in doped kagomé lattice Mott insulators. Scientific Reports, 6:25988, 2016. ISSN 2045-2322. doi: 10.1038/srep25988.

[70] M. A. Hayward, E. J. Cussen, J. B. Claridge, M. Bieringer, M. J. Rosseinsky, C. J. Kiely, S. J. Blundell, I. M. Marshall, and F. L. Pratt. The hydride anion in an extended transition metal oxide array: $LaSrCoO_3H_{0.7}$. Science (New York, N.Y.), 295(5561):18821884, 2002. ISSN 00368075. doi: 10.1126/science.1068321.

[71] Y. Tsujimoto, C. Tassel, N. Hayashi, T. Watanabe, H. Kageyama, K. Yoshimura, M. Takano, M. Ceretti, C. Ritter, and W. Paulus. Infinite-layer iron oxide with a square-planar coordination. Nature, 450(December):1062 1065, 2007. ISSN 0028-0836. doi: 10.1038/nature06382.

[72] M. J. Rosseinsky, et al. Structural and electronic properties of sodium-intercalated C 6 0. Nature, 356:416418, 1992. ISSN 0028-0836. doi: 10.1038/356416a0.

[73] J. R. Neilson, et al. Mixed-valence-driven heavy-fermion behavior and superconductivity in KNi_2Se_2. Physical Review B - Condensed Matter and Materials Physics, 86:112, 2012. ISSN 10980121. doi: 10.1103/PhysRevB.86.054512.

[74] B. Scott and R. Willett. Crystal structure and electronic spectroscopy of bis(hydrazinium) hexachlorotricuprate(2I,II): a copper(I)-copper(II) mixed-valence system exhibiting intervalence charge transfer. Inorganic Chemistry, 30(1):110113, 1991. ISSN 0020-1669. doi: 10.1021/ic00001a020.

[75] M. H. Braga, J. Ferreira, and L. F. Malheiros. A ternary phase in Cu-Li-Mg system. Journal of Alloys and Compounds, 436(1-2):278284, 2007. ISSN 09258388. doi: 10.1016/j.jallcom.2006.07.023.

[76] N. S. McIntyre and M. G. Cook. X-Ray Photoelectron Studies on Some Oxides and Hydroxides of Cobalt, Nickel, and Copper. Analytical Chemistry, 47(13):22082213, 1975.

[77] P. Van der Heide. X-ray Photoelectron Spectroscopy : An introduction to Principles and Practices. Wiley,2011. ISBN 9781118062531.

[78] M. B. Robin and P. Day. Mixed Valence Chemistry-A Survey and Classification. In Advances in Inorganic Chemistry and Radiochemistry, volume 10, pages 247422. 1967. ISBN 9780120236107. doi: 10.1016/S0065-2792(08)60179-X.

[79] P. Day, N. Hush, and R. Clark. Mixed valence: origins and developments. Philosophical transactions. Series A, Mathematical, physical, and engineering sciences, 366(1862):514, 2008. ISSN 1364-503X. doi: 10.1098/rsta.2007.2135.

[80] H. Rupp and U. Weser. X-ray photoelectron spectroscopy of copper(II), copper(I), and mixed valence systems. Bioinorganic Chemistry, 6(1):4559, 1976. ISSN 00063061. doi: 10.1016/S0006-3061(00)80049-6.

[81] C. D. Wagner. Auger lines in x-ray photoelectron spectrometry. Analytical Chemistry, 44(6):967973, 1972. ISSN 0003-2700. doi: 10.1021/ac60314a015.

[82] G. Panzner, B. Egert, and H.P. Schmidt. The stability of CuO and Cu_2O surfaces during argon sputtering studied by XPS and AES. Surface Science Letters, 151(2-3):A83, 1985. ISSN 01672584. doi: 10.1016/0167-2584(85)90649-8.

[83] R. Singh and D. Huse. Triplet and singlet excitations in the valence bond crystal phase of the kagomé lattice Heisenberg model. Physical Review B - Condensed Matter and Materials Physics, 77(14):17, 2008. ISSN 10980121. doi: 10.1103/PhysRevB.77.144415.

[84] J. P. Sheckelton, J. R. Neilson, and T. M. McQueen. Electronic tunability of the frustrated triangular-lattice cluster magnet $LiZn-2-xMo_3O_8$. Mater. Horiz., 2(1):7680, 2015. ISSN 2051-6347. doi: 10.1039/C4MH00166D.

[85] [85] Y. Kurosaki, Y. Shimizu, K. Miyagawa, K. Kanoda, and G. Saito. Mott Transition from a Spin Liquid to a Fermi Liquid in the Spin-Frustrated Organic Conductor $\kappa(ET)_2Cu_2(CN)_3$. Physical Review Letters, 95(17):177001, oct 2005. ISSN 0031-9007. doi: 10.1103/PhysRevLett.95.177001.

[86] M. Lee, et al. Large enhancement of the thermopower in Na_xCoO_2 at high Na doping. Nature materials, 5(7):537540, 2006. ISSN 1476-1122. doi: 10.1038/nmat1669.

[87] Y. Okamoto, et al. Spin-Liquid State in the S = 1/2 Hyperkagomé Antiferromagnet $Na_4Ir_3O_8$. Physical Review Letters, 99 (13):137207, 2007. ISSN 0031-9007. doi: 10.1103/PhysRevLett.99.137207.

[88] D. Podolsky and Y. B. Kim. Spin-orbit coupling in the metallic and spin-liquid phases of $Na_4Ir_3O_8$. Physical Review B, 83(5):054401, 2011. ISSN 1098-0121. doi: 10.1103/PhysRevB.83.054401.

[89] A. C. Larson and R. B. Von Dreele. General Structure Analysis System (GSAS). Structure, 748(LAUR 86-748):86748, 2004. ISSN 0031-9007. doi: 10.1103/PhysRevLett.101.107006.

[90] [90] A. C. Larson, R. B. Von Dreele, and Brian H. Toby. General Structure Analysis System - GSAS / EXPGUI, A Graphical user interface for GSAS. J. Appl. Crystallogr., 748(1994):2001, 2001.

[91] T. H. Han, J. S. Helton, S. Chu, A. Prodi, D. K. Singh, C. Mazzoli, P. Mller, D. G. Nocera, and Y. S. Lee.Synthesis and characterization of single crystals of the spin- 1/2 kagomé -lattice antiferromagnets $ZnCu_3(OH)_6Cl_2$. Physical Review B, 83(10):100402, 2011. ISSN 1098-0121. doi: 10.1103/PhysRevB.83.100402.

[92] S. H. Lee, C. Broholm, W. Ratcliff, G. Gasparovic, Q. Huang, T. H. Kim, and S. W. Cheong. Emergent excitations in a geometrically frustrated magnet. Nature, 418(6900):856858, 2002. ISSN 00280836. doi: 10.1038/nature00964.

[93] D. Bergman, et al. Order-by-disorder and spiral spin-liquid in frustrated diamond-lattice antiferromagnets. Nature Physics, 3(7):487491, 2007. ISSN 17452473. doi: 10.1038/nphys622.

[94] J. N. Behera and C. N R Rao. A Ni2+ (S = 1) kagom compound templated by 1,8-diazacubane. Journal of the American Chemical Society, 128(29):93349335, 2006. ISSN 00027863. doi: 10.1021/ja063385f.

[95] S. Hara, H. Sato, and Y. Narumi. Exotic magnetism of novel S = 1 kagomé lattice antiferromagnet KV 3 Ge 2 O 9 . Journal of the Physical Society of Japan, 81(7):1013, 2012. ISSN 00319015. doi:10.1143/JPSJ.81.073707.

[96] D. E. Freedman, R. Chisnell, T. M. McQueen, Y. S. Lee, C.e Payen, and D. G. Nocera. Frustrated magnetism in the S = 1 kagomé lattice $BaNi_3(OH)_2(VO_4)_2$. Chem. Commun., 48(1):6466, 2012. ISSN 1359-7345. doi: 10.1039/C1CC14731E.

[97] M. Fiebig, T. Lottermoser, D. Meier, and M. Trassin. The evolution of multiferroics. Nature Reviews Materials, 1(8), 2016. ISSN 20588437. doi: 10.1038/natrevmats.2016.46.

[98] S. W. Cheong and M. Mostovoy. Multiferroics: A magnetic twist for ferroelectricity. Nature Materials, 6(1):1320, 2007. ISSN 14761122. doi: 10.1038/nmat1804.

[99] S. Seki, Y. Onose, and Y. Tokura. Spin-driven ferroelectricity in triangular lattice antiferromagnets $ACrO_2$ (A=Cu, Ag, Li, or Na). Physical Review Letters, 101(6):14, 2008. ISSN 00319007. doi: 10.1103/PhysRevLett.101.067204.

[100] K. Kimura, H. Nakamura, S. Kimura, M. Hagiwara, and T. Kimura. Tuning ferroelectric polarization reversal by electric and magnetic fields in $CuCrO_2$. Physical Review Letters, 103(10):25, 2009. ISSN 00319007.doi: 10.1103/PhysRevLett.103.107201.

[101] T. McQueen, Q. Huang, J. W. Lynn, R. F. Berger, T. Klimczuk, B. G. Ueland, P. Schiffer, and R. J. Cava. Magnetic structure and properties of the S = 5/2 triangular antiferromagnet α-$NaFeO_2$. Physical Review B, 76(2):024420, jul 2007. ISSN 1098-0121. doi: 10.1103/PhysRevB.76.024420.

[102] N. Terada, et al. Magnetic and ferroelectric orderings in multiferroic I - NaFeO2. Physical Review B - Condensed Matter and Materials Physics, 89(18): 111, 2014. ISSN 1550235X. doi: 10.1103/PhysRevB.89.184421.

[103] H. T. Stokes, D. M. Hatch, and J. D. Wells. Group-theoretical methods for obtaining distortions in crystals: Applications to vibrational modes and phase transitions. Physical Review B, 43(13):1101011018, may 1991. ISSN 0163-1829. doi: 10.1103/PhysRevB.43.11010.

[104] N. Hanni, et al. Low Temperature Phases of $Na_2Ti_3Cl_8$ Revisited. Zeitschrift fr anorganische und allgemeine Chemie, 643(23):20632069, 2017. ISSN 00442313. doi: 10.1002/zaac.201700331.

[105] D. J. Hinz, et al. $Na_2Ti_3Cl_8$: From Isolated Ti^{2+} Ions to$[Ti_3]^{6+}$ Clusters. Angewandte Chemie International Edition in English,34(1) : 7173, 1995. ISSN05700833.doi:10.1002/anie.199500711.

[106] Allen Scheie. LongHCPulse: Long Pulse Heat Capacity on a Quantum Design PPMS. pages 18, 2017.

[107] J. P. Sheckelton, et al. Rearrangement of van der Waals stacking and formation of a singlet state at T = 90 K in a cluster magnet. Inorg. Chem. Front., 4(3):481490, 2017. ISSN 2052-1553. doi: 10.1039/C6QI00470A.

[108] X. G. Wen. Gapless boundary excitations in the quantum Hall states and in the chiral spin states. Physical Review B, 43(13):1102511036, 1991. ISSN 01631829. doi: 10.1103/PhysRevB.43.11025.

[109] G. J. Miller. Chemistry and properties of novel niobium cluster compounds. Journal of Alloys and Compounds, 229(1):93106, 1995. ISSN 09258388. doi: 10.1016/0925-8388(95)80031-X.

[110] N. Ikeda, et al. Ferroelectricity from iron valence ordering in the charge-frustrated system $LuFe_2O_4$. Nature, 436(7054):11361138, 2005. ISSN 00280836. doi: 10.1038/nature04039.

[111] Y. Wang, et al. Unveiling hidden ferrimagnetism and giant magnetoelectricity in polar magnet $Fe_2Mo_3O_8$. Scientific Reports, 5(1):12268, 2015. ISSN 2045-2322. doi: 10.1038/srep12268.

[112] R. H. Sanchez, et al. Maximizing Electron Exchange in a [Fe_3] Cluster. Journal of the American Chemical Society, 138 (7):22352243, 2016. ISSN 15205126. doi: 10.1021/jacs.5b12181.

[113] G. M. Sheldrick. A short history of SHELX. Acta Crystallographica Section A: Foundations of Crystallography, 64(1):112122, 2007. ISSN 01087673. doi: 10.1107/S0108767307043930.

[114] N. A. Benedek and C. J. Fennie. Why are there so few perovskite ferroelectrics? Journal of Physical Chemistry C, 117(26):1333913349, 2013. ISSN 19327447. doi: 10.1021/jp402046t.

[115] J. F. Scott and R. Blinc. Multiferroic magnetoelectric fluorides: Why are there so many magnetic ferroelectrics? Journal of Physics Condensed Matter, 23(11), 2011. ISSN 09538984. doi: 10.1088/09538984/23/11/113202.

[116] K. Asadi and M. A. van der Veen. Ferroelectricity in Metal Organic Frameworks: Characterization and Mechanisms. European Journal of Inorganic Chemistry, 2016(27):43324344, 2016. ISSN10990682. doi: 10.1002/ejic.201600932.

[117] K. M. Ok, E. O. Chi, and P. S. Halasyamani. Bulk characterization methods for noncentrosymmetric materials: second-harmonic generation, piezoelectricity, pyroelectricity, and ferroelectricity. Chemical Society Reviews, 35(8):710, 2006. ISSN 0306-0012. doi: 10.1039/b511119f.

[118] M. A. de Vries. Model s reputation restored. Nature, 468:908909, 2010.

[119] G. Jackeli and G. Khaliullin. Mott Insulators in the Strong Spin-Orbit Coupling Limit: From Heisenberg to a Quantum Compass and Kitaev Models. Physical Review Letters, 102(1):017205, 2009. ISSN 0031-9007. doi: 10.1103/PhysRevLett.102.017205.

[120] T. Yamamoto, et al. An antiferro-to-ferromagnetic transition in $EuTiO_{(3-x)}H_{(x)}$ induced by hydride substitution. Inorganic chemistry, 54(4):15017, 2015. ISSN 1520510X. doi: 10.1021/ic502486e. URL http://dx.doi.org/10.1021/ic502486e.

[121] T. Sakaguchi, et al. Oxyhydrides of (Ca,Sr,Ba)TiO_3 Perovskite Solid Solutions. Inorganic Chemistry, 51(21):1137111376, 2012. ISSN 0020-1669. doi: 10.1021/ic300859n.

[122] T. Yajima, et al. A labile hydride strategy for the synthesis of heavily nitridized $BaTiO_3$. Nature Chemistry, advance on(October):17, 2015. ISSN 1755-4330. doi:10.1038/nchem.2370.

[123] J. T Rijssenbeek, et al. Site and oxidation-state specificity yielding dimensional control in perovskite ruthenates. Journal of the American Chemical Society, 124(10):20901, 2002. ISSN 0002-7863. doi: 10.1021/ja017586p.

Biography

Zachary Andrew Kelly was born to Patricia and Tim Kelly in Lansdale, Pennsylvania on March 4th, 1988. Raised in Hatfield, Pennsylvania, with his younger brother, Matthew, and sister, Amy, Zach graduated from North Penn High School in May 2006. In September that year, Zach begin his academic career at Pennsylvania State University, where he majored in chemistry. Zach quickly joined a research group where he explored charge carriers dynamics in bulk heterojunction organic photovoltaics under the guidance of Professor John Asbury. In his graduate studies at Johns Hopkins University, under the guidance of Professor Tyrel M. McQueen, Zach focused on the theory, synthesis, and physical properties of geometrically frustrated magnetic materials. Zach earned his Master of Arts degree in May 2015, and his Doctor of Philosophy degree in February 2018.